Antenna design and radio channels for emerging micro- and millimeter wave applications

Jansen, F.G.

Award date:
2006

TU/e technische universiteit eindhoven

ANTENNA DESIGN AND RADIO CHANNELS FOR EMERGING MICRO- AND MILLIMETER WAVE APPLICATIONS

By F.G. Jansen

/faculteit elektrotechniek

Eindhoven University of Technology
Faculty of Electrical Engineering
Division of Telecommunication Technology and Electromagnetics
Radiocommunication Group

TTE

ANTENNA DESIGN AND RADIO CHANNELS FOR EMERGING MICRO- AND MILLIMETER WAVE APPLICATIONS

by F.G. Jansen

Master of Science Thesis
Carried out from 17-10-2005 to 30-06-2006

Supervisors:
Dr. ir. P.F.M. Smulders
Dr. ir. M.H.A.J. Herben
Dr. ir G. Dolmans

Graduation professor:
Prof. Dr. ir. E. R. Fledderus

Abstract

The advancement of silicon IC processes opens up new opportunities to develop new consumer microwave applications. The cut-off frequencies of silicon IC processes evolve to higher frequencies and therefore offer the possibility to develop new applications. In this project antennas for an automotive radar system at 24 GHz and a wireless personal area network at 60 GHz have been designed. The most severe requirements on the antennas were the large bandwidth, high gain and in the case of the automotive radar system the gain above a fixed elevation angle. Prior to this project a substrate stack was selected. A tradeoff was made between a substrate optimized for antenna performance and a substrate optimized for the performance of integrated circuits.

Transmission lines play a key role in the design of antennas especially at high frequencies. The propagation constant, attenuation factor and characteristic impedance of the microstrip line and the coplanar waveguide have been determined using so-called dispersive models and simulations in ADS Momentum. The coplanar waveguide has a higher degree of freedom in design and the possibility to be designed with a lower attenuation factor than the microstrip line.

A comparison was performed between antennas based on the microstrip patch design, a planar variant of the horn antenna called the tapered slot antenna and a slot antenna called bow-tie slot antenna. The latter two antennas were selected based on the wide return loss bandwidth. A tapered slot antenna and a bow-tie slot antenna both for 24 GHz as well as a scaled version of the bow-tie slot antenna designed for 60 GHz were fabricated. The return loss bandwidth as well as the radiation patterns of the fabricated antennas were measured. The measurements showed that the bandwidth requirement was met. The measured gains were comparable to the simulations in the case of the bow-tie slot antenna for 24 GHz but were higher in the case of the tapered slot antenna. However the gain requirement was not met by both antennas. In addition the gain requirement at a fixed elevation angle was not met.

Small-scale indoor radio channel measurements have been performed. An omni directional antenna, fan beam antenna and bow-tie slot antenna have been used as receive antennas and a omni directional antenna was used as transmit antenna. The radio channel was measured in a line of sight and in a non line of sight situation. The fan beam receive antenna had the highest received power and the lowest delay spread. The bow-tie slot antenna had the lowest received power and the highest delay spread. The coherence bandwidth could not be obtained by directly calculating the correlation in the frequency domain. Therefore two approximations based on the RMS delay spread have been used. The fan beam antenna had the largest coherence bandwidth followed by the omni directional antenna and the bow-tie slot antenna. A Ricean distribution was fitted to the absolute value of the received signal. The lowest Ricean k-factor was observed for the omni directional and the bow-tie slot antennas. The k-factor of these antennas in the NLOS situation was higher. The opposite behavior was observed for the fan beam antenna.

Contents

Chapter 1

Introduction

The advancement of silicon IC processes opens up new opportunities to develop new consumer microwave applications. The cut-off frequencies of silicon IC processes evolve to higher frequencies and therefore offer the possibility to develop applications in the 24 GHz (short range radar), 60 GHz (wireless personal area network), 77 GHz (long range radar) and 79 GHz (short range radar) frequency bands. In addition the envisioned applications require a large bandwidth. This bandwidth is not available at lower frequencies. In the integrated transceiver group at Philips Research demonstrators will be developed for microwave radar and radio applications. The circuits and the antenna of the demonstrator will be integrated into a module. Therefore a substrate was chosen prior to this project. The substrate choice is a tradeoff between the performance of the circuits and the performance of the antenna.
In this report the results of an investigation into microwaves antennas and transmission lines for short range automotive radar at 24 GHz and a wireless PAN at 60 GHz are presented. In order to be able to design the wireless PAN at 60 GHz the properties of the indoor radio channel at this frequency have to be known. Therefore several experiments using omni directional and fan beam antennas as well as the antenna designed in this project have been performed. The results of these experiments are presented in the second part of this report.
Prior to this project a literature survey was performed. The aim of this literature survey was to find antenna designs which can be used for short range radar at 24 GHz or wireless PAN at 60 GHz. Based on this literature search a pre-selection was made. The pre-selected antenna designs are used in this project.

This report has the following layout, the envisioned applications are presented in Chapter 2. These applications place strong demands on the design of the antenna. These requirements are presented in Chapter 3. The transmission lines play an important role in the design of antennas especially at high frequencies and are therefore treated in Chapter 4. Two basic designs have been used in this project. The first design is the microstrip patch antenna the second design is based on a slot in a ground plane. The results of the antennas based on the microstrip patch design are presented in Chapter 5. The design and simulation results of the designs based on a slot in a ground plane are treated in Chapter 6. The fabricated antennas were tested on return loss bandwidth, radiation pattern and gain. The results of these tests are presented in Chapter 7. In the second part of this report the properties of a 60 GHz indoor radio channel are investigated. The results of this investigation are presented in Chapter 8. In Chapter 9 the most important results of this project have been summarized and the main conclusions of the project are presented.

Chapter 2

Applications

The antennas that have been developed in this project are intended for two applications. The first application is an automotive radar at 24 GHz. This radar system can be used as a safety feature on automobiles and as a parking aid. The second application is a high speed wireless data network at 60 GHz. This network should push wireless data speeds into the Gigabits per seconds range. In this chapter the 24 GHz short range radar and the wireless data network at 60 GHz will be treated.

2.1 24 GHz short range radar

The first considered application is a vehicular radar system. With this system the position and speed of vehicles or objects around the concerning vehicle can be detected. Using this system a vehicle can be equipped with a 360° radar map. Currently systems are available that offer similar possibilities. These systems are based on ultrasonic or laser technology and are therefore not immune to bad weather conditions, when these systems are needed most. In addition a radar sensor could be hidden behind a plastic bumper which is transparent for the electromagnetic waves, see references [1] and [2].

Several features can be offered by the radar system. The first feature is a collision warning system in which the system alerts the driver to dangerous situations. A collision warning system has to give to the driver information indicating the need for urgent action to avoid a collision. The warning has to be provided in the advanced phases of a dangerous situation in order to warn the driver for the need to perform emergency braking, lane changing or other emergency avoidance manoeuvres. The second feature is a parking aid which gives the driver an accurate measure of the range of objects surrounding the car. Other features are: a lane change assistant, blind spot detection and automatic cruise control, these features are illustrated in Figure 2.1.

The implementation of vehicle based radar systems started with a 77 GHz long range radar system that provided automated cruise control for vehicles in the high price class. With the progress made in silicon IC process there are possibilities to develop automotive radar systems suitable for mass production. It is expected that technologies operating at 77 GHz will remain too expensive for mass production in the coming years. However a 24 GHz frequency band for automotive short range radar has been allocated by the European Commission and the FCC. These agencies have identified automotive short range radar as a significant technology for the improvement of road safety. The 24 GHz band overlaps existing bands i.e. the 23.6 GHz till 24 GHz band used by radio astronomy. Therefore the allocation of the 24 GHz band is temporary

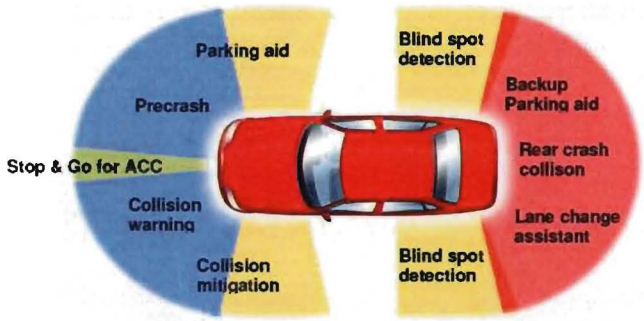

Figure 2.1: Different types of applications for short range radar.

and will end in 2013. Only Europe has this end-date, there the 79 GHz band will be used for short range radar in the future, see reference [1]. The 24 GHz band is strictly regulated, an overview of the regulations is given in Table 3.1 and in Figure 3.1.

At Philips Research the choice was made to use a radar system based on pseudo-noise coding. Other systems are based on a pulse radar system or a frequency sweep radar system. The schematic of the system is depicted in Figure 2.2. As can be seen a 24 GHz carrier signal is

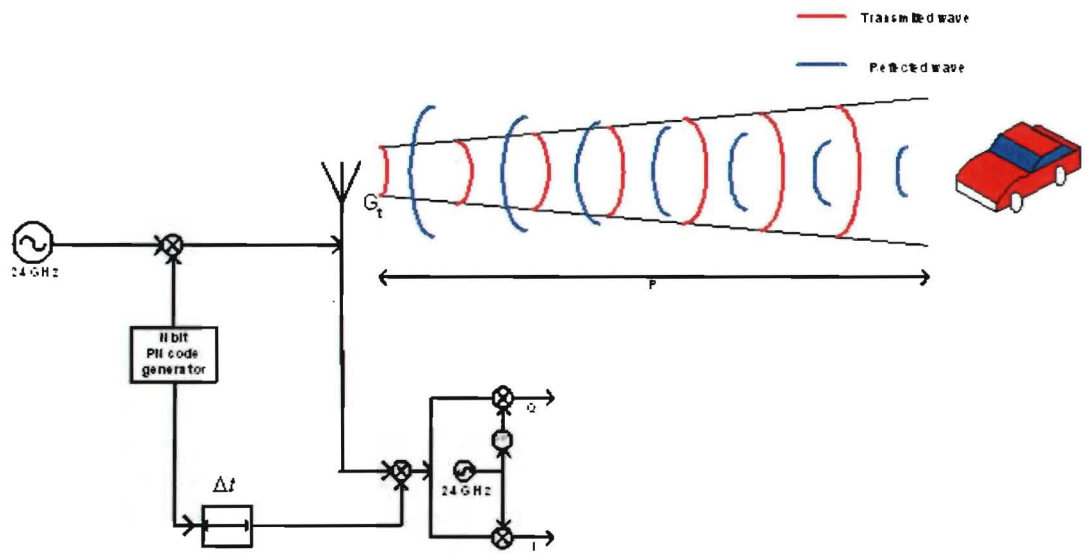

Figure 2.2: Schematic of the pseudo-noise automotive radar system.

multiplied by a N bit pseudo random code which switches between +1 and -1. This multiplication can thus be seen as pseudo-noise phase shift keying (PN-PSK). This signal is then transmitted by the antenna. The transmitted signal is reflected by the target and received by the antenna. The received signal is then multiplied by the pseudo-noise sequence, delayed by Δt seconds and mixed down by the 24 GHz carrier signal, by splitting the obtained signal in an in-phase and quadrature component the speed and distance are obtained. The time delay is varied so all distances are covered. If the delay Δt is equal to the round trip time of the transmitted signal a low frequency signal will be obtained. If the delay is not equal to the round trip time a signal will be

obtained that has a spread spectrum. A low pass filter can thus be used to check which delay time corresponded to the round trip time of the signal. The round trip time of the signal is given by:

$$T_d = \frac{2R}{c} \tag{2.1}$$

where c is the speed of light. The autocorrelation of the received PN code with the shifted reference PN code is given in reference [3] by:

$$R_{cc}(\tau) = \frac{1}{T_{seq}} \int_{-T_{seq}/2}^{T_{seq}/2} C_{RX}(t - T_d) C_{RE}(t - \tau) dt \tag{2.2}$$

where $C_{RX}(t - T_d)$ is the received PN code, $C_{RE}(t - \tau)$ is the reference code shifted by τ and $T_{seq} = N/F_{ch}$ where F_{ch} is the chip rate of the PN code and N is its length. The reference PN code is shifted by fixed steps τ_s. The range resolution can now be given as:

$$R_{min} = \pm c \cdot \tau_s / 2 \tag{2.3}$$

If $\tau_s = 1/F_{ch}$, that is the shift in time is equal to one chip, the Nyquist bandwidth of this system is $2 \cdot F_{ch}$. In the worst case the correlation function is evaluated for every shift of the reference PN code. The processing time, which is the reciprocal of the number of range updates per second , is now given as:

$$T_s = (T_d/\tau_s)(N/F_{ch}) = \frac{R}{R_{min}} T_{seq} \tag{2.4}$$

The received power is given by the radar transmission equation, see reference [4].

$$P_r = \frac{(G_d \lambda)^2 N \sigma_{radar} P_{rad}}{(4\pi)^3 R^4} \tag{2.5}$$

The power is reflected by the target which has a radar cross section σ_{radar}, the antenna gain is given by G_d, P_{rad} is the power in W radiated by the antenna, N is the length of the PN code and R is the distance to the target. In Equation 2.5 it is assumed that one antenna, with antenna gain G_d is used to transmit and receive the signal, this explains the quadratic term for the antenna gain. Since the radiated power is limited to the maximum allowed power the received power can be increased by increasing the antenna gain or increasing the length of the N bit pseudo noise sequence. Increasing N leads to an increase in the integration time, (thus in received power) but also in the time between two consecutive updates of the range and speed, see Equation 2.4. When only one antenna is used and the antenna gain is increased then the power delivered to the antenna has to be decreased to keep the maximum allowed transmitted power below the fixed level.
The advantage of using a pseudo-noise based radar over a pulse radar or CW-FM radar is the robustness. Since there will be less interference between different cars due to different codes used in each car. In addition by using spread spectrum techniques the system is less sensitive to narrowband interference. By increasing the length of the pseudo-noise sequence the integration time is increased. This leads to an increase in processing gain.

2.2 Wireless 60 GHz network

The second application of the antenna designs presented in this report is a high speed wireless network at 60 GHz. This application is currently developed within the Sigi-Spot project. The goal of this project is to develop an ultra fast wireless data network using low priced components. The license free 60 GHz band is used to achieve the high data rate. This wireless network will be designed to have a data speed of 1 GB/s or higher. This can be achieved because there is a large bandwidth available at 60 GHz. The allocated spectrum for 60 GHz ranges from 59 GHz to 64 GHz for mobile applications. The investigation of the 60 GHz channel has been started before this project. This investigation indicates a high path loss. This property of the 60 GHz channel leads to small cells in which this bandwidth can be used. This again leads to the opportunity to reuse the same frequency many times in a small area. Since the antenna for the 60 GHz wireless network also requires a large bandwidth an attempt will be made to construct a scaled version of one of the antennas designed for the 24 GHz short range radar that will operate at 60 GHz. This antenna will then be used to perform indoor radio channel measurements at 60 GHz. This project has started before the official start date of the Sigi-Spot project. Therefore no hard requirements for the antenna were available, except for the bandwidth requirement of 5 GHz and high gain.
Possible applications for the 60 GHz band could be: wireless Gigabit Ethernet, wireless transmission of digital high definition television signals (Wireless HDMI) and high speed synchronization with portables devices i.e. PDA's, digital cameras or portable audio devices.

Chapter 3

Antenna requirements and substrate technology

The type of application determines the requirements on the antenna. In this chapter these requirements will be given and explained. In design of integrated antennas the choice of the substrate technology and the layout plays an important role. In this project the choice for the substrate technology had been made prior to the start of this project. As a consequence antenna designs had to be searched that meet the requirements and can be implemented using the given substrate. The chosen substrate technology is treated in Section 3.2.

3.1 Requirements

The requirements on the antenna are not the same for the two applications that were discussed in Chapter 2. The requirements for the antennas to be used for the short range radar were well defined and will be treated in detail. The requirements for the antennas to be used in the high speed wireless network at 60 GHz were not well defined at the beginning of this project. Therefore the choice was made to use a scaled version of one of the antennas designed for the short range radar. The strongest demand for this scaled version was that the bandwidth should be at least 5 GHz.

3.1.1 Short range radar at 24 GHz requirements

The most important requirement on the short range radar is to accurately measure the distance between the vehicle and the objects surrounding the car. The parking aid feature demands the highest range resolution. Typically a resolution of 5 cm is required. To obtain a range resolution of 5 cm a time shift τ_s of $1/3 \cdot 10^{-9}$, see Equation 2.3, is needed thus $F_{ch} = 3 \cdot 10^9$, and the Nyquist bandwidth is 6 GHz.
The radiation above the horizon for the 23.6 to 24 GHz band, is limited because of the interference with the radio astronomy band. This limitation will become more severe during the years, see Table 3.1. The emission spectrum is depicted in Figure 3.1. The regulations of the 23.6 to 24 GHz band are also included in this figure.

Year	Suppression	Angle
.. - January 1st 2005	25 dB	38°
January 1st 2005 - January 1st 2010	25 dB	30°
January 1st 2010 - January 1st 2014	30 dB	30°
January 1st 2014 - ..	35 dB	30°

Table 3.1: European emission rules for the 23.6 GHz - 24 GHz (radio astronomy) band.

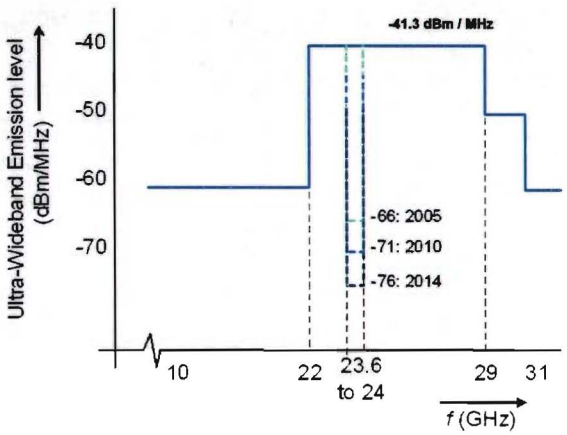

Figure 3.1: Emission spectrum as set by ETSI

To estimate the required antenna gain a link budget calculation is presented in Table 3.2. The free space loss has been calculated using Equation 2.5 and is very high. The effective isotropic radiated power of the antenna is limited by the ETSI regulation to -41.3 dBm in 1 MHz of bandwidth, see Figure 3.1. Since it is assumed that only one antenna is used to transmit and receive the signal this poses a problem. This can be solved by increasing the antenna gain and simultaneously reducing the transmitted power in order to maintain a maximum EIRP of -41.3 dBm. In addition the spread spectrum technique introduces a compression gain of 30 dB if a PN code with a length of 1024 bits is used. The total received power now is -96.5 dBm. By using an antenna with a gain of 6.5 dBi or higher, and reducing the power delivered to the antenna to stay below the maximum EIRP, the required received power can be obtained.

Parameter	Value
σ_{radar}	1 m^2
Required maximum range	30 m
Free space wavelength	1.25 10^{-2} m
Receiving antenna gain	0 dBi
Transmitted power	2 dBm
Free space loss	-128.5 dB
Received power	-126.5 dBm
Compression gain	30 dB
Required receiving antenna gain	6.5/16.5 dBi
Total received power required	-80/90 dBm

Table 3.2: Link budget calculation for the 24 GHz band.

Philips Research intends to demonstrate the RF part of the PN coded radar system. The RF part will be placed inside a module. No high frequency signals will be transferred outside this module. Therefore the antenna has to be small enough to be incorporated into a module. This requirement rules out the use of large metal antennas like horn antennas.

3.2 Substrate technology

In this section a short description of the substrate stack that was used for the design and construction of the feeding structure and the antennas is given. No other stacks have been used. The substrate stack was provided by Philips Research. Since this substrate should be used for the driving circuits as well as for the antenna a comprise is made. Common antenna designs, i.e. microtrip patch antennas, usually require an electrically thick substrate with a low permittivity while microwave circuitry requires a thin substrate with high permittivity. In addition the developed circuits and antennas are intended to be used in a mass production process. This requires a low cost substrate stack.

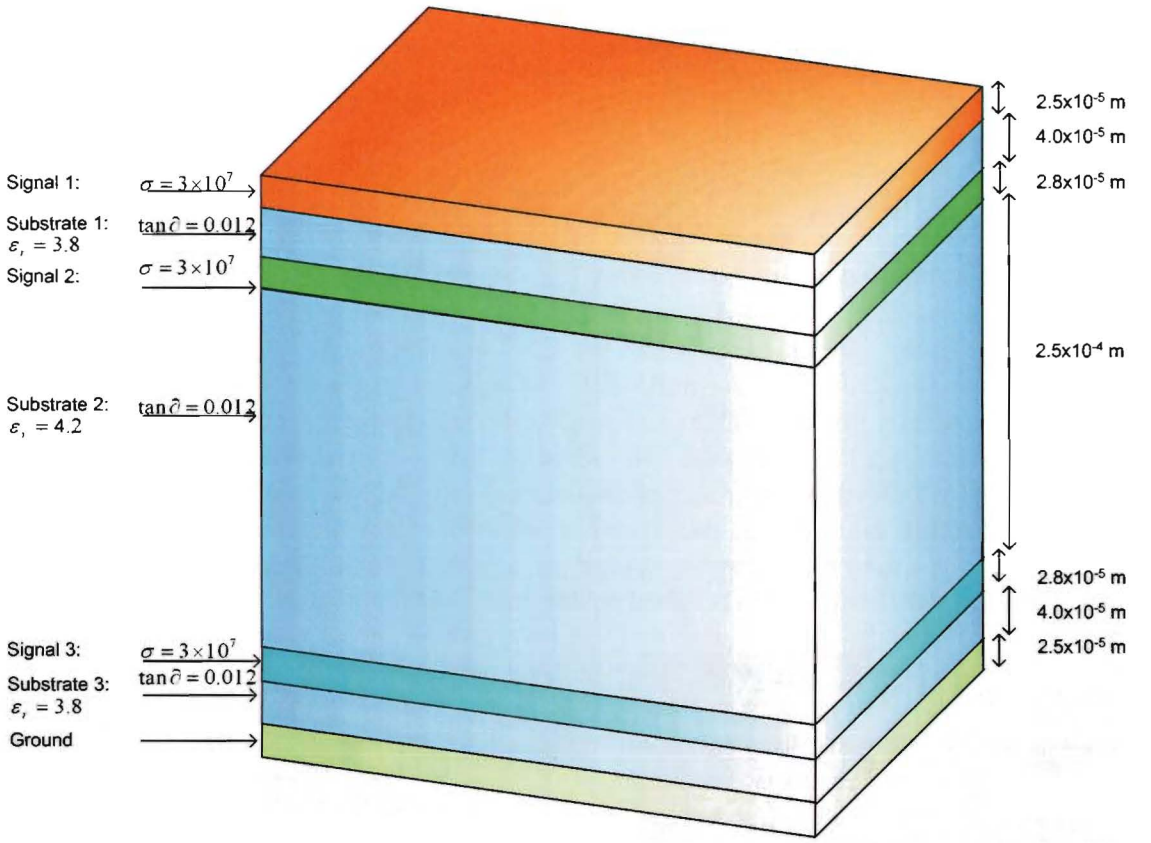

Figure 3.2: Three dimensional representation of the substrate stack that was provided by Philips Research.

The chosen substrate stack is depicted in Figure 3.2. The stack consists of three signal layers made out of copper separated by three dielectric substrates of varying thickness. The three signal layers and the ground plane can be connected to each other by vias. The conductivity, σ, of the metal layers is 3×10^7 Siemens/m. The bottom of the stack can be closed with a metal ground

Chapter 4

Transmission lines

At high frequencies transmission lines play an important role in the design of antennas. To be able to design a good antenna it is important that the transmission line which connects the antenna to the rest of the system is well designed. Therefore transmission lines were investigated. In the first part of this chapter the theory used to describe the properties of the transmission lines is treated. In the second part models, based on empirical data, were implemented in Matlab. These models have been used to simulate the transmission lines. The obtained data is compared to other simulators. In the last part tapered transitions are treated. These transitions can be used to connect transmission lines with different dimensions to each other. The transmission line plays a key role in antenna design. It connects the antenna with the other parts of the circuit. If the transmission line is not well designed reflections will occur which will seriously degrade the performance of the antenna. It is assumed that all the circuits that drive the antenna have an output impedance of 50 Ω. Therefore, the transmission line and the antenna also need to have a characteristic impedance of 50 Ω to prevent reflections. Another possibility is the use of circuits that convert a line with a different impedance to a 50 Ω line. These circuits have not been considered.
In this chapter the equations governing lossy transmission lines will be treated. There are two methods of calculating the characteristic impedance and the propagation constant. The first method that is used, is a quasi static method. The second method follows from a full wave analysis. The most important outcome is the dispersive nature or frequency dependency of the characteristic impedance and propagation constant. However the full wave analysis is a complicated process and is beyond the scope of this project. Therefore quasi empirical methods, known as the dispersive models, have been used. The obtained frequency dependent values then substitute the quasi static values.
Two types of transmission lines were used, the microstrip line and the coplanar waveguide. The treated model, for the microstrip line as well as for the coplanar waveguide, has been implemented in Matlab from Mathworks. The outcome of these models is compared to the outcome of computer aided design (CAD) programs often used in industry and scientific environments as well as to results obtained with Advanced Design System from Agilent Technologies.

plane. The signal one layer can be covered by a protecting moulding layer, not depicted in Figure 3.2, with a relative permittivity of $\epsilon_r = 3$ and loss tangent $\tan\delta = 0$. The smallest structure that can be made has to be at least 50 μm wide. As can be seen the permittivity of the inner conductor, $\epsilon_r = 3.8$ is different from the permittivity of the two outer conductors, $\epsilon_r = 4.2$. The loss tangent of the dielectric substrates is $\tan\delta = 0.012$. In this project extensive use has been made of ADS Momentum. In this simulator it is assumed that the substrate extends to infinity.
In the next chapter several transmission line models will be discussed. These models are compared with the results of commercial computer programs. The tested computer programs are limited in the number of layers in the substrate stack. Therefore a simplified representation of the stack will be used in the transmission line models. The simplified stack consists of only one substrate with a permittivity of $\epsilon_r = 4$ and with a height equal to the combined height of the three substrate layers, $h = 330\mu$m.

The colors that have been used to indicate the different materials and layers in Figure 3.2 are used in the remainder of this report.

4.1 Microstrip lines

Microstrip lines belong to the parallel-plate group. They consist of a metal strip and a metal ground plane separated by a dielectric substrate. The width of the strip line is given by W and the height of the substrate is given by h. In Figure 4.1 a cross section of the microstrip line is de-

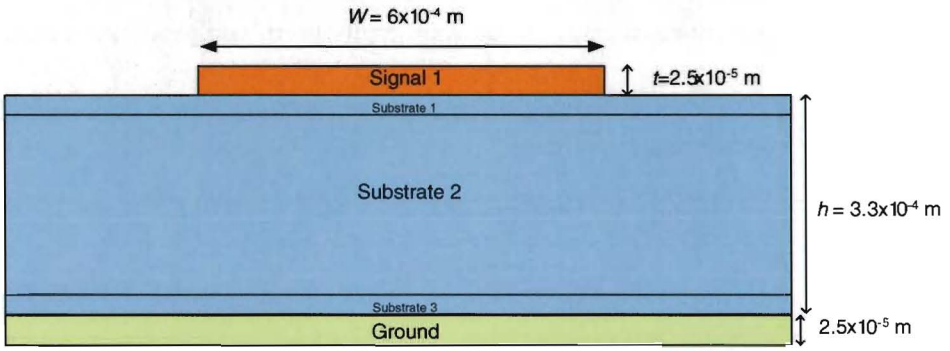

Figure 4.1: Cross section of the microstrip line.

picted. However, most of the CAD programs do not support a multi-layered substrate. Therefore a single substrate with $\epsilon_r = 4$ and a total height of the combined heights of the three substrate layers is used. The strip line is not completely surrounded by a homogeneous dielectric substrate. Therefore the electromagnetic (EM) field is not only confined to the substrate between the strip line and the ground plane but is also present in the air above the strip line. Due to the fringing

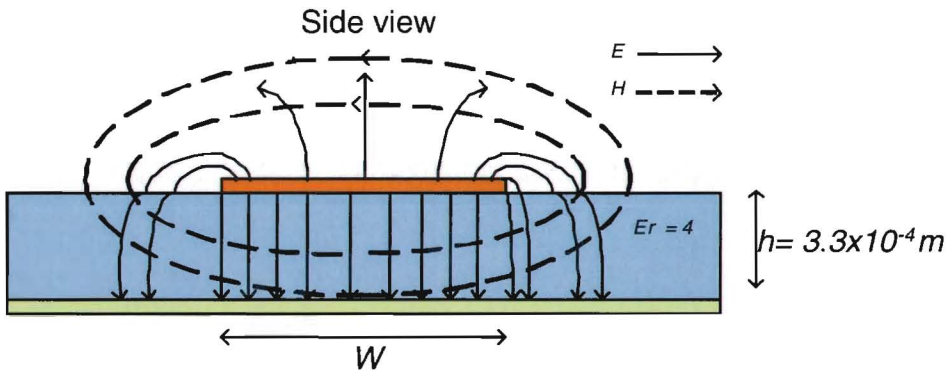

Figure 4.2: The fringing field of a microstrip line

fields, see picture 4.2, at the dielectric-air interface it is not possible to support a pure TEM, TE or TM mode. Since the fringing fields are much smaller than the main field (between the strip and the ground plane), the microstrip line is often referred to as quasi-TEM mode. For more information about the equations describing transmission lines see Appendix A. To be able to use the theory described in Appendix A the resistance, inductance and capacitance of the transmission line have to be known. These parameters could be obtained by use of a full wave analysis. However this is beyond the scope of this project. Therefore closed form equations are used that have been obtained by curve fitting the results of a numerical simulation. The equations were taken from reference [5].

Because of the fringing fields, see Figure 4.2, in the material above the strip the relative permittivity has to be adjusted in order to calculate the capacitance and inductance. An effective permittivity, ϵ_{reff}, is introduced for $W/h \leq 1$ and is given by:

$$\epsilon_{reff} = \frac{\epsilon_r + 1}{2} + \frac{\epsilon_r - 1}{2\sqrt{1 + 12\frac{h}{W}}} \tag{4.1}$$

There are two approximations for the characteristic impedance depending on the ratio of $\frac{w}{h}$.

$$Z_0 = \begin{cases} \frac{60}{\sqrt{\epsilon_{reff}}} \ln(\frac{8h}{W_e} + 0.25\frac{W_e}{h}) & \text{if } \frac{W}{h} \leq 1; \\ \frac{1}{\sqrt{\epsilon_{reff}}} \frac{120\pi}{[\frac{W_e}{h} + 1.393 + 0.667 \ln(\frac{W_e}{h} + 1.444)]} & \text{if } \frac{W}{h} \geq 1. \end{cases} \tag{4.2}$$

where W_e is introduced to account for the finite thickness of the metal strip.

$$\frac{W_e}{h} = \begin{cases} \frac{W}{h} + \frac{1.25t}{\pi h}(1 + \ln(\frac{4\pi W}{t})) & \text{if } \frac{W}{h} \leq 1/2\pi.; \\ \frac{W}{h} + \frac{1.25t}{\pi h}(1 + \ln(\frac{2h}{t})) & \text{if } \frac{W}{h} \geq 1/2\pi.; \end{cases} \tag{4.3}$$

The last effect that has to be included is dispersion. The effective permittivity, ϵ_{reff} depends on the frequency.

$$\epsilon_{reff}(f) = \epsilon_r - \frac{\epsilon_r - \epsilon_{reff}}{1 + (\frac{f}{f_{50}})^m} \tag{4.4}$$

$$f_{50} = \frac{f_{k,TM_0}}{0.75 + \{0.75 - (0.332/\epsilon_r^{1.73})\}\frac{W}{h}} \tag{4.5}$$

$$f_{k,TM_0} = \frac{ctan^{-1}(\epsilon_r \sqrt{\frac{\epsilon_r - 1}{\epsilon_r - \epsilon_{reff}}})}{2\pi h \sqrt{\epsilon_r - \epsilon_{reff}}}$$

$$m = m_0 m_c$$

$$m_0 = 1 + \frac{1}{1 + \sqrt{\frac{W}{h}}} + 0.32(\frac{1}{1 + \sqrt{\frac{W}{h}}})^3$$

$$m_c = \begin{cases} 1 + \frac{1.4}{1 + \frac{W}{h}} \left\{0.15 - 0.235 \exp(\frac{-0.45f}{f_{50}})\right\} & \text{if } \frac{W}{h} \leq 0.7 \\ 1 & \text{if } \frac{W}{h} \geq 0.7 \end{cases}.$$

where ϵ_{reff} is the static effective permittivity obtained in Equation 4.1 and c is the speed of light which was taken to be $3 \cdot 10^8 m/s$. A plot of the frequency dependency of the relative permittivity is depicted in Figure 4.3. For frequencies below 1 GHz the quasi static value of ϵ_r seems to provide a good approximation. The effective relative permittivity approaches the value of the permittivity of the dielectric substrates for very high frequencies. When the effective relative permittivity obtained in Equation 4.1 is filled in Equation 4.2 a frequency dependent equation is obtained for the characteristic impedance. A simulated result of the frequency dependence is depicted in Figure 4.4. With the obtained effective relative permittivity the phase constant β and the attenuation factor α can be calculated.

$$\beta = \frac{\omega\sqrt{\epsilon_{reff}(f)}}{c} \tag{4.6}$$

The losses in a microstrip line, α_t in $\mathrm{dB}m^{-1}$, can be split into two parts. The losses in the dielectric substrate, α_d and the losses in the conductor strip, α_c.

$$\alpha_t = \alpha_c + \alpha_d \tag{4.7}$$

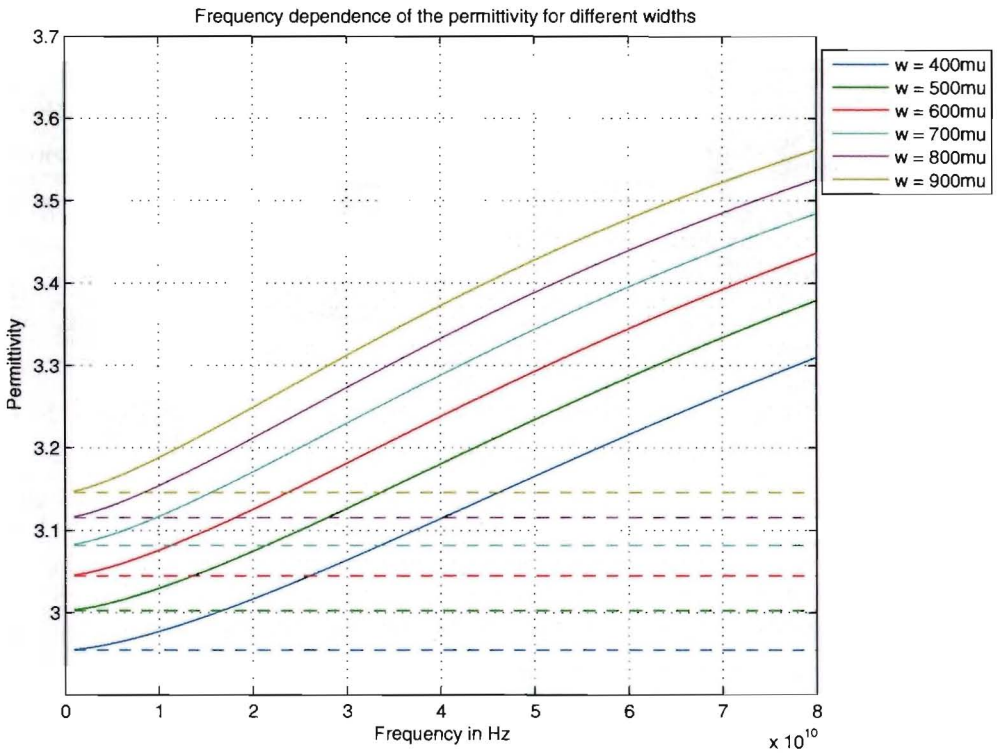

Figure 4.3: Relative permittivity of the microstrip line for different widths W plotted against the frequency (scale 1 GHz till 80 GHz), the dashed lines indicate the quasi static approximation of the relative permittivity.

Width	ϵ_r at 0 GHz	ϵ_r at 24 GHz	ϵ_r at 60 GHz	ϵ_r at 77 GHz	Difference in % at 24 GHz	Difference in % at 60 GHz	Difference in % at 77 GHz
w = 400 μm	2.95	3.04	3.21	3.30	3.05 %	8.81 %	11.86 %
w = 500 μm	3.00	3.10	3.29	3.37	3.33 %	9.67 %	12.33 %
w = 600 μm	3.05	3.15	3.35	3.42	3.28 %	9.84 %	12.13 %
w = 700 μm	3.08	3.19	3.40	3.47	3.57 %	10.39 %	12.66 %
w = 800 μm	3.12	3.24	3.44	3.51	3.85 %	10.26 %	12.50 %
w = 900 μm	3.15	3.27	3.48	3.55	3.81 %	10.48 %	12.70 %

Table 4.1: Difference in percentages between the static permittivity and the frequency dependent permittivity for different widths of the microstrip line and at the three frequencies considered in this project.

The losses in the conductor, α_c, are calculated by:

$$\alpha_c = \begin{cases} 1.38A\frac{R_S}{hZ_{0m}}\frac{32-(\frac{W_e}{h})^2}{32+(\frac{W_e}{h})^2} & \text{dB /unit length if } \frac{W}{h} \leq 1 \\ 6.1\times 10^{-5}A\frac{R_s Z_{0m}\epsilon_{reff}(f)}{h}\left\{\frac{W_e}{h}+\frac{0.667\frac{W_e}{h}}{\frac{W_e}{h}+1.444}\right\} & \text{dB/unit length if } \frac{W}{h} \geq 1 \end{cases} \tag{4.8}$$

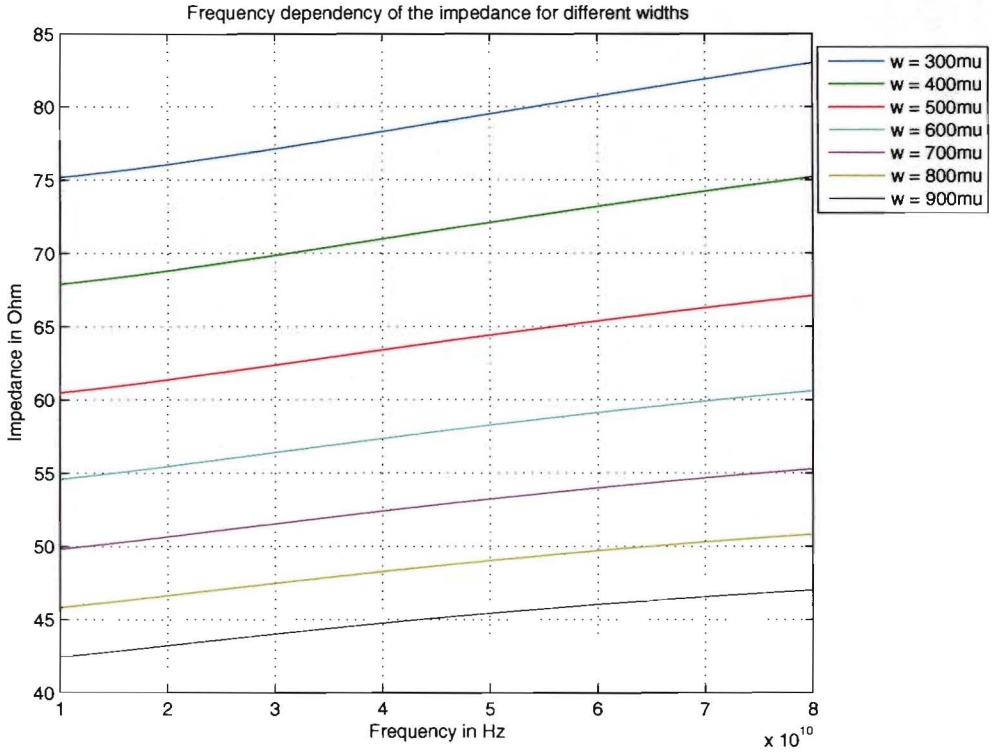

Figure 4.4: Characteristic impedance of the microstrip line for different widths W plotted against the frequency

$$
\begin{aligned}
R_s &= \sqrt{\pi f \mu_0 \rho_c} \\
\rho c &= \text{resistivity of the strip} \\
A &= 1 + \frac{h}{W_e}\left\{1 + \frac{1.25}{\pi}\ln\frac{2B}{t}\right\} \\
B &= \begin{cases} h & \text{if } \frac{W}{h} \geq \frac{1}{2\pi} \\ 2\pi W & \text{if } \frac{W}{h} \leq \frac{1}{2\pi} \end{cases}
\end{aligned}
\tag{4.9}
$$

The losses in the dielectric are given by:

$$
\alpha_d = 27.3\frac{\epsilon_r}{\epsilon_r - 1}\frac{\epsilon_{reff}(f) - 1}{\sqrt{\epsilon_{reff}(f)}}\frac{tan\delta}{\lambda_0}\text{dB/unit length} \tag{4.10}
$$

The results for the phase constant β and the attenuation factor α are depicted in figures 4.5 and 4.6. Since the height h is fixed the only parameter that can be varied is W. In Figure 4.4 a plot of the impedance plotted against the width of the strip is given. As can be seen a width of 700 μm yields an impedance of 50 Ω. In the past however microstrips with a width of 600 μm were used by Philips Research. In Figure 4.4 can be seen that this width does not result in an impedance of 50 Ω. However since the microstrip lines that were simulated were covered with a moulding layer, see Section 3.2, with $\epsilon_r = 3$ the value of 50 Ω could still be obtained.
A number of computer aided design (CAD) programs were used to compare the results. The CAD programs assume that there is air above the strip. To be able to make a good comparison

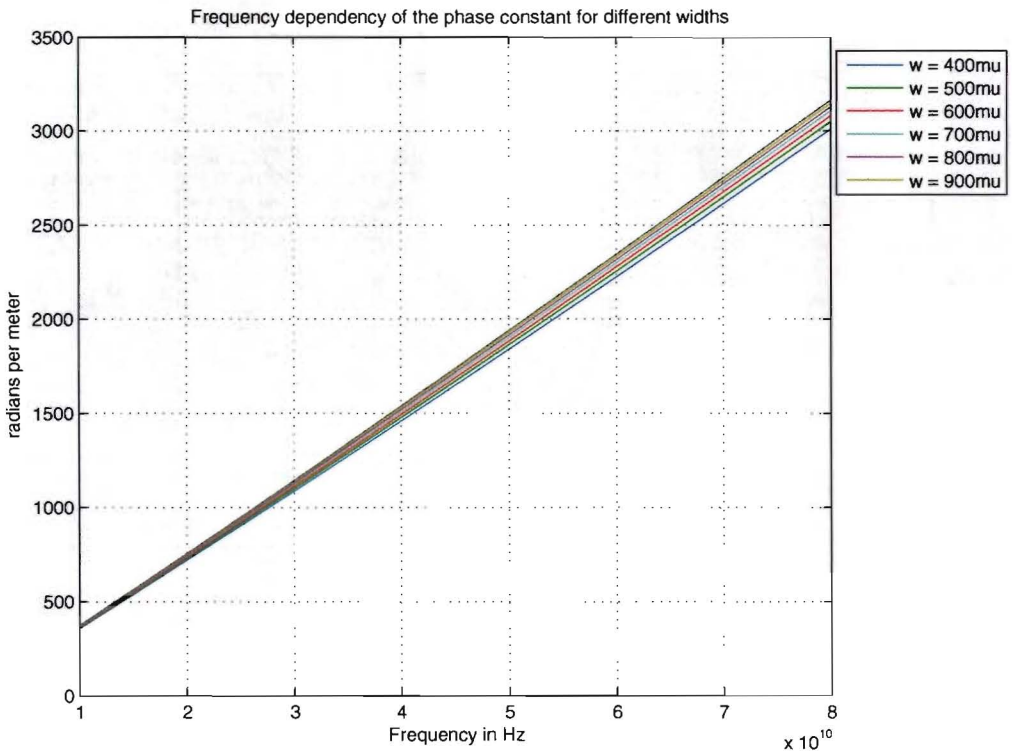

Figure 4.5: Phase constant of the microstrip line for different widths W plotted against the frequency

simulations in ADS were performed on a microstrip line with a width of 700 μm and no covering moulding layer as well. The programs TX-line from Applied Wave Research, inc., Polar SI 9000 Field Solver from Polar Instruments and Appcad from Agilent Technologies were used. To perform a frequency dependent simulation Advanced Design Systems from Agilent was used, as well as a tool Linecalc included in the ADS package. The Appcad program is not able to calculate the attenuation factor. The model described above was implemented in Matlab from Mathworks. The results from the CAD programs are displayed in Table 4.2. As can be seen in Table 4.2, the

	TX-line	Appcad	Linecalc	Polar	Matlab	ADS
Z_0	49.62 Ω	48.21 Ω	48.24 Ω	47.8 Ω	50.98 Ω	49.90 Ω
ϵ_{ref}	3.25	3.14	3.12	3.04	3.19	3.21
α	48.42 dB/m	N.A.	50.09 dB/m	48.7 dB/m	51.92 dB/m	53.99 dB/m
β	906.6 rad/m	890.6 rad/m	891.7 rad/m	877 rad/m	904.2 rad/m	917.5 rad/m

Table 4.2: Comparison between line calculation programs for a microstrip line at 24 GHz, with dimensions: $W = 700\ \mu m$, $t = 28\ \mu m$, $h = 330\ \mu m$, $\epsilon_r = 4$.

values for the characteristic impedance agree reasonably well for all the investigated programs. The largest difference from the mean value of 49.13 Ω can be found with the program written in Matlab and is 1.86 Ω which is 3.77% of the mean value. The Appcad and Linecalc programs seem to agree very well on the relation between relative permittivity and characteristic impedance and phase constant. There is a difference in method of calculation between the TX-line program

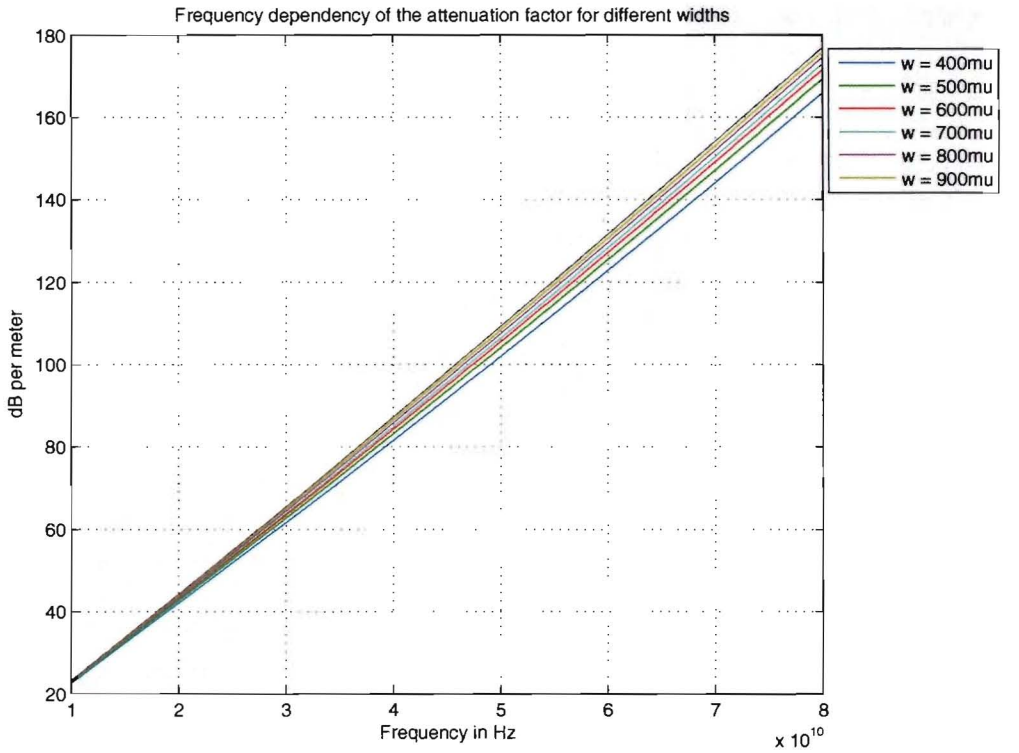

Figure 4.6: Attenuation factor of the microstrip line for different widths W plotted against the frequency

and the method implemented in Matlab. This can be seen in the relation between the relative permittivity and the characteristic impedance. The model used in TX-line is however not publicly available.

The values in the ADS column were obtained by making use of a special port and a build in model. This so called single port is an external port and is calibrated so no undesired reactive effects of the port excitations exists. For more information about this process see Appendix B. Since a full wave simulator was available the propagation constant and characteristic impedance can also be obtained by extracting these parameters from the simulated s-parameters. This is a complicated process. To maintain continuity this is described in Appendix C in row 1a. The values calculated with ADS seem to agree with the programs that use a model to calculate the parameters. It can be concluded that the investigated programs can be used as tools for fast prediction of the characteristic impedance, attenuation factor and phase constant of a microstrip line. The effective permittivity in the ADS column was obtained with:

$$\epsilon_r = 3 \times 10^8 (\beta/\omega)^2 \tag{4.11}$$

4.2 Coplanar waveguide

In a coplanar waveguide (CPW) the ground is located at the same side of the dielectric substrate as the strip conductor. The cross section of the coplanar waveguide is depicted in Figure 4.7. The

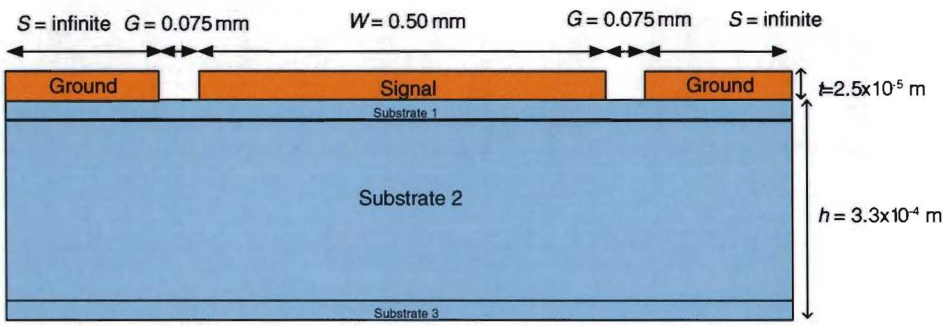

Figure 4.7: cross section of the coplanar waveguide

CPW consists of two slots of width S and a metal strip with width W. The signal is connected to the metal strip between the slots. The CPW feed lines were used in antenna designs which have a slot. One of the advantages of the coplanar structure is that it can be easily connected to other components which have a coplanar structure, i.e. MESFETS. Consequently they are suitable for integration in monolithic microwave integrated circuits (MMICs). The metal strips along

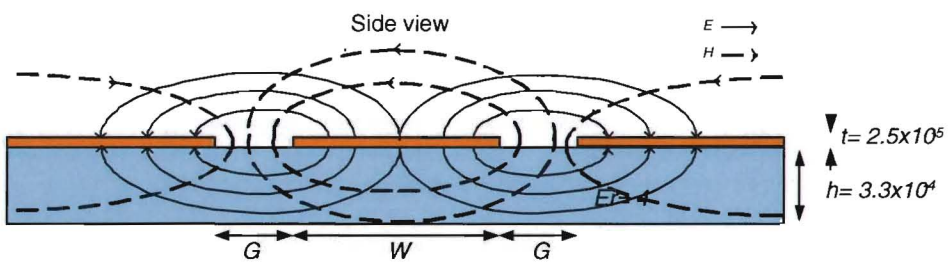

Figure 4.8: The electromagnetic field of a coplanar waveguide

the outer edges of the slots are connected to ground. The electromagnetic fields of a coplanar waveguide are displayed in Figure 4.8. The calculation of the characteristic impedance of the CPW involves conformal mapping. Conformal mapping is a complicated process which is beyond the scope of this text. For more details about the conformal mapping process see reference [5]. In this Section formulas will be given that can be used to calculate the characteristic impedance, effective relative permittivity, propagation constant and the attenuation factor. The equations were also obtained by curve fitting to numerical simulations and are described in reference [5]. The quasi-static approximation of the characteristic impedance, Z_{0cpw}, with an infinite thick dielectric

substrate is given by:

$$Z_{0cpw} = \frac{30\pi}{\sqrt{\epsilon_{re}}}\frac{K(k_1')}{K(k_1)} \tag{4.12}$$

$$k_1 = \frac{W}{2G+W} \tag{4.13}$$

$$k_1' = \sqrt{1-k_1^2} \tag{4.14}$$

$$\epsilon_{re} = \frac{\epsilon_r+1}{2} \tag{4.15}$$

where $K(k)$ is the complete elliptic integral of the first kind and $K(k')$ is its complement. The used substrate has a finite thickness h. Therefore a modified relative permittivity is introduced.

$$\epsilon_{re} = 1+\frac{\epsilon_r-1}{2}\frac{K(k_2)}{K(k_2')}\frac{K(k_1')}{K(k_1)} \tag{4.16}$$

with k_2

$$k_2 = \frac{\sinh(\pi a/2h)}{\sinh(\pi b/2h)} \tag{4.17}$$

The equations for a and b are given below. The ϵ_{re} obtained in (4.16) is substituted, in (4.12). The obtained values are only valid for an infinitesimally thin metallic strip conductor. The CPW used has a strip conductor with thickness t. To account for this effect, effective values for the width of the slot, G, and the width of the strip conductor, W, are introduced.

$$G_e = G+\Delta \tag{4.18}$$

$$W_e = W-\Delta \tag{4.19}$$

$$\Delta = (1.25t/\pi)[1+\ln(4\pi G/t)] \tag{4.20}$$

$$\epsilon_{re}^t = \epsilon_{re}-\frac{0.7(\epsilon_{re}-1)t/G}{[\frac{K(k)}{K(k')}]+0.7t/G} \tag{4.21}$$

The values for G_e and W_e obtained in (4.18) and (4.19) replace the old widths in Equation (4.13). The value for ϵ_{re}^t obtained in (4.21) is filled in, in Equation (4.12). The quasi-static approximations are now complete. A frequency depended value for ϵ_{re}^t is now introduced.

$$\sqrt{\epsilon_{re}(f)} = \sqrt{\epsilon_{re}(0)}+\frac{\sqrt{\epsilon_r}-\sqrt{\epsilon_{re}(0)}}{1+D(f/f_{50})^{-1.8}} \tag{4.22}$$

$$D = e^{u\ln(2a/(b-a))+v}$$

$$u = 0.54-0.64p+0.015p^2$$

$$v = 0.43-0.86p+0.54p^2$$

$$p = \ln(2a/h)$$

$$a = W/e$$

$$b = (W+2G)/2$$

The cutoff frequency for the TE_0 mode is f_{50} and is given by:

$$f_{50} = \frac{c}{4h\sqrt{\epsilon_r-1}} \tag{4.23}$$

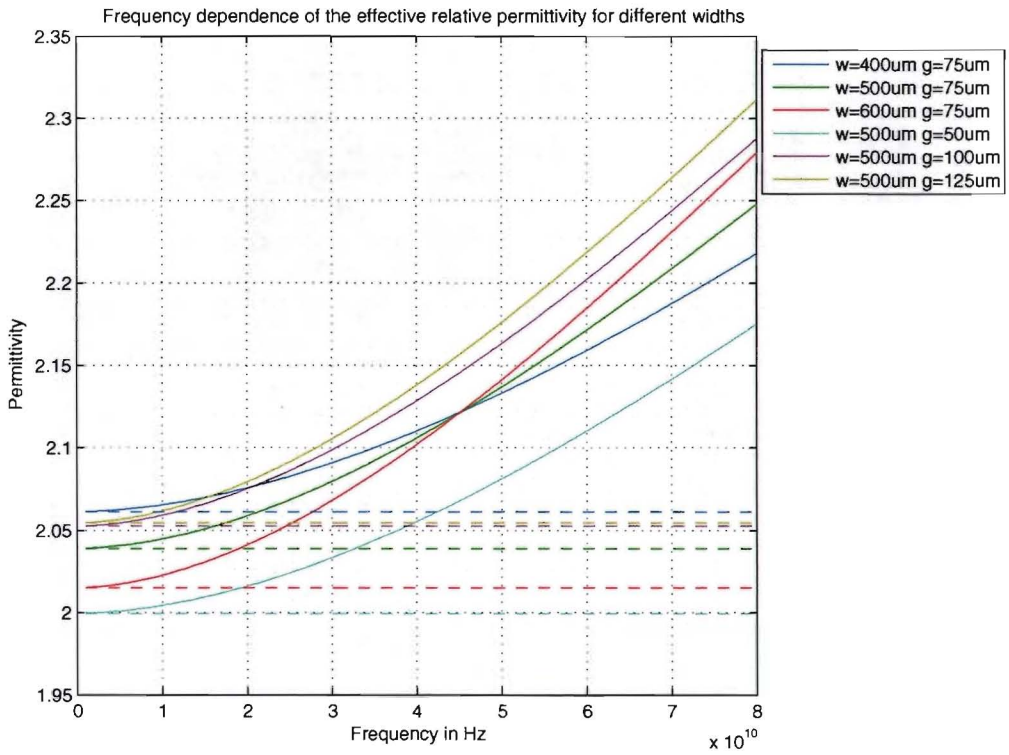

Figure 4.9: Relative permittivity of the coplanar waveguide for different widths W and G, plotted against the frequency (scale 1 GHz till 80 GHz), the dashed lines indicate the quasi static approximation of the relative permittivity.

A typical value of the cutoff frequency on the substrate described in Section 3.2 is 131 GHz. The value for ϵ_r was set to 4 and the height of the substrate was set to 330 μm. This frequency is well above the frequencies used in this report. A plot of the frequency dependent relative permittivity is depicted in Figure 4.9. In Figure 4.9 can be seen that for frequencies lower than 1 GHz the static value of the relative permittivity becomes comparable to the frequency dependent permittivity. The frequency dependent relative permittivity exhibits an asymptotic behavior for high frequencies. The permittivity converges to the relative permittivity of the dielectric substrate. The frequency dependent value of $\epsilon_{re}(f)$ can now be used to calculate the frequency dependent Z_{0cpw} by filling in the value of $\epsilon_{re}(f)$ from Equation 4.22, into Equation 4.12. The frequency dependent characteristic impedance is depicted in Figure 4.10. The value of $\epsilon_{re}(f)$ from Equation 4.22 can also be used to calculate the propagation constant β similar to way it was calculated for the microstrip line. The value for the attenuation constant due to the losses in the dielectric substrate, α_d, is given by 4.10 with $\epsilon_{re}(f)$ obtained in Equation 4.22. The value for the attenuation due to the imperfect conductor, α_c, is given by:

$$\alpha_c = \frac{8.68 R_s \sqrt{\epsilon_{re}(f)}}{480\pi K(k_1)K'(k_1)(1-k_1^2)} \left\{ \frac{1}{a}\left[\pi + \ln\left(\frac{8\pi a(1-k_1)}{t(1+k_1)}\right)\right] + \frac{1}{b}\left[\pi + \ln\left(\frac{8\pi b(1-k_1)}{t(1+k_1)}\right)\right]\right\} \quad (4.24)$$

The result for the phase constant and attenuation factor are depicted in figures 4.11 and 4.12.

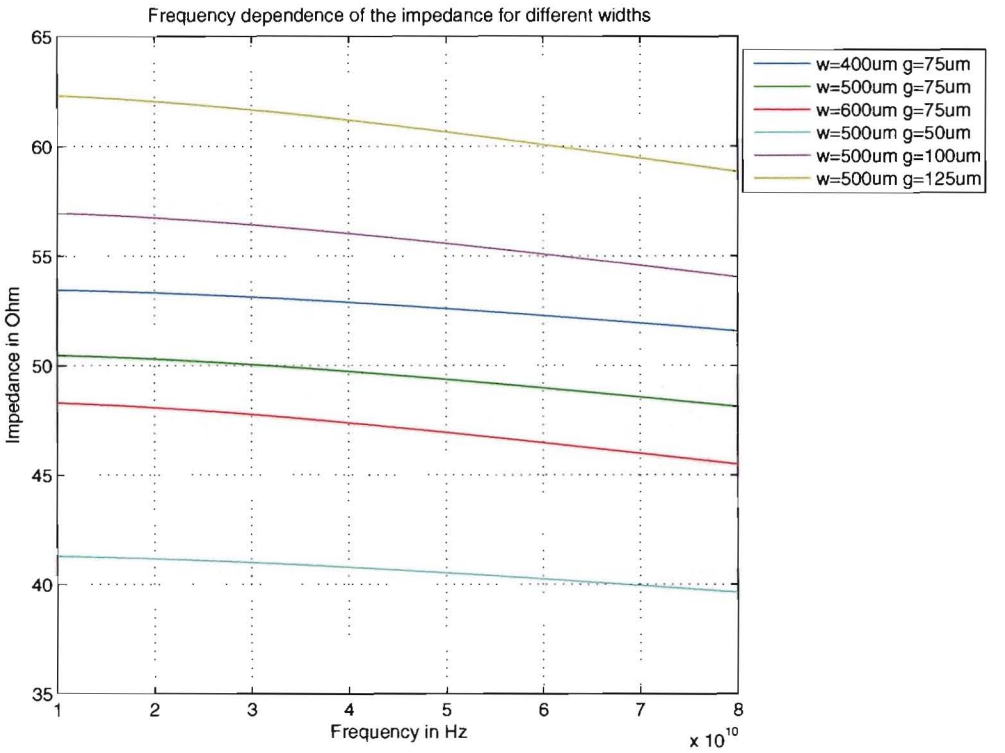

Figure 4.10: Characteristic impedance of the coplanar waveguide for different strip and gap widths.

Width and Gap Width	ϵ_r at 0 GHz	ϵ_r at 24 GHz	ϵ_r at 60 GHz	ϵ_r at 77 GHz	Difference in % at 24 GHz	Difference in % at 60 GHz	Difference in % at 77 GHz
w = 400 μm g = 75 μm	2.09	2.11	2.19	2.24	0.96%	4.78 %	7.18 %
w = 500 μm g = 75 μm	2.06	2.09	2.20	2.26	1.46%	6.80 %	9.71 %
w = 600 μm g = 75 μm	2.04	2.07	2.21	2.29	1.47%	8.33 %	12.25 %
w = 500 μm g = 50 μm	2.03	2.05	2.14	2.20	0.99%	5.42 %	8.37 %
w = 500 μm g = 100 μm	2.07	2.10	2.22	2.30	1.45 %	7.25 %	11.11 %
w = 500 μm g = 125 μm	2.07	2.10	2.24	2.32	1.45%	8.21 %	12.08 %

Table 4.3: Difference in percentages between the static permittivity and the frequency dependent permittivity for different widths of the strip and the gap of the coplanar waveguide at the three frequencies considered in this project.

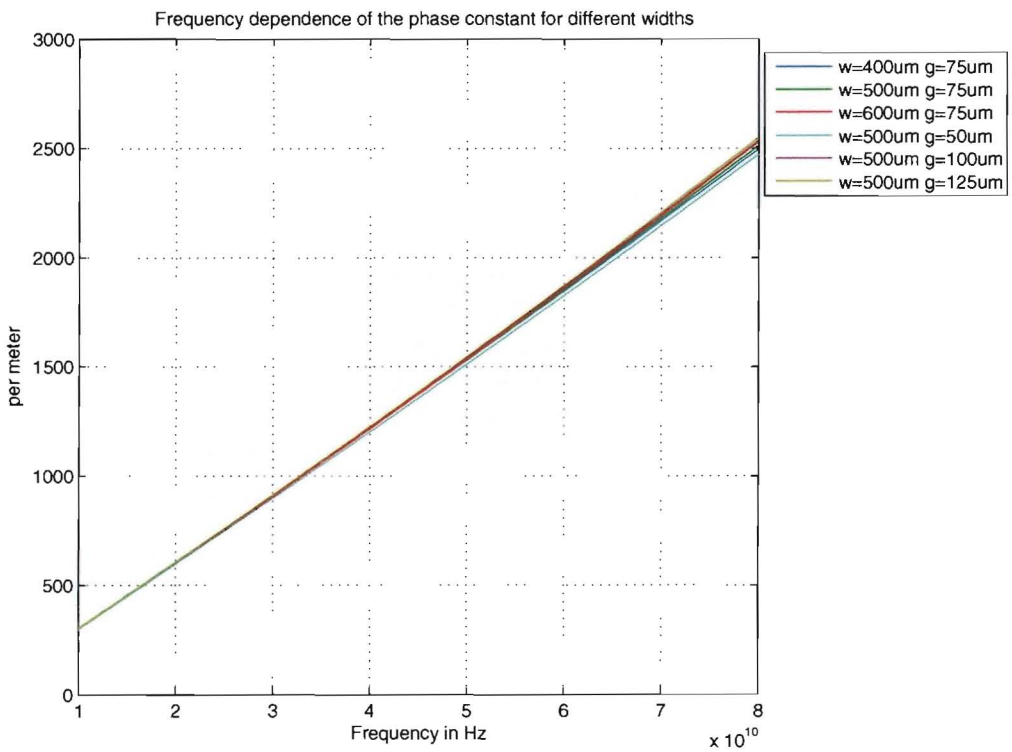

Figure 4.11: Phase constant of the coplanar waveguide for different strip and gap widths.

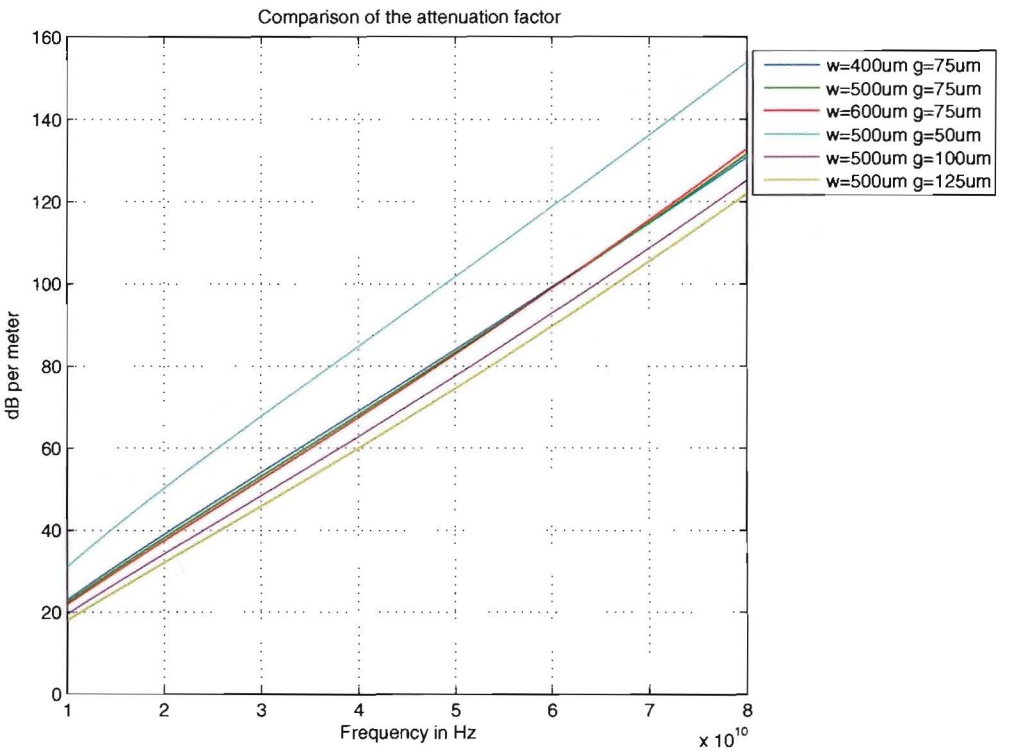

Figure 4.12: Attenuation factor of the coplanar waveguide for different strip and gap widths.

In addition to the dielectric loss and the conductor loss other forms of loss exist in coplanar waveguides. These losses are called the radiation and surface wave losses. Radiation loss comes from parasitic modes. The parasitic mode in a coplanar waveguide is the odd mode, the voltages in the slots are in anti-phase. This can be avoided by using symmetric circuits. Surface wave loss comes from another parasitic mode in the dielectric substrate.
The obtained values are also compared to results obtained with the same CAD programs used for the microstrip line. The obtained values are given in Table 4.4.

	TX-line	Appcad	Linecalc	Polar	Matlab	ADS
Z_0	50.68 Ω	30.5 Ω	50.01 Ω	50 Ω	50.18 Ω	52.21 Ω
ϵ_{ref}	2.12	2.26	2.12	N.A.	2.07	2.00
α	42.01 dB/m	N.A.	46.71 dB/m	58.4 dB/m	44.04 dB/m	22.89 dB/m
β	731.8 rad/m	760 rad/m	732.2 rad/m	735 rad/m	722.6 rad/m	710.00 rad/m

Table 4.4: Comparison between line calculation programs for a coplanar waveguide at 24 GHz, with dimensions: $W = 500\mu m$, $G = 75\mu m$, $t = 28\mu m$, $h = 330\mu m$ and $\epsilon_r = 4$

The Appcad program produces wrong results when the thickness of the conductor strip is large. When the thickness of the conductor strip is reduced Appcad produces comparable results as the other programs. Problems arise when modelling the finite thickness in the method of moments simulator. This problem was investigated by testing different methods to extract the transmission line parameters from the s-parameters. To maintain continuity here this problem is treated in Appendix C. The values of the last column were obtained by simulating the CPW with thick conductors and internal ports. Thereafter a second CPW which was slightly longer was simulated. The two simulations were then combined. This method is treated in more detail in Appendix C. The values correspond to the values of row 6 in this appendix. In the last column can be seen that the value for the attenuation differs strongly from the values of the attenuation factors obtained with the CAD programs. Further research is needed to solve this problem.

4.2.1 Comparison between microstrip line and coplanar waveguide

In this Section the losses of the microstrip line will be compared to the losses of the coplanar waveguide. Therefore the losses of the microstrip line and the coplanar waveguide have been plotted, see Figure 4.13. Every line is designed to have an characteristic impedance of 50 Ω.

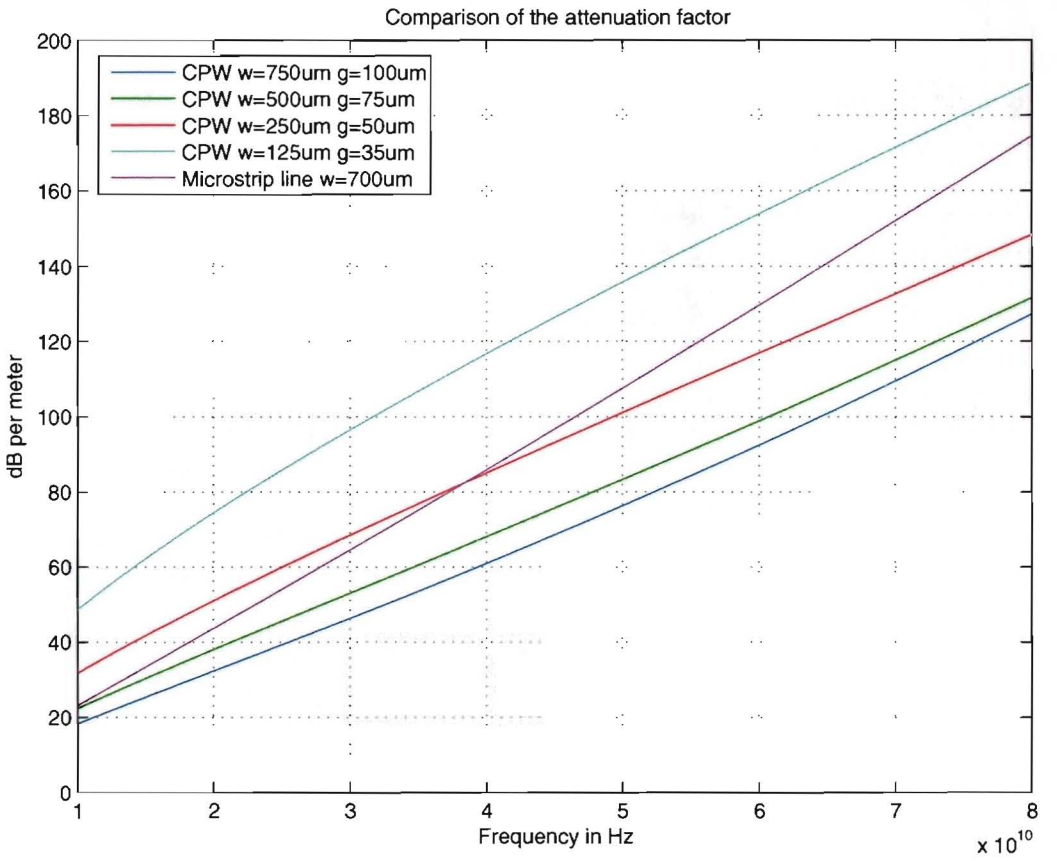

Figure 4.13: Comparison of the attenuation factor of the coplanar waveguide and the microstrip line with characteristic impedances of 50 Ω.

As can be seen the coplanar waveguide with a wide conductor strip has the lowest losses. It is expected that by further widening the strip a decrease in attenuation can be achieved. However the model that was implemented in Matlab does not perform well with structures larger than depicted. Therefore the optimum coplanar waveguide cannot be depicted.

Type	size	α at 24 GHz	α at 60 GHz
CPW	$w = 750\mu m, g = 100\mu m$	0.038 dB per mm	0.092 dB per mm
CPW	$w = 500\mu m, g = 75\mu m$	0.044 dB per mm	0.099 dB per mm
CPW	$w = 250\mu m, g = 50\mu m$	0.059 dB per mm	0.12 dB per mm
CPW	$w = 125\mu m, g = 35\mu m$	0.084 dB per mm	0.15 dB per mm
Microstrip line	$w = 700\mu m$	0.051 dB per mm	0.13 dB per mm

Table 4.5: The attenuation factor at 24 and 60 GHz for the coplanar waveguide and the microstrip line, with a characteristic impedance of 50 Ω and different sizes.

When constructing a microstrip line with a characteristic impedance of 50 Ω there is only one suitable width. The coplanar waveguide however, offers more freedom to chose the size of the strip and the size of the gap. This freedom can then be used to construct a transmission line with a lower loss. When a transmission line is required with a certain characteristic impedance and attenuation factor, this kind of figure could also be used as a guide to find a suitable structure.

4.3 Cascaded transmission lines

A transmission line can be seen as a two port network. Consequently a transmission line can be described by:

$$\begin{bmatrix} V_o(z) \\ I_o(z) \end{bmatrix} = T_F \begin{bmatrix} V_i(z) \\ I_i(z) \end{bmatrix} \tag{4.25}$$

where $V_o(z)$ and $I_o(z)$ are the output voltage and current respectively and $V_i(z)$ and $I_i(z)$ are the input voltage and current respectively, T_F is a 2x2 transmission matrix called the forward transmission matrix. Recalling that the voltage $V(z)$ and current $I(z)$ at a distance z from the point of excitation are given by:

$$\begin{aligned} V_s(z) &= V_0^+ e^{-\gamma z} + V_0^- e^{\gamma z} \\ I_s(z) &= I_0^+ e^{-\gamma z} + I_0^- e^{\gamma z} \end{aligned}$$

where the time factor $e^{j\omega t}$ has been omitted. The values for V_0^+ and V_0^- can be derived using the lumped circuit depicted in Figure A.1. Where the transmission line is driven by a voltage V_0 and a current I_0.

$$V^+ = \frac{V_0 + Z_0 I_0}{2} \tag{4.26}$$

$$V^- = \frac{V_0 - Z_0 I_0}{2} \tag{4.27}$$

The current at a distance z from the source can now be written as:

$$I_s(z) = \frac{V_0 + Z_0 I_0}{2Z_0} e^{-\gamma z} + \frac{V_0 - Z_0 I_0}{2Z_0} e^{\gamma z} \tag{4.28}$$

After rearranging the terms and applying: $e^{kx} + e^{-kx} = 2\cosh(kx)$ and $e^{kx} - e^{-kx} = 2\sinh(kx)$, Equation 4.28 can be written as:

$$I_s(z) = I_0 \cosh(\gamma z) + \left(\frac{V_0}{Z_0}\right) \sinh(\gamma z) \tag{4.29}$$

And the voltage can be written as:

$$V_s(z) = \frac{V_0 + Z_0 I_0}{2} e^{-\gamma z} + \frac{V_0 - Z_0 I_0}{2} e^{\gamma z} \tag{4.30}$$

$$V_s(z) = V_0 \cosh(\gamma z) + Z_0 I_0 \sinh(\gamma z) \tag{4.31}$$

Combining equations 4.29 and 4.31 the matrix T_F is obtained as:

$$T_{F,k} = \begin{bmatrix} A_K & B_K \\ C_K & D_K \end{bmatrix} = \begin{bmatrix} \cosh(\gamma z) & Z_0 \sinh(\gamma z) \\ \left(\frac{1}{Z_0}\right) \sinh(\gamma z) & \cosh(\gamma z) \end{bmatrix} \tag{4.32}$$

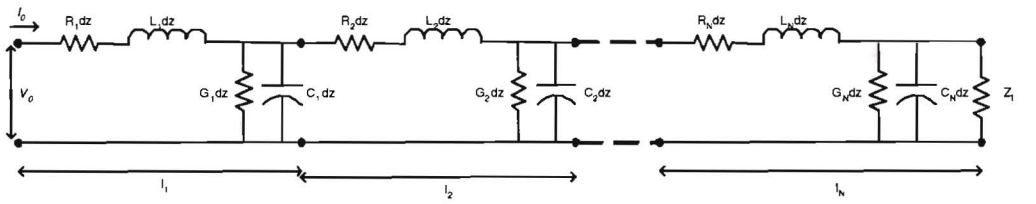

Figure 4.14: Coupled transmission line with different sections

The forward transmission matrix can also be used to describe a network depicted in Figure 4.14. In this network N transmission lines are connected. Since the transmission matrix describes the relation between the two ports it can be easily used to calculate an equivalent transmission matrix for the connected transmission lines:

$$T_{F_{tot}} = \prod_{n=1}^{N} T_n \tag{4.33}$$

Where T_n is the forward transmission matrix of the nth segment, with Z_{0_n}, length l_n and propagation constant γ_n. The cascade of transmission lines can now be described with the total forward transmission matrix, $T_{F_{tot}}$.

4.4 Coplanar waveguide transitions

In this Section the problem of connecting two coplanar waveguides with the same ratio of W to G, the same characteristic impedance, but with a different width W of the strip is treated. As can be seen in Figure 4.12, it can be advantageous to use a wide strip in order to achieve a low loss. When such a low loss cpw has to be connected to a standard component, i.e. a connector, it might be necessary to change the width of the strip while keeping the same characteristic impedance. To achieve such a connection a tapered transition element as depicted in Figure 4.15

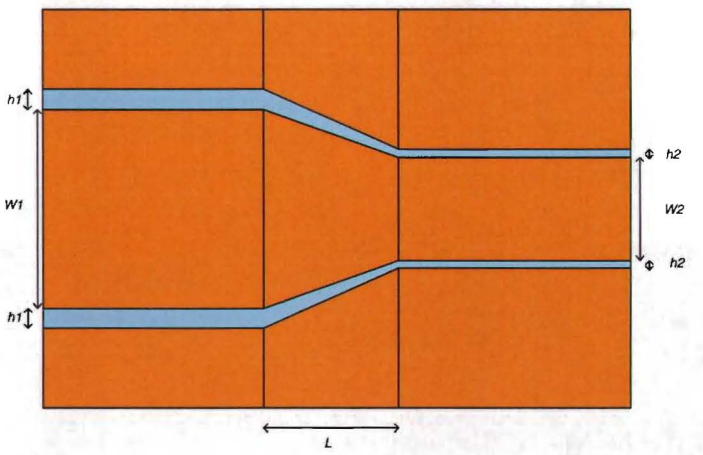

Figure 4.15: Transition element with dimensions: W1= 500 μm, G1=74 μm, W2=260 μm and G2=75 μm and t= 25 μm.

can be used. The theory treated in Section 4.3 is used to calculate the characteristic impedance of

this transition. Therefore the transition is divided into N sections with width W_n and gap width G_n. Then the transmission matrix of each section is calculated. Thereafter the theory of coupled transmission lines is used, the load impedance of the transition is equal to the characteristic impedance of the transmission line on the right hand side, which is assumed to be 50 Ω. This coplanar waveguide has a ground plane. When the dimensions of the coplanar waveguide on the right are filled in one of the CAD programs described in Section 4.2 a characteristic impedance is obtained which is not 50 Ω. The ground plane however changes the characteristic impedance into 50 Ω. The coplanar waveguide on the left side and the transition element do not have a ground plane. Simulations of the coplanar waveguide with ground plane done at Philips Research in the past indicate that the attenuation factor of the lines with a ground plane is 0.06 dB/mm at 24 GHz which is comparable to the attenuation factor of coplanar waveguides without a ground plane, see Table 4.5 row 3. A sketch of the connector is depicted in Figure 4.16. A simulation

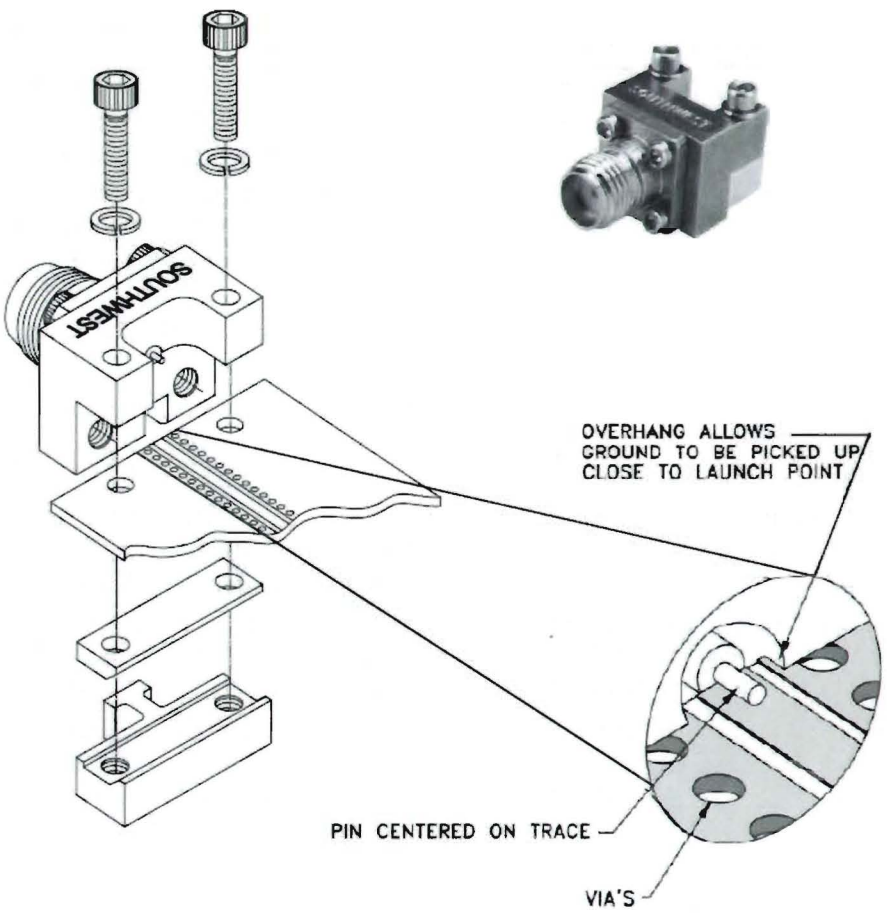

Figure 4.16: The used connector, the length of the grounded coplanar waveguide used in these designs is 5.2 mm

of characteristics of the transition has been made by implementing the cascaded transmission lines theory in Matlab. The model described in 4.2 was used to compute the characteristics of each section. The implementation was first tested on a transmission line without a taper. The results agreed with the results obtained by using the model described in 4.2. Next the cascaded

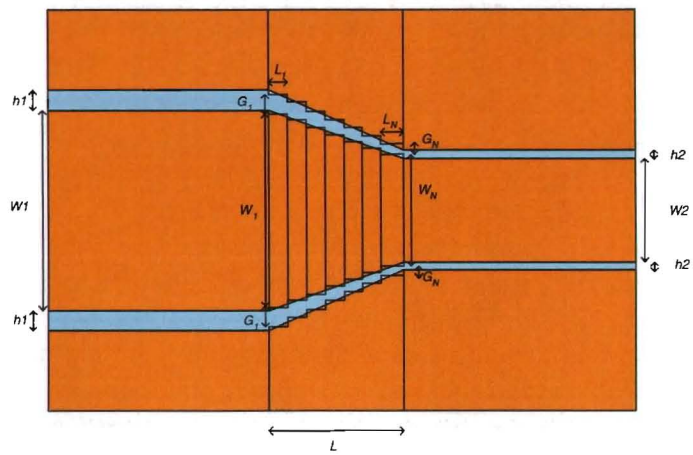

Figure 4.17: Sectioned transition with dimensions: W1= 500μm, G1=74 μm, W2=260 μm and G2=75 μm and t= 25 μm.

model was used to find the characteristics of the tapered transition. The results are depicted in the figures below. Because the calibration technique using two lines that slightly differ in length cannot be applied to the transitions. The choice was made to model the transition as two slots excited by two calibrated ports.
The result from the Matlab model is depicted in blue in Figure 4.18, the result from ADS is depicted in red.

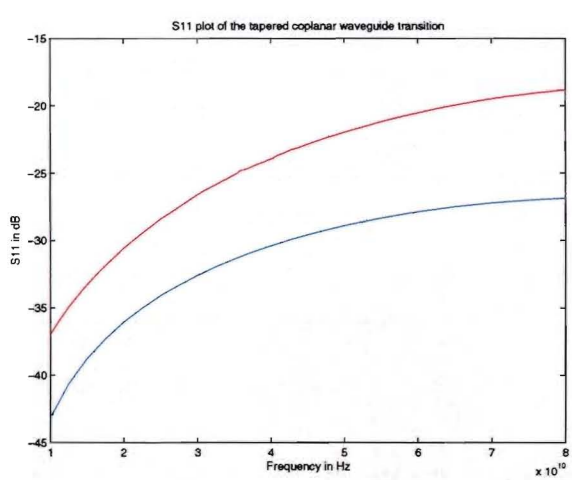

Figure 4.18: The S11 plot of the tapered coplanar waveguide transition with sizes: W1= 500μm, G1=74 μm, W2=260 μm and G2=75 μm and t= 25 μm.

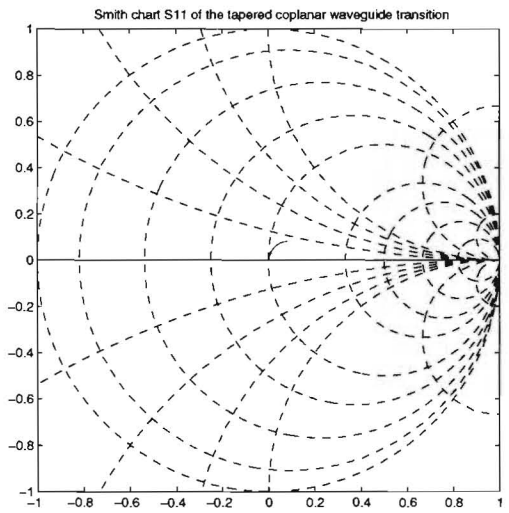

Figure 4.19: The smith chart of the tapered coplanar waveguide transition with sizes: W1= 500 μm, G1=74 μm, W2=260 μm and G2=75 μm and t= 25 μm.

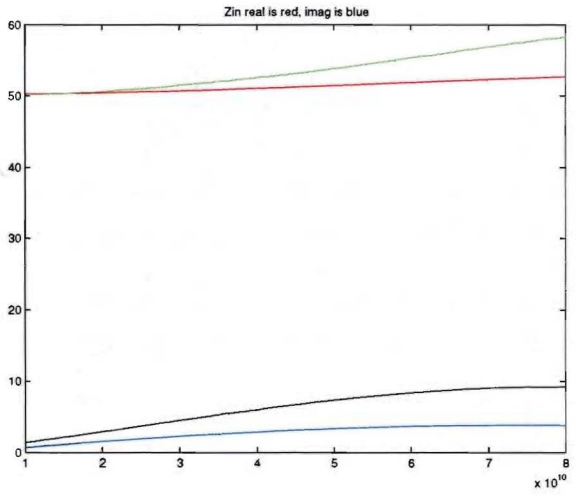

Figure 4.20: The input impedance of the tapered coplanar waveguide transition with sizes: W1= 500μm, G1=74 μm, W2=260 μm and G2=75 μm and t= 25 μm.

The S11 return loss from the Matlab model is depicted in red in Figure 4.19, the S11 return loss from ADS is depicted in blue. The real part of the input impedance, obtained with the Matlab model, in Figure 4.20 is depicted in red, the imaginary part is depicted in blue. The real part of the input impedance, obtained with the ADS, in Figure 4.20 is depicted in green, the imaginary part is depicted in black. Two set of simulations were done. In the first set the thickness of the metal strips was set to 25 μm. These results are compared to the results obtained with ADS Momentum. As is explained in Appendix C, the metal thickness is not modelled with this configuration. This is the cause of the difference in values. To verify the results a second set of measurements was made. In this set the metal thickness was set to 0 μm. With this configuration the results from the model implemented in Matlab and the results of ADS Momentum are comparable. The S11 return loss

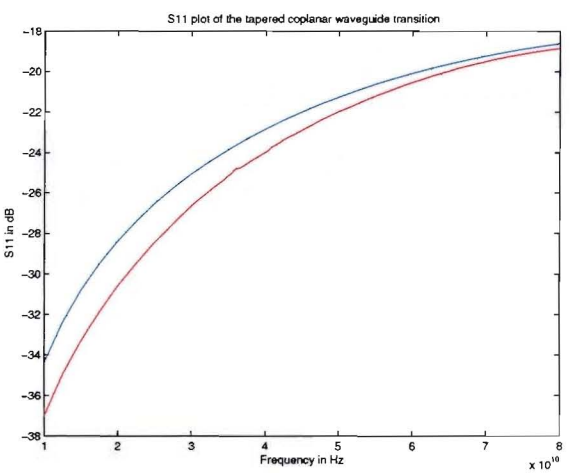

Figure 4.21: The S11 plot of the the tapered coplanar waveguide transition with sizes: W1= 500μm, G1=74 μm, W2=260 μm and G2=75 μm and t= 0 μm.

from the Matlab model is depicted in blue in Figure 4.21, the S11 return loss from ADS is depicted in red.

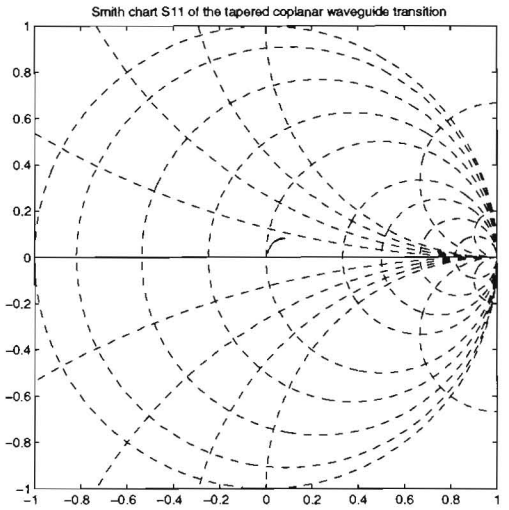

Figure 4.22: The smith chart of the tapered coplanar waveguide transition with sizes: W1= 500 μm, G1=74 μm, W2=260 μm and G2=75 μm and t= 0 μm.

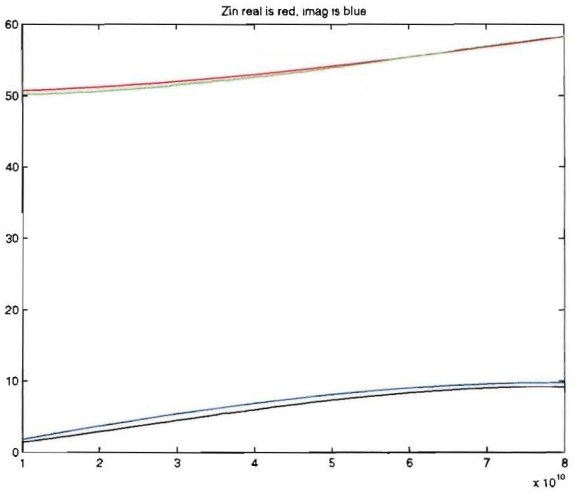

Figure 4.23: The input impedance of the tapered coplanar waveguide transition with sizes: W1= 500μm, G1=74 μm, W2=260 μm and G2=75 μm and t= 0 μm.

The result from the Matlab model is depicted in red in Figure 4.22, the result from ADS is depicted in blue. The real part of the input impedance, obtained with the Matlab model, in Figure 4.23 is depicted in red, the imaginary part is depicted in blue. The real part of the input impedance, obtained with the ADS, in Figure 4.23 is depicted in green, the imaginary part is depicted in black.
The model implemented in Matlab, with t= 25 μm, produces the most accurate results for the real configuration wherein the thickness of the metal strip is not zero. The tapered transition elements do not produce serious reflections and are matched reasonably well to the characteristic impedance of 50 Ω.

4.5 Conclusions concerning transmission lines at high frequencies

In this section the results of the investigation of transmission lines were presented. In this Section the conclusions of this chapter are summarized. The first transmission line that was investigated was the microstrip line. The frequencies used in this project are high compared to the frequencies used in the past by Philips Research. Therefore the frequency dependency of the transmission line parameters Z_0, γ, β and α were investigated. It was found that a microstrip line with a width of 700 μm has a characteristic impedance of 50 Ω. The frequency dependent behavior is summarized in Table 4.6. Several CAD programmes were tested. These CAD programmes work well. The result of this test is summarized in Table 4.2.
The coplanar waveguide transmission line was also investigated. The coplanar transmission line with dimensions $W = 500$ μm and $G = 75$ μm was chosen. The frequency dependent behavior of the effective permittivity was investigated. In Table 4.7 the frequency dependent behavior of the the chosen waveguide is given. The CAD programs that were tested with the microstrip line

Width	ϵ_r at 0 GHz	ϵ_r at 24 GHz	ϵ_r at 60 GHz	ϵ_r at 77 GHz	Difference in % at 24 GHz	Difference in % at 60 GHz	Difference in % at 77 GHz
w = 700 μm	3.08	3.19	3.40	3.47	3.57 %	10.39 %	12.66 %

Table 4.6: Difference in percentages between the static permittivity and the frequency dependent permittivity for the chosen microstrip line at the three frequencies considered in this project.

Width and Gap Width	ϵ_r at 0 GHz	ϵ_r at 24 GHz	ϵ_r at 60 GHz	ϵ_r at 77 GHz	Difference in % at 24 GHz	Difference in % at 60 GHz	Difference in % at 77 GHz
w = 500 μm g = 75 μm	2.06	2.09	2.20	2.26	1.46%	6.80 %	9.71 %

Table 4.7: Difference in percentages between the static permittivity and the frequency dependent permittivity of the chosen coplanar waveguide at the three frequencies considered in this project.

were also tested with the coplanar waveguide. The results were given in Table 4.4. One of these programs, Appcad, was not able to model a coplanar waveguide with a finite metal thickness. The other programs performed well. Problems arose when the transmission line parameters were extracted from ADS. This problem was treated in Appendix C. A solution was found by using two coplanar waveguides which slightly differ in length. However the attenuation per meter was lower than expected. Further investigation is needed to solve this problem. The connector, transition element and transmission line form a chain which is connected to an antenna. Further in this report, Chapter 6 and Chapter 5 two types of antennas are described. These antennas use a coplanar waveguide and a microstrip line respectively. The characteristics of the feeding structure based on the coplanar waveguide is summarized in Table 4.8.

Frequency	attenuation transmission line	Characteristic impedance transmission line	return loss transition element	return loss connector	attenuation connector footprint
24 GHz	0.044 dB/mm	50.2 Ω	S11 < -26 dB	S11<-23 dB	0.068 dB/mm
60 GHz	0.099 dB/mm	48.0 Ω	S11 < -20 dB	S11<-10 dB	0.12 dB/mm

Table 4.8: Characteristics of the feeding structure based on the coplanar waveguide with dimensions: w = 500 μm and g =75 μm. Values based on the model implemented in Matlab. The values for the connector were simulated in ADS.

The feeding structure based on the microstrip line was not connected to a connector. The microstrip line has to be transformed into a coplanar waveguide to be connected to the connector. In this report no such feeding structure was developed.
A comparison of the microstrip line and the coplanar waveguide was presented. It was shown that the loss per mm in dB was lower for a coplanar waveguide see Table 4.5.

Chapter 5

Microstrip antennas

In this chapter a short summary will be given of the antenna designs that are based on the microstrip patch antenna design. The microstrip patch antenna was the first design that was simulated in this project. This design was chosen as a starting point because of its simplicity. The structure consists of a metal patch and a ground plane separated by a dielectric substrate. The principles of operation of the microstrip antenna (MSA) are described in Section 5.1 using the transmission line model. Next the results of the MSA are presented in Section 5.2. In sections 5.3 and 5.4 two variations of the MSA are presented. In the last Section conclusions are drawn about the performance of the discussed antennas.

5.1 The transmission line model

A microstrip antenna confines wave energy to a small region. This is achieved with the resonant behavior of a finite guided structure that supports a standing wave mode. The electromagnetic energy radiates from that part of the antenna where it is open to free space. When the characteristic impedance of the feeding structure matches the characteristic impedance of the microstrip antenna the power is delivered from the feed line to the antenna. In this case there is little reflection. The incoming power is then radiated by the antenna into free space.

The transmission line model assumes that the microstrip patch antenna can be represented by a transmission line with two radiating slots at the ends, see reference [6]. As was the case with the microstrip line the patch antenna supports a quasi-TEM mode. To support the fundamental TM_{10} mode the length of the patch must be slightly smaller than $\lambda_d/2$. Where λ_d is the wavelength in the dielectric medium. Because the main mode is the TM_{10} there is no variation of the electric field along the width of the patch, W. However the field various one $\lambda_d/2$ cycle along the length of the patch, L, see Figure 5.1. The fields along the edges of the patch can be separated into tangential and normal fields with respect to the ground plane. The normal components along the width are in opposite directions and thus 180° out of phase since the patch is $\lambda_d/2$ long. Therefore these fields cancel each other in the broadside direction. The tangential fields are in phase and hence combine to give a radiating field normal to the ground plane. As can be seen in the side view image in Figure 5.1, most of the electric field lines reside in the substrate and parts of some lines reside in the air. Therefore the material surrounding the patch antenna can not be

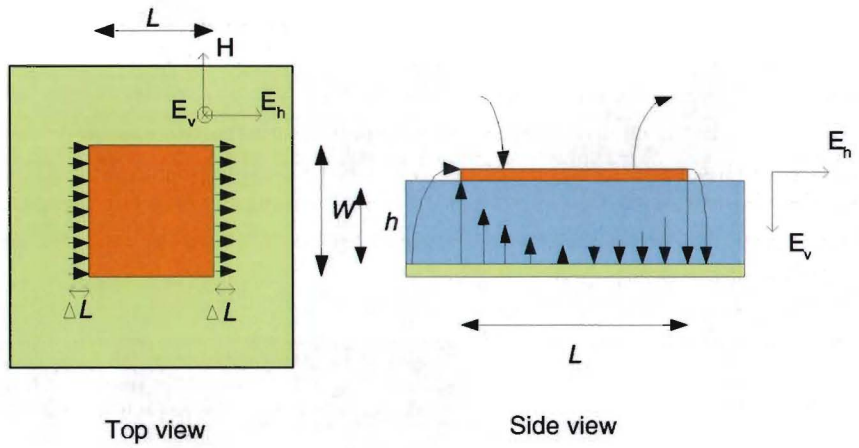

Figure 5.1: The EM fields of the patch antenna

considered homogeneous. To solve this problem an effective permittivity, ϵ_{reff} is introduced:

$$\epsilon_{reff} = \frac{\epsilon_r + 1}{2} + \frac{\epsilon_r - 1}{2} \frac{1}{\sqrt{1 + 10\frac{h}{W}}} \tag{5.1}$$

where ϵ_r is the permittivity of the substrate, see reference [6]. Because of the fringing fields along the width of the antenna, the electrical width of the patch, L_{eff}, is larger than the physical width. The effective width, L_{eff}, is be given by:

$$L_{eff} = L + 2\Delta L \tag{5.2}$$

$$\Delta L = 0.412h \frac{(\epsilon_{reff} + 0.3)(\frac{W}{h} + 0.264)}{(\epsilon_{reff} - 0.258)(\frac{W}{h} + 0.8)} \tag{5.3}$$

The resonant frequency, f_0, of the antenna can now be calculated:

$$f_0 = \frac{c}{2L_{eff}\sqrt{\epsilon_{reff}}} \tag{5.4}$$

The microstrip patch antenna radiates in the direction normal to the plane of the patch. This can be seen in Figure 5.1 by taking the outer product of the magnetic and the horizontally orientated electric field.
The transmission line model is very intuitive and simple but ignores some important effects, i.e. field variations along radiating edges. The length of the radiating slot is in practice slightly longer since there are also fringing fields along the width of the patch. There are more accurate models to describe the microstrip patch antenna such as the cavity model or the Multi port Network Model (MNM). However the antenna designs described in this chapter are presented as alternatives and can be sufficiently explained with the transmission line model.

5.2 Microstrip patch antenna

A microstrip patch antenna was designed to operate at 24 GHz. The multi layered substrate stack described in Section 3.2 was used. On top of this stack was a moulding layer with $\epsilon_r = 3$. The

design is depicted in Figure 5.2. The following sizes were used: $W = 2.85$ mm, $L = 2.85$ mm, $S = 0.175$ mm, $L_s = 0.87$ mm and $W_m = 0.6$ mm.
To obtain the length of the inset L_s the parameter analysis described in reference [7] was used. The position where the feeding line attaches to the patch determines the impedance of the microstrip patch. This can be explained by looking at the field distribution depicted in Figure 5.1. The field in the middle of the patch is smaller than the field at the edge of the patch which indicates that a feeding line attaching to the center of the patch sees a lower impedance than a line attaching to the edge of the patch.

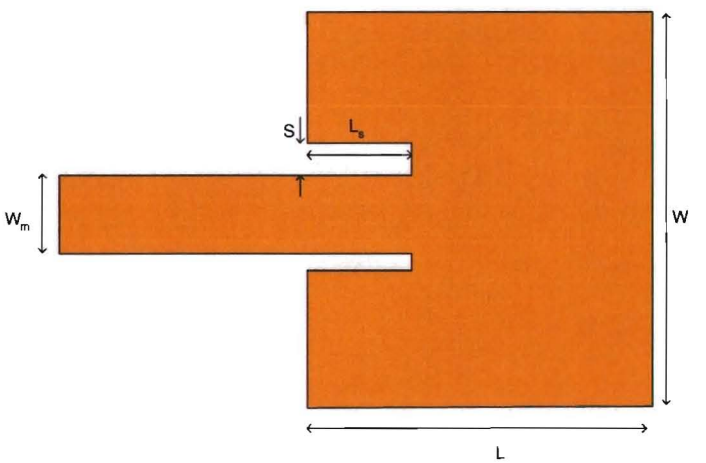

Figure 5.2: The microstrip patch antenna with feed inset, sizes: $W = 2.85$ mm, $L = 2.85$ mm, $S = 0.175$ mm, $L_s = 0.87$ mm and $W_m = 0.6$ mm

This design was simulated with ADS. The return loss plot is depicted in Figure 5.3. The return loss bandwidth is 1.23 GHz which is 5.125% of the operating frequency. The gain and directivity are summarized in Table 5.1.
One of the biggest drawbacks of the MSA design is the small bandwidth due to the small electrical size. Several methods are described in literature to increase the return loss bandwidth of the microstrip patch antenna. One way of increasing the bandwidth is by using a different substrate stack with a lower permittivity and/or a larger height, see reference [6]. This option was however not available since the substrate choice was already made. In addition the use of a thick substrate causes surface wave excitation which degrades the performance of the antenna.
An other possibility is the use of parasitically coupled elements. This configuration produces a double-tuned resonance. These elements can be rectangular patches with a different size than the main patch. These extra patches can be positioned in the same plane as the main patch or in the plane above or below the main patch. Because of the increase in size of the antenna in the horizontal plane the first option was not investigated.
The doubled tune resonance can also be obtained by feeding the rectangular patch via a slot in the metal ground plane. In this configuration a microstrip line is located on one side of the ground plane and the resonating patch is located on the other side of the patch. The length of the slot in the ground plane is a length which corresponds to a resonance close to the resonance of the patch. Several attempts have been made to obtain a large bandwidth with this antenna type. However none of the attempts obtained a bandwidth larger than 1.23 GHz. One possible explanation could be the thin spacing between the resonating patch and the ground plane.

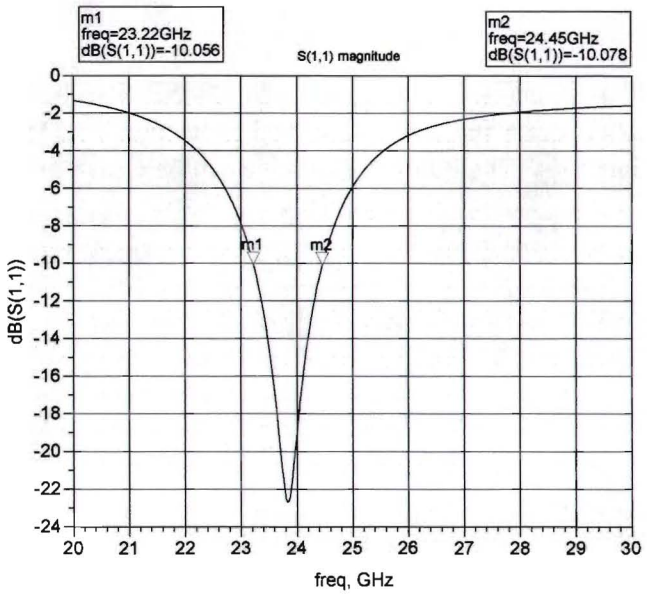

Figure 5.3: The S11 return loss plot of the MSA with sizes: $W = 2.85$ mm, $L = 2.85$ mm, $S = 0.175$ mm, $L_s = 0.87$ mm and $W_m = 0.6$ mm

5.3 Double stacked rectangular patch

The configuration of the double stacked microstrip patch antenna (SMSA) is depicted in Figure 5.4. It is a variation of the MSA described in the previous Section. A second patch with a width W_2 is placed below the upper patch with width $W_1 > W_2$. The second patch is coupled parasitically to the upper driving patch. Because of the smaller width of the lower patch the resonance frequency of this patch will be higher than the resonance frequency of the upper patch. In this way a double resonance is obtained and the bandwidth is increased.

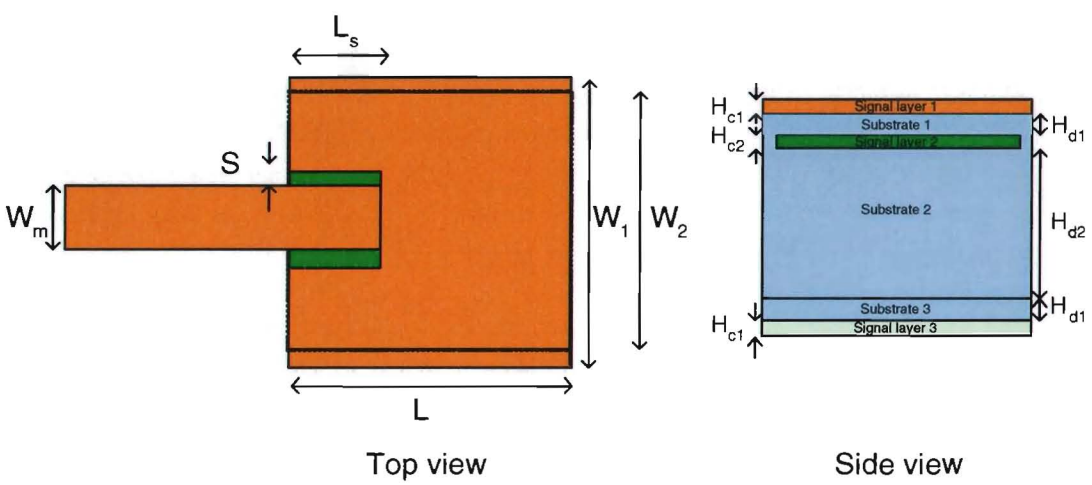

Figure 5.4: The microstrip stacked patch antenna with feed inset:$W_1 = 2.8$ mm, $W_2 = 2.53$ mm, $L = 2.88$ mm, $S = 0.173$ mm, $L_s = 0.95$ mm and $W_m = 600\mu m$, for the side view: $H_{d1} = 40\mu m$, $H_{d2} = 250\mu m$, $H_{c1} = 25\mu m$ and $H_{c2} = 28\mu m$

A design guide, see reference [8] was used to find a design on the available substrate. The dimensions of the configuration in Figure 5.4 are: $W_1 = 2.8$ mm, $W_2 = 2.53$ mm, $L = 2.88$ mm, $S = 0.173$ mm, $L_s = 0.95$ mm and $W_m = 600\mu m$. The SMSA was also covered with a moulding layer with $\epsilon_r = 3$. The substrate stack was described in Section 3.2. The plot of the return loss curve is depicted in Figure 5.5. The double resonance can be clearly seen. The upper patch res-

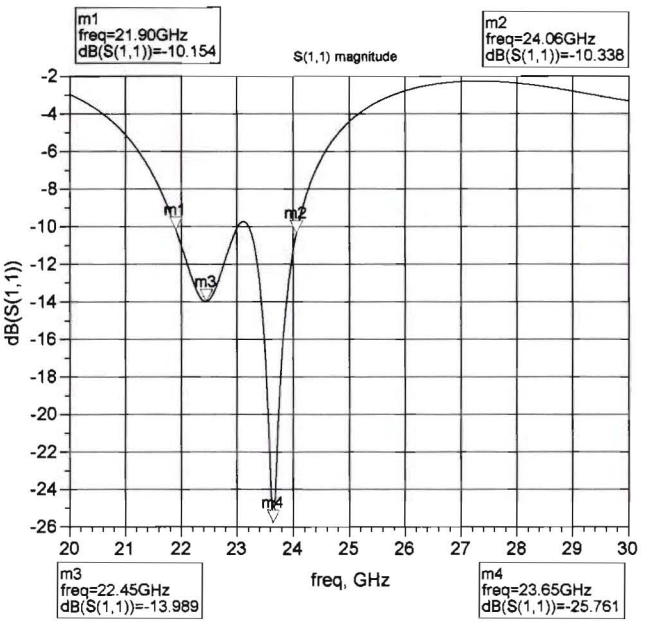

Figure 5.5: The S11 return loss plot of the SMSA with sizes: $W_1 = 2.8$ mm, $W_2 = 2.53$ mm, $L = 2.88$ mm, $S = 0.173$ mm, $L_s = 0.95$ mm and $W_m = 600\mu m$.

onates at 22.45 GHz and the lower patch resonates at 23.65 GHz. By choosing the widths of the patches almost equal the two resonances can be combined. In this way a bandwidth of 2.16 GHz has been obtained which is equal to 9% of the operating frequency. The possibility of adding an extra patch on signal layer three has not been investigated. Placing the lower patch at signal layer three has been investigated. However since the separation between the lower patch and the ground plane is only $40\mu m$ the bandwidth of the upper resonance is very small. It is expected that adding a third resonance will not produce a bandwidth of 5 GHz. The gain and directivity are summarized in Table 5.1.

5.4 Rectangular microstrip patch with a U-shaped slot

The last design that has been investigated was a rectangular slot, without inset, in which an U-shaped slot was cut out, see Figure 5.6. This design was originally proposed by Huynh in reference [9]. The slot provides another resonating frequency. The sizes of this configuration are $W = 4.685$ mm, $L = 2.797$ mm, $L_s = 1.40$ mm, $H_{in} = 0.68$ mm, $H_{out} = 1.10$ mm and $W_s = 0.21$ mm. The substrate stack was described in Section 3.2, again the moulding layer was placed over the antenna.
The bandwidth of this antenna is 5.24 GHz, which is 21.8 % of the operating frequency. As can be seen in Figure 5.7 the bandwidth is not centered around 24 GHz. The two resonances are located at 20.58 GHz and at 23.96 GHz. The total mean length of the slot is 2.20 mm. The upper

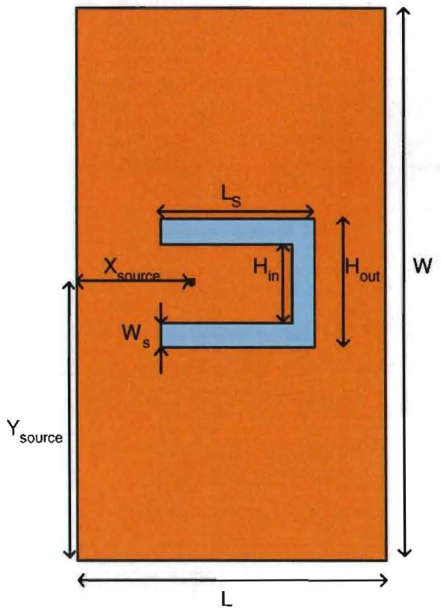

Figure 5.6: The microstrip patch antenna with an U-shaped slot, $W = 4.685$ mm, $L = 2.797$ mm, $L_s = 1.40$ mm, $H_{in} = 0.68$ mm, $H_{out} = 1.10$ mm, $W_s = 0.21$ mm, $X_{source} = 1.15$ mm and $Y_{source} = 2.34$ mm.

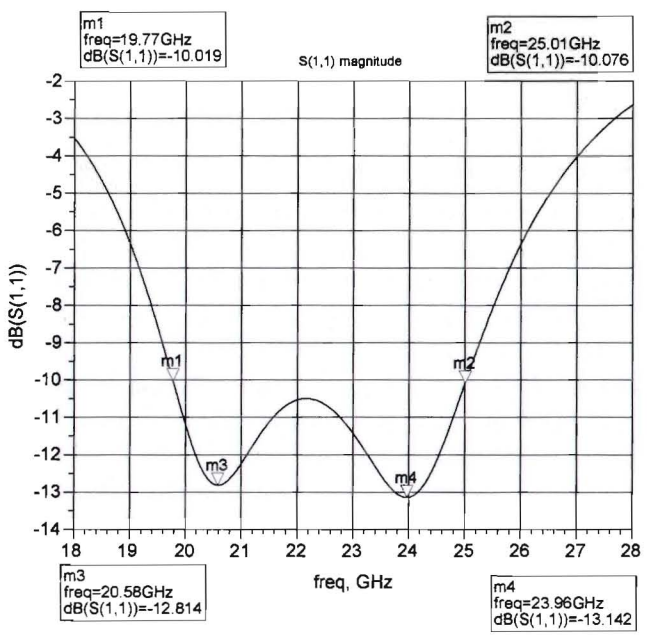

Figure 5.7: The S11 return loss plot of the MSA with an U-shaped slot: $W = 4.685$ mm, $L = 2.797$ mm, $L_s = 1.40$ mm, $H_{in} = 0.68$ mm, $H_{out} = 1.10$ mm, $W_s = 0.21$ mm, $X_{source} = 1.15$ mm and $Y_{source} = 2.34$ mm.

resonance is controlled by the slot length and the lower resonance is controlled by the width W. Several attempts have been made to connect the antenna to a feeding line, i.e. a microstrip

line coupled to the edge of the patch or a microstrip line coupled trough a slot. However all of these feeding structures severely degrade the performance of the antenna. The simulations were obtained by placing a measuring port directly on the antenna. The position of this probe was $X_{source} = 1.15$ mm and $Y_{source} = 2.34$ mm. Since no suitable connection to a feeding circuit was available the investigation of this design was abandoned.

5.5 Summary

In this chapter the principles of operation of the microstrip patch antenna have been treated. These principles were explained using the transmission line model, which provides an approximation of the resonant frequency of the MSA. Thereafter the microstrip patch antenna design was presented. The results of this antenna were also presented. It was concluded that the bandwidth of the MSA was too small. A possible solution to this problem was investigated. This solution uses a multi-resonator approach. Two variations of the MSA that use this principle were investigated. One of the presented designs, the double stacked MSA, did not meet the bandwidth requirement. The MSA with an U-shaped slot met the bandwidth requirement of 5 GHz. However no suitable feeding structure was found for this design. The results of the presented designs are summarized in Table 5.1. An error occurs when determining the efficiency in ADS. The calculation of the gain and directivity for these antennas results in equal values for the gain and directivity. This is not expected for a real antenna. Because the gain is equal to the directivity the efficiency is found to be 100 %. This problem has to be investigated further. It can be concluded

Design	Feed	Bandwidth	l Frequency	u Frequency	Gain	Directivity	Efficiency
MSA	Microstrip	1.23 GHz	23.22 GHz	24.45 GHz	6.76 dB	6.70	100 %
Stacked MSA	Microstrip	2.16 GHz	22.45 GHz	23.65 GHz	7.01 dB	6.92	100 %
U-slot MSA	Probe	5.24 GHz	20.58 GHz	23.96 GHz	6.70 dB	6.70	100 %

Table 5.1: The antenna characteristic of the microstrip patch antenna and variations thereof.

that no suitable design using a microstrip patch antenna has been found. Two variations were tested which use an extra patch or a slot in the patch. However these designs did not meet the bandwidth requirement or did not have a suitable connection. The small bandwidth can mainly be attributed to the used substrate technology. The substrate stack with a relative permittivity of 4 in combination with the thin dielectric substrate of 330 μm cannot produce a large bandwidth when the microstrip patch antennas are used.

Chapter 6

Ultra wideband antenna designs

Prior to this project a literature search concerning antenna design has been performed. The aim of this search was to find antenna designs that exhibit wideband behavior. The search resulted in a list of publications concerning antenna designs that have a wide bandwidth. Based on the results reported in these publications a pre-selection was made. Further requirements for the design were the complexity of the antenna structure, the size of the antenna and the used substrate technology. Based on these requirements designs containing a spiral or a thick foam based substrate were rejected. The designs that were selected from the pre-selection were: the stacked rectangular patch antenna, the aperture coupled rectangular patch antenna, the rectangular U-slot antenna, the tapered slot antenna and the bow-tie slot antenna. In all cases the substrate technology as described in literature was very different from the substrate technology that had to be used in this project and is described in Section 3.2. Therefore no precise conclusions could be drawn on the performance of these antenna types on the available substrate technology. Because a computer aided design program, ADS, was available fast implementation and simulation of the antenna design was possible. During the literature search publications containing design guidelines had been found. These guidelines were used to convert and to adapt the design to the new substrate technology. After optimizing the designs a comparison between the performance of the antenna designs could be made. A Table with the advantages and drawbacks of each design is presented in Table 6.1. The advantages and drawbacks are based on simulated results that

Design	Advantage	Drawback
Tapered Slot	wideband,	Low gain/ large dimensions of single element
Bow-tie Slot	wideband	Low gain/ large dimensions of single element
Stacked Patch	small structure	small bandwidth
U-Slot Patch	wideband small structure	difficult feeding structure
Aperture coupled patch	small structure	small bandwidth

Table 6.1: The advantages and drawbacks of different types of antenna designs.

will be presented later. Based on this comparison the tapered slot antenna and the bow-tie slot antenna were selected for further development and fabrication. In this chapter these designs will be treated in detail. The designs that have been rejected were treated in Chapter 5.

6.1 The tapered slot antenna

In this chapter the tapered slot antenna will be treated. The tapered slot antenna is an end-fire antenna with a large bandwidth. The design consists of a tapered slot etched on a thin film of metal which can be based on a thin substrate on one side of the film. The slot is narrow towards one end for efficient coupling. Moving away from this end the slot is tapered and a travelling wave radiates in the end-fire direction. It can be said that the tapered slot antenna is the printed circuit equivalent of the horn antenna. Where the waveguide structure of the horn antenna is represented by the tapered slot. Different types of tapering profiles have been presented during the years. Gibson introduced an exponentially tapered slot, called the Vivaldi antenna, see reference [10], this antenna had a reported bandwidth of 32 GHz. Later the linearly tapered slot antenna, LTSA, was introduced by Prasad, see reference [11]. A constant width tapered slot antenna, CWSA, was introduced by Yngvesson, see reference [12]. Simons introduced a V-shaped linear tapered slot antenna, V-LTSA, see reference [13]. More variations on these designs have been reported in literature however have not been included here. In this project the choice

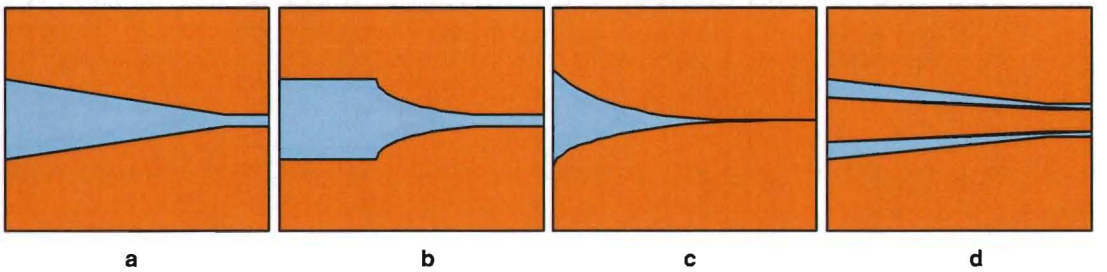

Figure 6.1: Top side view of tapered slot antenna designs: linearly tapered slot antenna (a), constant width tapered slot antenna (b), exponentially tapered slot (c), V shaped linear tapered slot antenna (d).

was made to use the V-LTSA based on the simple connection with a coplanar waveguide and the well documented design of this antenna. In the remainder of this report the V-LTSA is referred to as TSA. In this section the principles of operation of the tapered slot antenna are treated and the simulated results are presented. The design that was used as a starting point was provided by Philips Research. The modifications that have been made to this design will be treated. The results for the tapered slot antenna will be presented in the last Section.

6.1.1 Principles of operation

The tapered slot antenna is a member of the travelling wave structures of the "surface wave type". In this type of travelling wave structure the phase velocity is smaller than the speed of light, $V_{ph} \leq c$, where the phase velocity is given by:

$$V_{ph} = \frac{\omega}{\beta} \tag{6.1}$$

with β the phase constant and $\omega = 2\pi f$. The planar transmission lines described in Chapter 4 apply to this condition. The tapered slot antenna can be seen as a flared slot or a flared coplanar waveguide, in the case of the V-LTSA. In these structures the electromagnetic waves are guided down the antenna. At the base of the antenna, where the width of the slot G is small compared

to the wavelength λ_0 the waves are tightly bound. As the width of the slot increases the bonding becomes weaker and the waves are radiated away from the antenna, thus producing end-fire radiation. The width of the slot changes along the length of the antenna. As a consequence each part of the antenna radiates at a different frequency. An infinitely long TSA can thus be seen as a frequency independent antenna. Because of the flaring the phase constant, and thus the phase velocity, is dependent on the structure of the transmission line and is in this case not constant along the antenna as was described in Chapter 4. Energy is lost along the slot due to radiation perpendicular to the slot and losses in the conductors and the dielectric substrate. The radiation losses, in contrast to the transmission lines where these losses are neglected, are the main losses in the TSA.

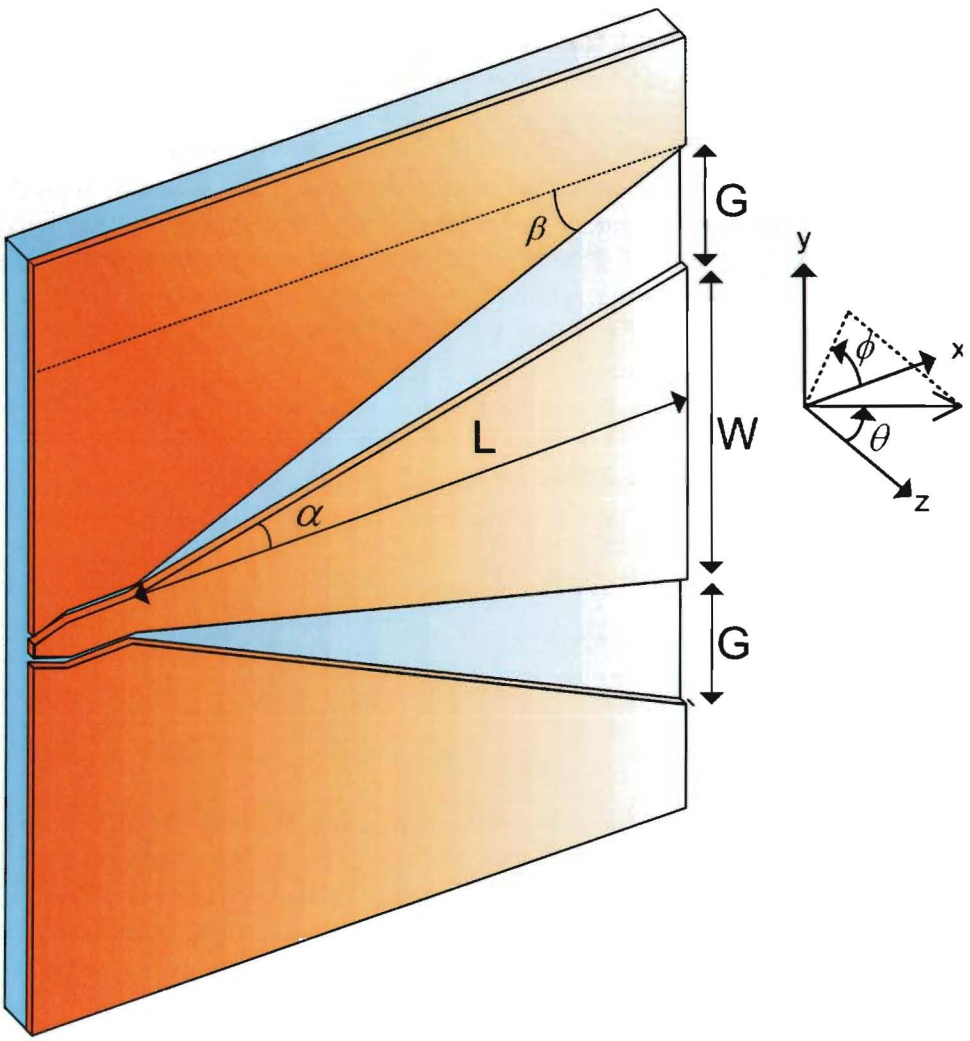

Figure 6.2: Three dimensional image of the V-LTSA. The corresponding coordinate system is depicted as well.

Several methods of analysis of the tapered slot antenna have been reported. Most of the methods approximate the behavior of the antenna by dividing the slot in N sections. To each section a uniform width is assigned and then analyzed. Different methods of analysis have been applied, i.e. coupled transmission lines or full wave analysis. Thereafter the sections are recombined and

the antenna characteristics are computed. This approach has been applied by Janaswamy in reference [14]. The first step in this approach is to find the tangential component of the electrical field in one section of the slot. These slots are then connected end to end. The power flowing out of one section is taken as the input power of the next section. The backward travelling wave arising from the discontinuities of the section junctions has not been taken into account in this approach. The electric field is obtained by using the Galerkin method in the spectral domain. The field distribution is then used to find the radiated field. This is accomplished by using the half plane Green's functions. This approach is valid for any smooth taper profile.
Wang applied a different approach to the problem in [15]. In this approach the method of moments was applied. For more information about the Method of Moments see Appendix B. Rooftop and sinusoidal basis functions where used to model the currents on the antenna structure and the Galerkin method was applied to find the interaction matrix. The method was applied to an open-ended slot line and the LTSA. Wang also applied this approach to the V-LTSA in [16].
Oraizi also applied the stepped transmission line approach to find the antenna characteristics of the TSA in [17]. In this approach the theory of coupled transmission lines as described in 4.3 is applied. Because this theory was already investigated in this project for a CPW transition in Section 4.4, an extension was made to model the designed TSA. The approach is treated in detail and applied to the V-LTSA. Although the publication presents a method to find the optimum design of a TSA this has not been attempted. Oraizi has used a LTSA for his model. In this project a V-LTSA is used. When comparing the structure of the V-LTSA to the LTSA it is obvious to use the model of a coplanar waveguide as a basis instead of the slot line.
The load impedance of the coupled transmission lines was taken to be 120π, the impedance of free space. The frequency domain is divided into K sections. Recalling from Section 4.3 that a coupled transmission line can be described as:

$$\begin{bmatrix} V_o(z) \\ I_o(z) \end{bmatrix} = T_{F,k} \begin{bmatrix} V_i(z) \\ I_i(z) \end{bmatrix} = \begin{bmatrix} A_K & B_K \\ C_K & D_K \end{bmatrix} \begin{bmatrix} V_i(z) \\ I_i(z) \end{bmatrix} \tag{6.2}$$

where $T_{F,k}$ represents the forward transmission matrix for the k^{th} frequency. The input impedance can now be given as:

$$Z_{in,k} = \frac{A_k Z_{L,k} + B_k}{C_k Z_{L,k} + D_K} \tag{6.3}$$

where $Z_{in,k}$ and $Z_{L,k}$ are the input and load impedance, respectively. To obtain the bandwidth of the antenna the input reflection coefficient is observed. The input reflection coefficient is the ratio of the magnitude of the inserted wave to the magnitude of the reflected wave on the same port. The bandwidth is defined by that part of the frequency spectrum where 10% or less of the input wave is reflected. The input reflection coefficient, or S_{11} parameter is given by:

$$S_{11}(k) = \frac{Z_{in,k} - Z_0}{Z_{in,k} + Z_0} \tag{6.4}$$

where Z_0 represents the characteristic impedance, in this case 50 Ω. The bandwidth is defined as that part of the frequency spectrum where the S_{11} curve is below -10 dB. The return loss plot is depicted in Figure 6.3. These plots have been simulated without a moulding layer covering the antenna.
From figures 6.3, 6.4 and 6.5 is clear that the used model is not accurate enough. One explanation could be the impedance with which the tapered CPW is terminated. In this model it is assumed

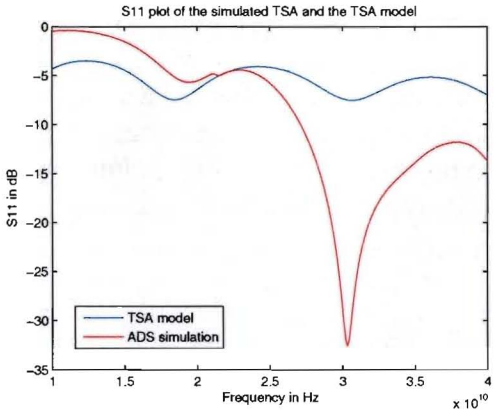

Figure 6.3: Return loss plot of the TSA model (blue) and the simulated results of ADS (red)

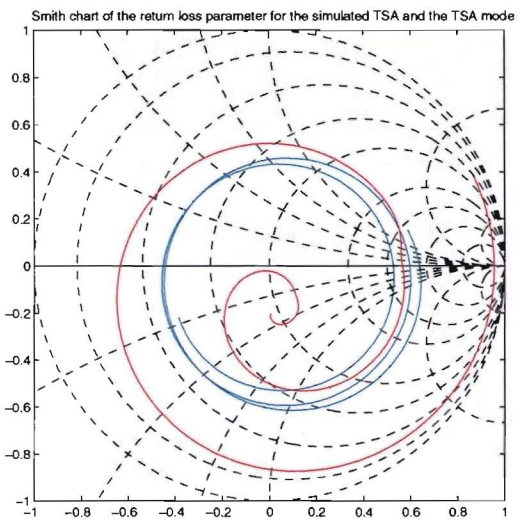

Figure 6.4: The smith chart of the TSA model (blue) and the simulated results of ADS (red)

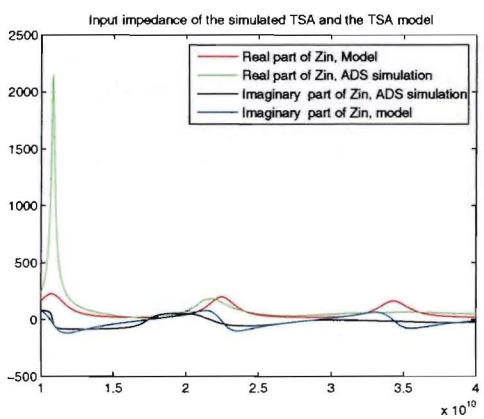

Figure 6.5: The input impedance of the TSA model and the simulated results of ADS

that the TSA is terminated with a real impedance equal to the impedance of free space. In reality there is also a capacitance due to the fringing fields at the end of the antenna. This has not been modelled and could explain the difference between the model and the simulated result. This kind of coplanar waveguide termination is not common and no models for this termination have been found in literature. The modelling of this termination is beyond the scope of this project. Therefore the Method of Moments simulator is used to design the TSA.

6.1.2 Design process

Within Philips the V-LTSA design had already been designed on a different substrate technology. This technology was modelled as follows: two perfectly conducting metal layers separated by a 635 μm thick dielectric substrate with permittivity, $\epsilon_r = 9.6$ and loss tangent $\tan\delta = 0$. This design was taken as the starting point. The TSA has two important parameters: the length of the slot L and the flaring angle, α. As a start these parameters were copied to the substrate described in Section 3.2. However no ground plane was included in the design. The V-LTSA can be directly connected to a coplanar waveguide. To achieve this, the connection of the original design had to be modified in such a way that a CPW with $W = 500\ \mu m$ and $G = 75\mu m$ could be attached. In Section 4.2 was shown that a coplanar waveguide with these dimensions has a characteristic impedance of 50 Ω. Now the feeding lines were attached the obtained design could be optimized. Therefore the design presented in reference [13] was taken as a reference. The length L and the width G in this design were chosen as 1.7 λ_0 and 0.32 λ_0. The angle α was 12.5°. As substrate a 250 μm thick substrate with $\epsilon_r = 10.5$ was used. Only the dimensions of the antenna were used from this reference. The substrate described in Section 3.2 with a moulding layer was used for the simulations.
The required bandwidth is large at 24 GHz. Therefore the focus during the design process has mostly been on requiring the maximum bandwidth. The first parameter that was varied is the angle α. The results are depicted in figures 6.6 and 6.7. Here can be seen that varying the flaring angle has a large effect on the bandwidth of the antenna. In the final design the angle was set at $\alpha = 12.4°$. As can be seen in Figure 6.6 this results in the lowest peak at 24 GHz. The advantage of this angle can also be seen in Figure 6.7, the matching of the antenna with this angle is better than the matching of the antennas with different flaring angles. The gain and directivity of the designs used in this parameter analysis are presented in Table 6.2. The designs were covered with the moulding layer.
In reference [18] measurements were presented for varying length, L, and substrate thickness, h of the Vivaldi, LTSA and CWSA. One of the conclusions was that the 3 dB beam width decreases with increasing length in addition the antenna gain also increases. Since the antenna that has to be designed is restricted in size an optimum length has to be found. Therefore the length of the V-LTSA is varied. The gain of these designs is given in Table 6.2. A strange effect occurred during the simulations. the gain is in two cases higher than the directivity. This is however not possible, the error needs to be investigated further. In Table 6.2 can be seen that the gain of the antenna increases with increasing length of the TSA. In Figure 6.8 can be seen that the length of the TSA can not be decreased below 9.08 mm. Decreasing the length further would result in an antenna that would not meet with the required bandwidth of 5 GHz. The antenna with length L = 14 mm could not be simulated with an adaptive frequency scale and therefore looks less smooth than the other lines. However the difference in behavior is still clear. In Figure 6.10 the dimensions of the final design are depicted. These dimensions were chosen based on the parameter analysis that was performed and was presented in the section above.

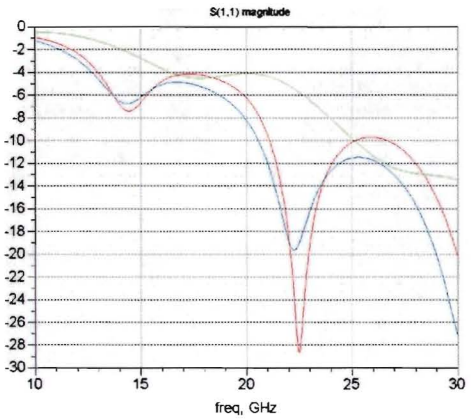

Figure 6.6: The V-LTSA for different angles α, green: $\alpha = 14.5°$, blue: $\alpha = 12.4°$ and red: $\alpha = 9.8°$

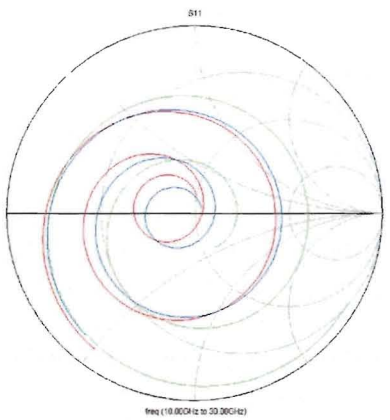

Figure 6.7: The V-LTSA for different angles α, green: $\alpha = 14.5°$, blue: $\alpha = 12.4°$ and red: $\alpha = 9.8°$'

Type	Directivity	Gain
V-LTSA $\alpha = 14.5°$ length =9.08 mm	7.3	7.5 dBi
V-LTSA $\alpha = 12.4°$ length =9.08 mm	8.5	5.2 dBi
V-LTSA $\alpha = 9.8°$ length =9.08 mm	8.5	5.5 dBi
V-LTSA $\alpha = 9.8°$ length =7 mm	7.6	4.5 dBi
V-LTSA $\alpha = 9.8°$ length = 14 mm	7.3	7.3 dBi

Table 6.2: Gain and directivity of the V-LTSA designs.

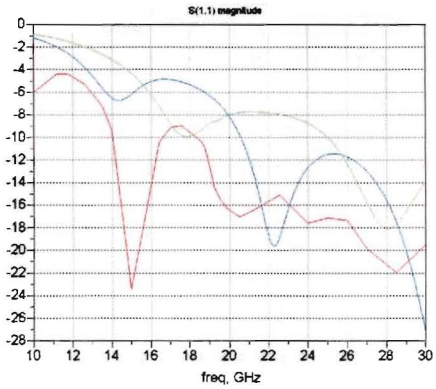

Figure 6.8: The V-LTSA for different lengths L, green: L = 7 mm, blue: L = 9.08 mm and red: L = 14 mm

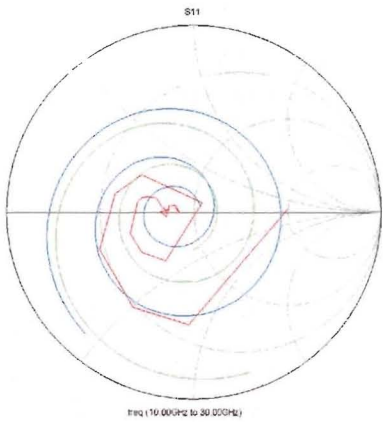

Figure 6.9: The V-LTSA for different lengths L, green: L = 7 mm, blue: L = 9.08 mm and red: L = 14 mm

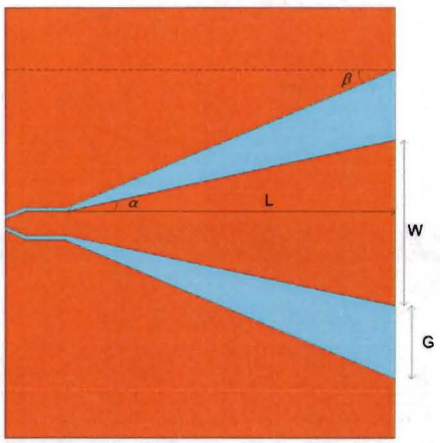

Figure 6.10: The V-LTSA and its dimensions: $L = 9.1\ mm$, $W = 4.64\ mm$, $G = 2.00\ mm$, $\alpha = 12.4°$ and $\beta = 23.00°$.

6.1.3 Simulated results of the V-LTSA

In this section the simulated results of the tapered slot antenna will be presented. The results have been obtained by simulating the tapered slot antenna in ADS Momentum. In the previous section the simulated results were obtained with a tapered slot antenna without a connector. In this section the connector has been simulated as well. However since ADS is not a full three dimensional simulator only the footprint of the connector is modelled. The results presented here do not include the shading and reflection effects that can be caused by the connector.
The S11 return loss plot is depicted in Figure 6.11. The bandwidth of the antenna is 8.12 GHz which is 33.8 % of the operating frequency. The lower frequency is located at 20.80 GHz and the upper frequency is located at 28.92 GHz. The plot shows a peak at 23.84 GHz. This can be attributed to the connector since it is not visible in the plot without a connector. The Smith chart is depicted in Figure 6.12 and shows that the antenna is matched to 50 Ω reasonably well.

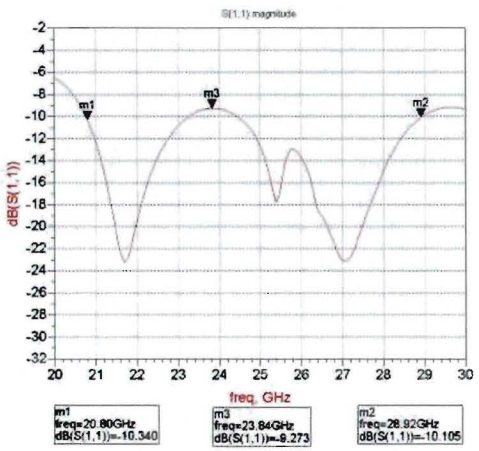

Figure 6.11: The S11 return loss plot of the V-LTSA

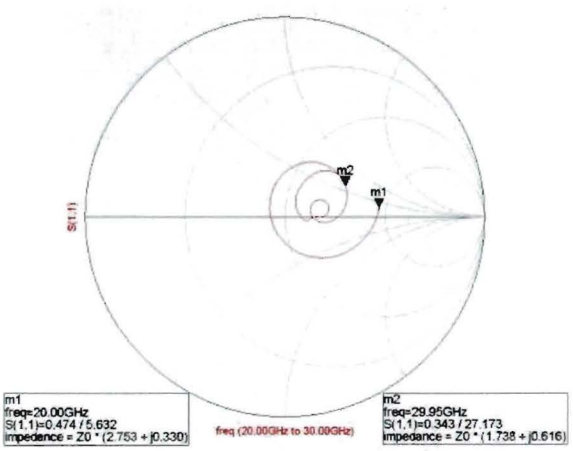

Figure 6.12: The Smith chart of the V-LTSA

The three dimensional radiation pattern of the combined co- and cross polar electric fields is presented below. The normalized intensity is represented by the color, where red represents a large intensity and green represents a small intensity. Also depicted below is the structure of the antenna, with the connector, on which the currents are depicted.

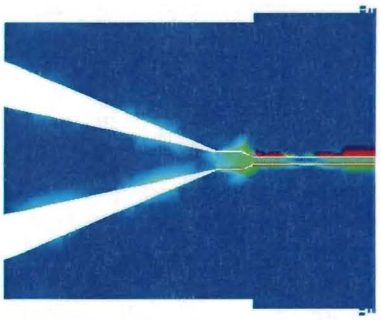

Figure 6.13: Current on the tapered slot antenna

The radiation color scheme is also used to represent the magnitude of the current. The holes

that are usually present in the connector are covered. This represents a more accurate description since the holes will usually be filled with screws. In the figure depicting the currents 6.13, can be seen that the current propagates along the edges of the slot.

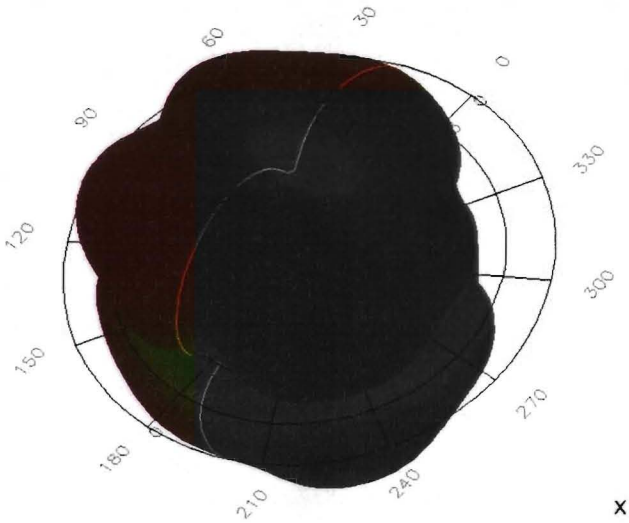

Figure 6.14: The combined co- and cross polar electrical fields of the tapered slot antenna depicted in a three dimensional plot. The depicted angle is ϕ.

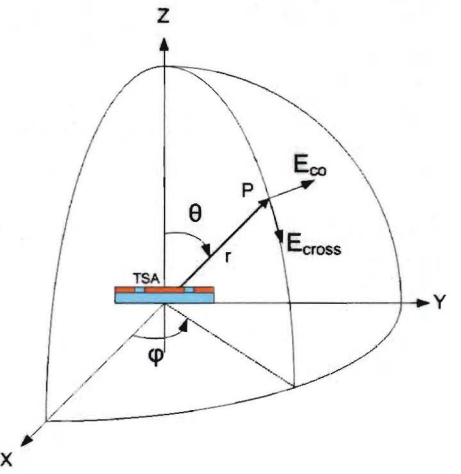

Figure 6.15: The coordination system that was used. The TSA is depicted viewed from the connector side.

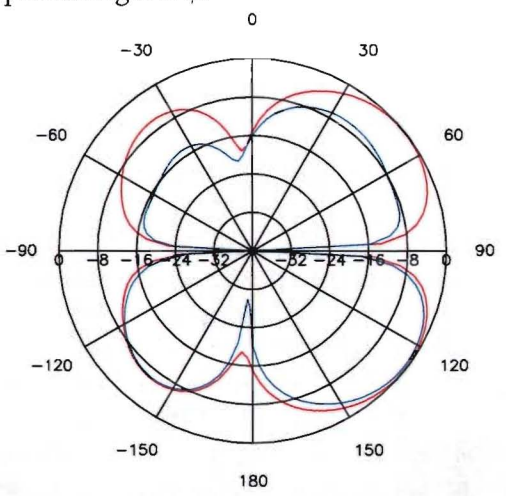

Figure 6.16: The polar plot of the tapered slot antenna with $\phi = 129°$ and the θ angle swept over 360°.

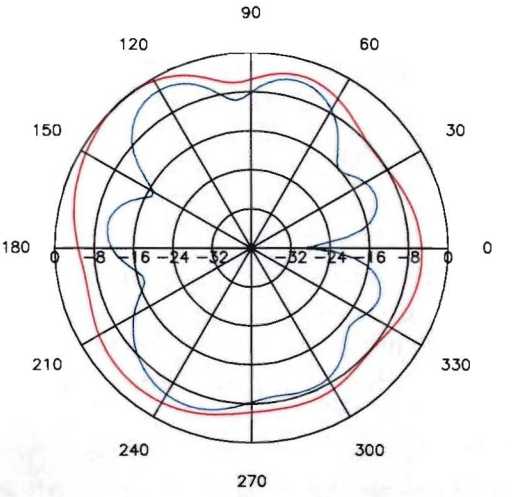

Figure 6.17: The polar plot of the tapered slot antenna with $\theta = 129°$ and the ϕ angle swept over 360°.

From the three dimensional radiation pattern, see Figure 6.14 can be seen that the antenna radiates in four directions and has a null in the XY plane. Given the two slots of the structure, see Figure 6.2 two beams are expected. The null which divides the two beams can be explained by the electric fields in the slots which are in anti-phase. The three dimensional radiation pattern has been cut. This cut has been made by setting $\phi = 129°$ and rotating θ. In red the co polar compo-

nent and the in blue the cross polar component are depicted, see Figure 6.15 for the orientation of the co- and cross polar component. The null at $\theta = 90°$ can be clearly seen. The radiation pattern has also been cut by setting $\theta = 129°$ and rotating ϕ over 360°, see Figure 6.17. The two beams at 129° and 240° can been seen. The antenna radiation characteristics at 24 GHz are given in Table 6.3. Remember that a restriction on the gain at an angle of 30° above the horizon was placed. This requirement is not met. This can be seen in Figure 6.16, at $\theta = 30°$ where the normalized gain is equal to 0 dB.
In the two figures below the gain is plotted for two different angles. For more information about the used angles see Figure 6.2. Since the radiation intensity is very low in the $\theta = 90°$ plane the θ angle was set to 129°. At this angle maximum radiation occurs. The ϕ angle is then rotated over 360°. In Figure 6.18 the gain is depicted. The two beams are clearly visible at 129° and 240°. The gains from the two beams are not equal this could be attributed to a small non symmetry in the design.

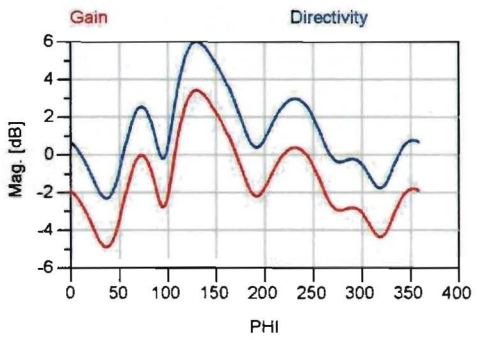

Figure 6.18: The gain and directivity plot of the TSA with the $\theta = 129°$.

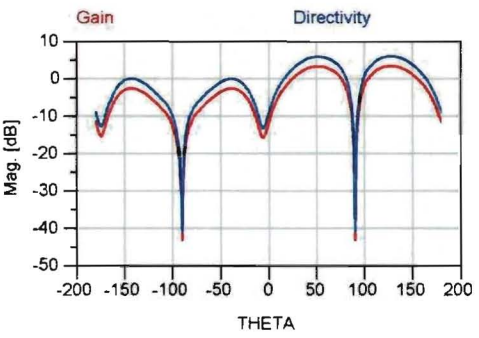

Figure 6.19: The gain and directivity plot of the TSA with the $\phi = 129°$.

Since there are regulations that restrict the amount of power that is radiated above an elevation angle of 30° it is interesting to observe the gain along the θ axis. Therefore the ϕ angle was set to the angle with maximum radiation, 129°. The gain and directivity are depicted in Figure 6.19. The small gain that was mentioned above can be clearly seen at 90°. In Figure 6.19 can also be seen that the gain is larger than zero at $\theta > 90°$ this can be explained by the absence of a ground plane.
In the applications for this design the shape of a pulse transmitted or received with this antenna is important. The shape of a pulse is distorted when different frequency components arrive at different points in time. This effect can be depicted by a plot of the group delay of an antenna. The group delay is defined as the negative derivative of the phase to frequency of the S_{11} parameter. The group delay is plotted in Figure 6.20. The average group delay was calculated by taking the average of the modulus of the group delay in the band 22 to 29 GHz. The maximum delay is determined in the same band by taking the maximum of the modulus of the group delay. The difference between the maximum delay and mean delay is important. It represents the maximum spread in time with which different frequency components are passed trough the antenna. These parameters are usually used in filter design. In most narrow band antennas this parameter is not considered important. However when using wide bandwidth designs the received signal could be distorted, the received pulse could be smeared out in time causing inter symbol interference in digital transmissions. In the table below a summarization of the antenna parameters is given.

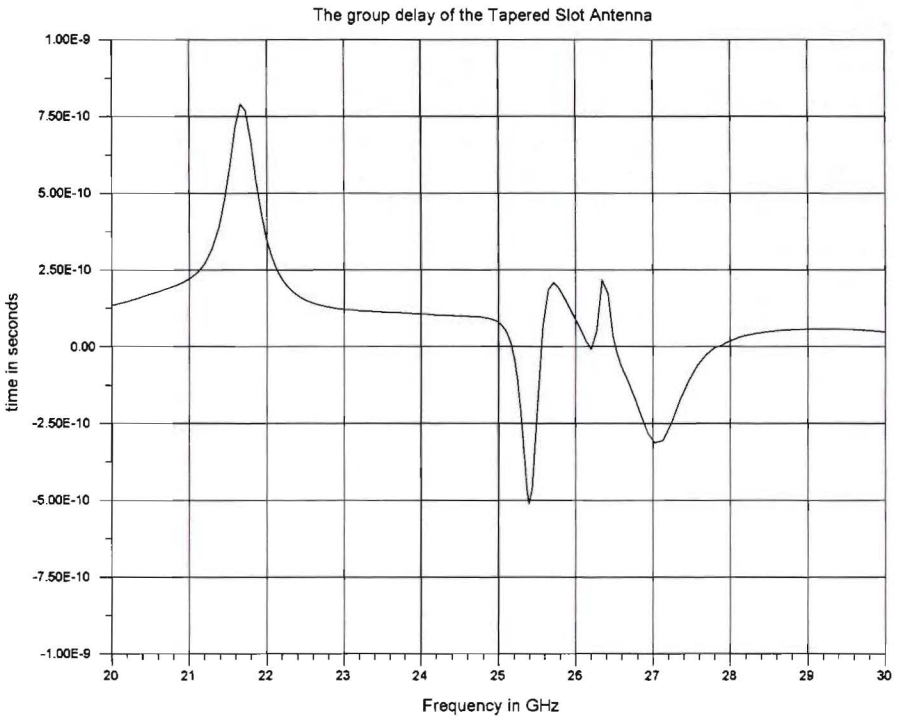

Figure 6.20: The group delay of the TSA

Parameters	value
Directivity	6.00 dBi
Gain	3.40 dBi
Angle of Maximum radiation (θ, ϕ)	129 °,129°
Efficiency	55%
Bandwidth	8.12 GHz
Lower frequency of the bandwidth	20.80 GHz
Upper frequency of the bandwidth	28.92 GHz
Average group delay	0.13 ns
Maximum group delay	-0.51 ns

Table 6.3: Antenna parameters of the tapered slot antenna with sizes: $L = 9.08$ mm and $\theta = 12.5°$.

6.2 Bow-tie slot antenna with tuning stub

The bow-tie slot antenna is the second antenna that was chosen for further investigation. The choice was made based on the large bandwidth that was demonstrated in literature. The bow-tie slot antenna consists of a thin sheet of metal in which a bow-tie shaped slot was cut out. The feeding line is based on a coplanar waveguide. To obtain more freedom in designing the antenna two metal stubs were added to the design. This design was first proposed in reference [19]. The antenna design for the 60 GHz band is depicted in Figure 6.21. The printed bow-tie antenna,

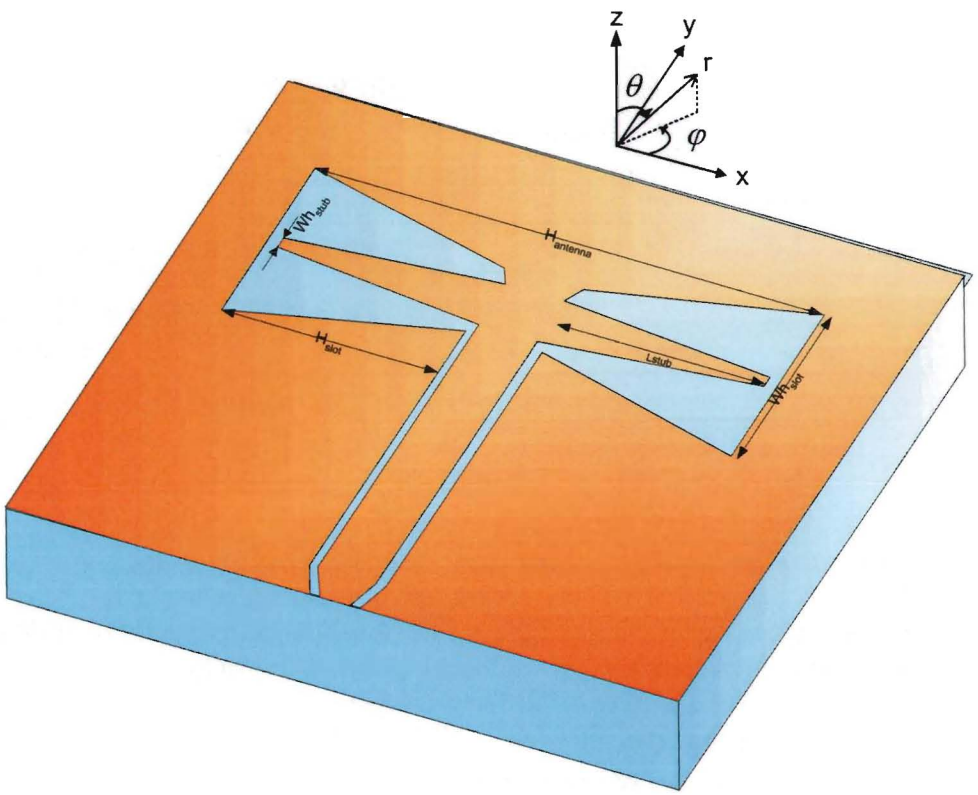

Figure 6.21: The bow-tie slot antenna for 60 GHz. The corresponding coordinate system is depicted as well.

without a metal stub, is a planar variant of the dipole antenna. The bow-tie shape of the slot increases the bandwidth. A parameter analysis of the metal stub was performed in reference [20]. The addition of the metal stub offers the designer extra freedom to tune the antenna. In addition to this freedom this type of antenna can be directly connected to a coplanar waveguide. Therefore no balun is needed.

6.2.1 Principles of operation

The bow-tie slot antenna used in this project can be seen as a bow-tie slot antenna to which a metal stub has been added. A bow-tie slot antenna without stub can be seen as a planar variant of the bi-conical horn. The bow-tie shape is chosen to increase the bandwidth. The effect of adding a metal stub can be described best with the equivalent magnetic current in the slot. The direction of the

current can be found by taking the outer product of the E field with the z-axis. The equivalent magnetic currents of a bow-tie slot antenna without a metal stub are depicted in Figure 6.23. The main resonance frequency is shifted to a lower frequency. This can be explained by the increase in path length of the magnetic current see Figure 6.22 and Figure 6.23. The electric currents are depicted in figures 6.28 and 6.38.

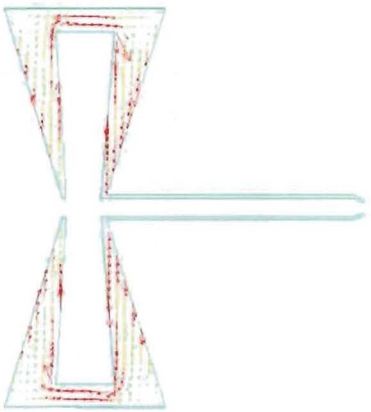

Figure 6.22: Magnetic current in the slot of the the bow-tie slot antenna with a metal stub at 24 GHz

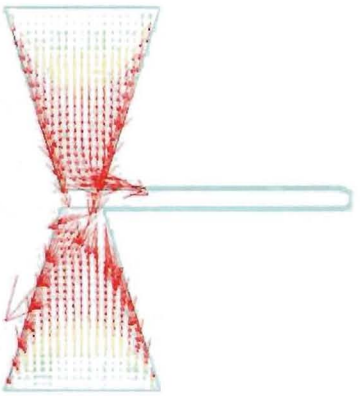

Figure 6.23: Magnetic current in the slot of the bow-tie slot antenna at 24 GHz without the metal stub

The resonances are mainly controlled by the spacing between the top of the slot and top of the metal stub $H_{spacing} = H_{slot} - L_{stub}$. Increasing this spacing wil increase the bandwidth. In addition by increasing the upper width of the metal stub Wh_{stub}, the path length can also be increased. The other dimensions have an influence on the bandwidth of the antenna as well. A parameter analysis has been performed in reference [20]. This analysis has provided enough information to design the antennas.

6.2.2 Design process

In Figure 6.24 the antenna designed for the 24 GHz short range radar band is depicted. To obtain this design the antenna proposed in reference [20] was first scaled to operate at 24 GHz. This was done by dividing all dimensions (expect the dimensions of the substrate) by the ratio of the center frequency of the short range radar to the center frequency of the original design which was 10 GHz. This ratio was taken to be $\frac{24GHz}{10GHz} = 2.4$. In reference [20] a parameter analysis of the metal stub was performed. This parameter analysis was used as a guide to find the final design. The most important parameters were the width of the metal stub Wh_{stub}, and the spacing between the top of the slot and top of the metal stub $H_{spacing} = H_{slot} - L_{stub}$. The antenna for the short range radar was designed first. The final design is depicted in Figure 6.24. Next this design was scaled linearly with $\frac{60GHz}{24GHz} = 2.5$. The dimensions of the stub where then varied until a 5 GHz bandwidth around 60 GHz was obtained. The final design is depicted in 6.25. The substrate of the bow-tie slot antennas do not have a ground plane.

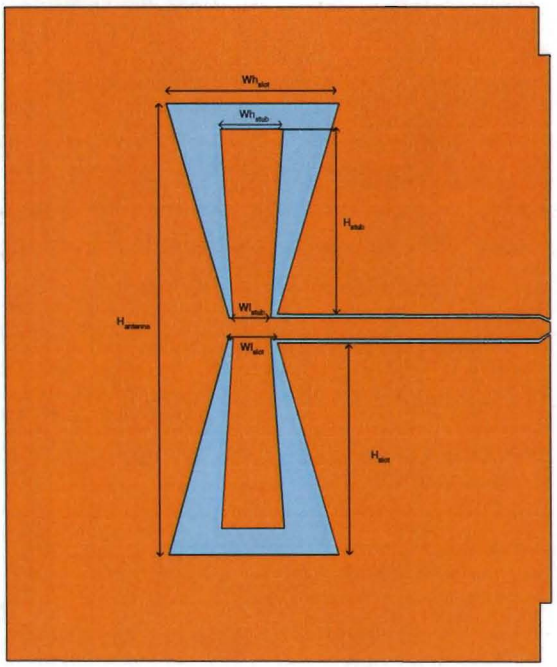

Figure 6.24: The bow-tie slot antenna for 24 GHz. Dimensions: $H_{antenna} = 10.50$ mm, $Wh_{slot} = 4.26$ mm, $Wl_{slot} = 1.20$ mm, $H_{slot} = 4.95$ mm, $Wh_{stub} = 1.55$ mm, $Wl_{stub} = 0.91$ mm and $H_{stub} = 4.30$ mm.

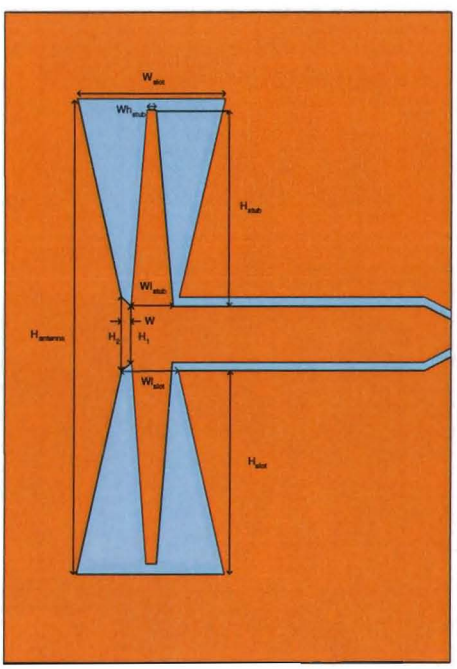

Figure 6.25: The bow-tie slot antenna for 60 GHz. Dimensions: $H_{antenna} = 4.125$ mm, $Wh_{slot} = 1.35$ mm, $Wl_{slot} = 0.52$ mm, $H_{slot} = 1.76$ mm, $Wh_{stub} = 0.88$ mm, $Wl_{stub} = 0.37$ mm, $H_{stub} = 1.75$ mm, $H_1 = 0.5$ mm, $H_2 = 0.65$ mm and $W = 0.09$ mm.

6.2.3 Simulated results at 24 GHz

In this Section the simulated results of the bow-tie antenna designed at 24 GHz are presented. The S11 return loss plot is depicted in Figure 6.26 . The bandwidth of the antenna is 14.8 GHz which is 61.6 % of the operating frequency. The lower frequency is located at 15.32 GHz and the upper frequency is located at 30.11 GHz. The bow-tie slot antenna is designed to have two main resonances. The first resonance can be found around 18 GHz the second resonance around 29 GHz is less clear. The Smith chart is depicted in Figure 6.27.

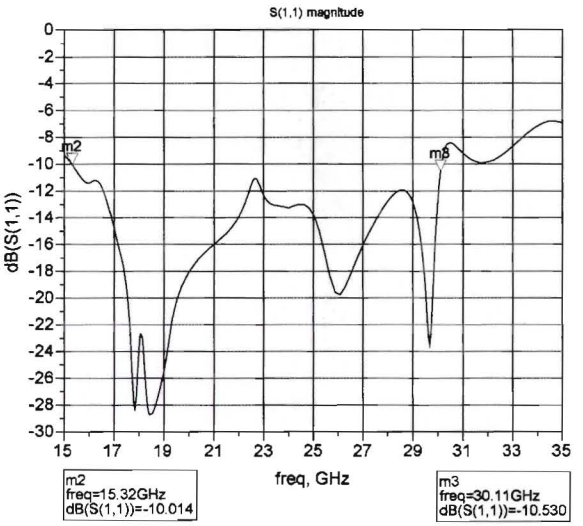

Figure 6.26: The S11 return loss plot of the bow-tie slot antenna at 24 GHz

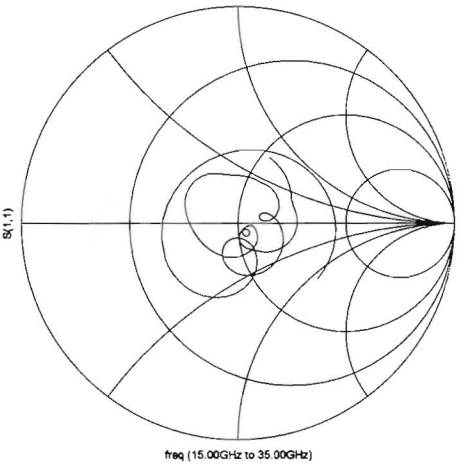

Figure 6.27: The Smith chart of the bow-tie slot antenna at 24 GHz

In the figure depicting the currents, 6.28, can be seen that the current propagates along the two metal stubs and to some extend along the direction of the coplanar waveguide.

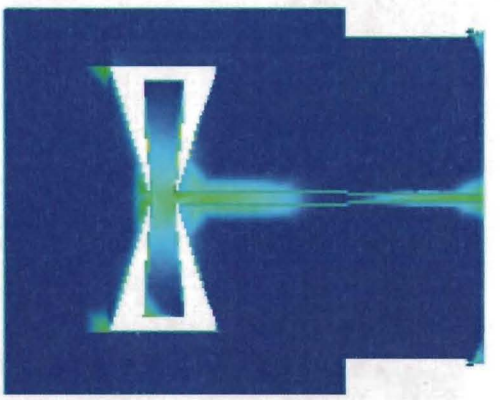

Figure 6.28: Current on the bow-tie slot antenna at 24 GHz

In the three dimensional radiation pattern, see Figure 6.29 can be seen that the antenna radiates in two directions and has a null at $\theta = 90°$.

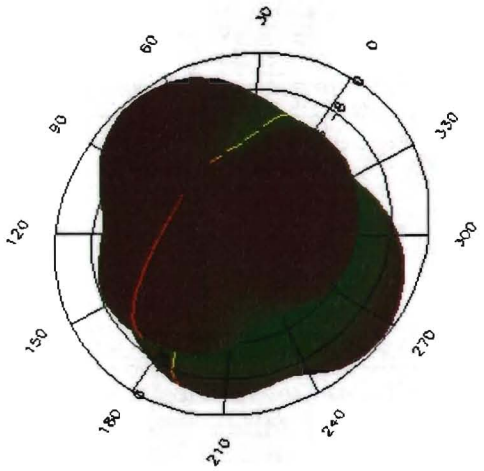

Figure 6.29: The combined co- and cross polar electrical fields of the bow-tie slot antenna at 24 GHz depicted in a three dimensional plot. The depicted angle is ϕ.

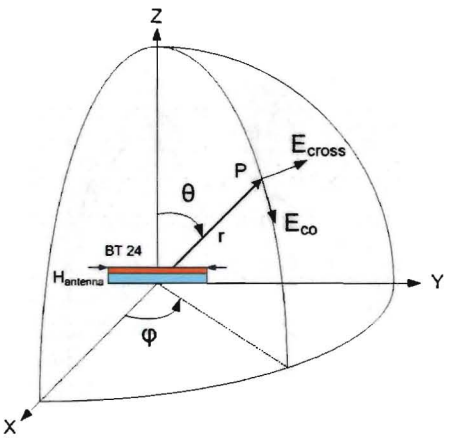

Figure 6.30: The coordination system. The bow-tie slot is depicted viewed from the front in the horizontal position

The three dimensional radiation pattern has been cut. The first cut has been made by setting $\phi = 282°$ and rotating θ see Figure 6.31. In green the co polar component and in red the cross polar component are depicted, see Figure 6.30. The radiation pattern has also been cut by setting $\theta = 150°$ and rotating ϕ, see Figure 6.32. The co polar component is depicted in blue and the cross polar component is depicted in red. The gain at an elevation angle of 30° is at most -6 dB which still exceeds the maximum gain at this angle.

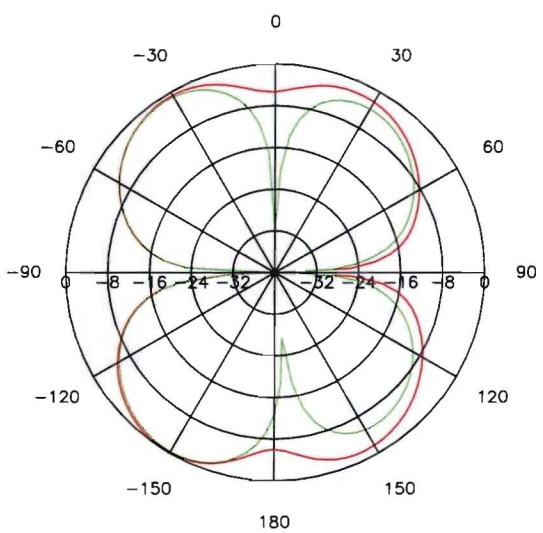

Figure 6.31: The polar plot of the bow-tie slot antenna at 24 GHz with $\phi = 282°$ and the θ angle swept over 360°.

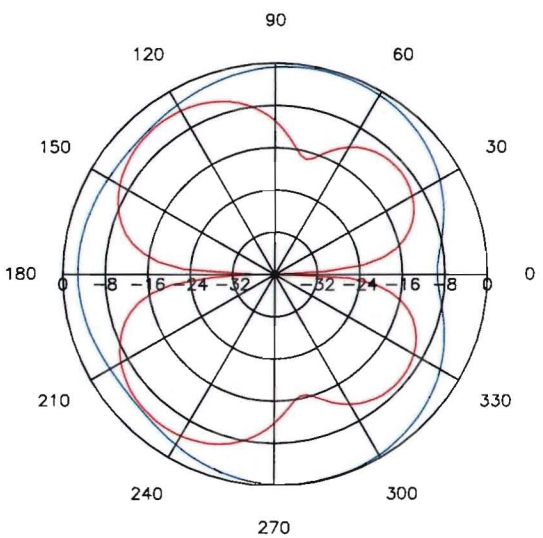

Figure 6.32: The polar plot of the bow-tie slot antenna at 24 GHz with $\theta = 150°$ and the ϕ angle swept over 360°.

The gain and directivity plots are given in figures 6.33 and 6.34. The plots are obtained by setting the θ to the angle of maximum radiation, 150° and rotating the phi angle over 360° and setting the ϕ angle to 282 ° and rotating the θ angle over 360°, respectively.

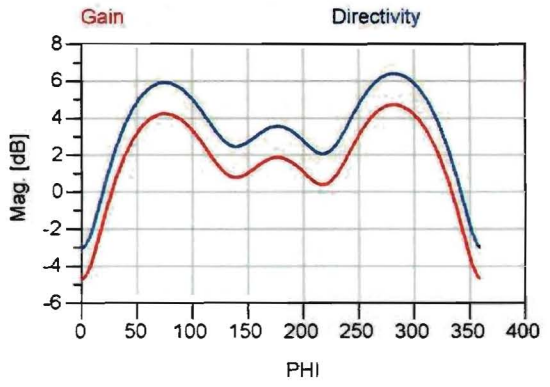

Figure 6.33: The gain and directivity plot of the bow-tie slot antenna at 24 GHz with the $\theta = 150°$.

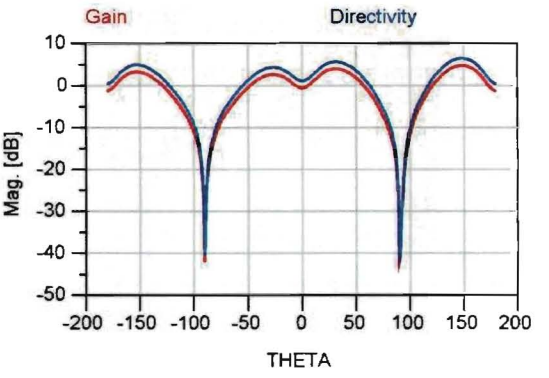

Figure 6.34: The gain and directivity plot of the bow-tie slot antenna at 24 GHz with the $\phi = 282°$.

The group delay is plotted in Figure 6.35. The average group delay was calculated by taking the average of the modulus of the group delay in the band 22 to 29 GHz. The maximum delay is determined in the same band. In Table 6.5 the simulated radiation characteristics are presented.

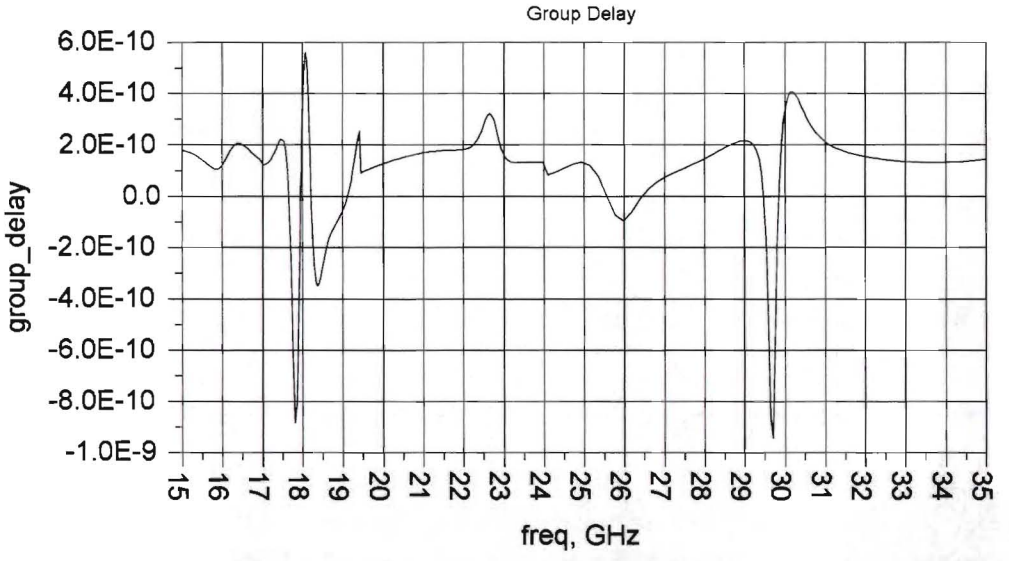

Figure 6.35: The group delay of the bow-tie slot antenna at 24 GHz

Parameters	value
Directivity	6.4 dBi
Gain	4.71 dBi
Angle of Maximum radiation (θ, ϕ)	150 °,282°
Efficiency	67.76%
Bandwidth	14.8 GHz
Lower frequency of the bandwidth	15.32 GHz
Upper frequency of the bandwidth	30.11 GHz
Average group delay	0.16 ns
Maximum group delay	0.32 ns

Table 6.4: Antenna parameters of the bow-tie slot antenna at 24 GHz with dimensions: $H_{antenna} = 10.50$ mm, $Wh_{slot} = 4.26$ mm, $Wl_{slot} = 1.20$ mm, $H_{slot} = 4.95$ mm, $Wh_{stub} = 1.55$ mm, $Wl_{stub} = 0.91$ mm and $H_{stub} = 4.30$ mm.

6.2.4 Simulated results at 60 GHz

In this Section the simulated results of the bow-tie antenna designed at 60 GHz are presented. In Table 6.5 the simulated radiation characteristics are presented. This antenna had to be simulated without the connector because the amount of memory that was available was insufficient. The S11 return loss plot is depicted in Figure 6.36. The bandwidth of the antenna is 17.21 GHz which is 28.7 % of the operating frequency. The lower frequency is located at 48.02 GHz and the upper frequency is located at 65.23 GHz. The bow-tie antenna clearly has two resonances, the first is located at 52 GHz, the second is located at 63 GHz. The Smith chart is depicted in Figure 6.37.

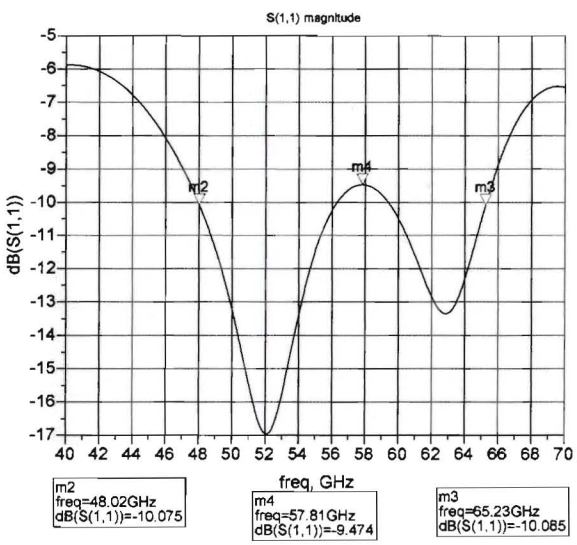

Figure 6.36: The S11 return loss plot of the bow-tie slot antenna at 60 GHz

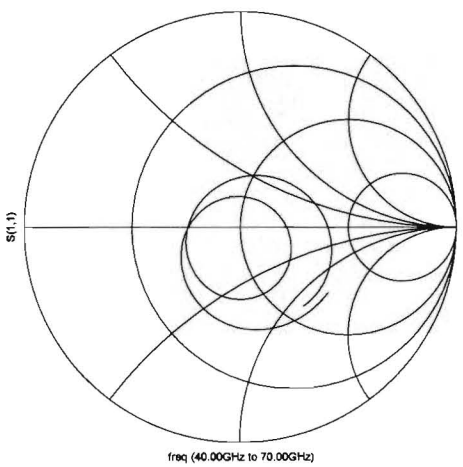

Figure 6.37: The Smith chart of the bow-tie slot antenna at 60 GHz

The three dimensional radiation pattern is depicted in Figure 6.39. In contrast to the bow-tie antenna at 24 GHz the radiation pattern does not have two clear beams in which it radiates in the XY plane. The current is depicted in Figure 6.38.

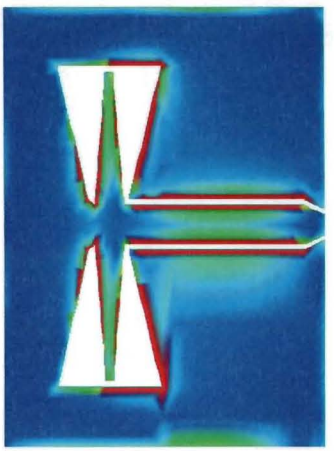

Figure 6.38: Current on the bow-tie slot antenna at 60 GHz

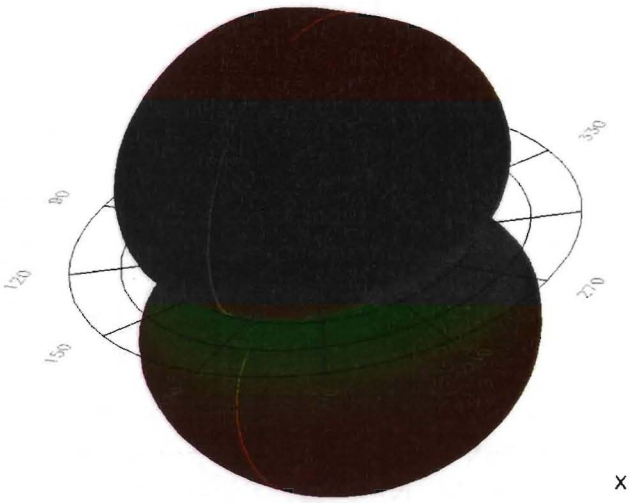

Figure 6.39: The combined co- and cross polar electrical fields of the bow-tie slot antenna at 60 GHz depicted in a three dimensional plot. The depicted angle is ϕ.

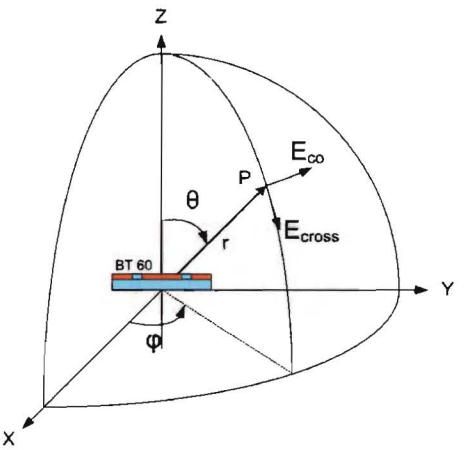

Figure 6.40: The coordination system. The bow-tie slot at 60 GHz is depicted viewed from the connector side in the horizontal position

The three dimensional radiation pattern has been cut. The first cut has been made by setting $\phi = 300°$ and rotating θ, see Figure 6.41. In red the co polar component and in blue the cross polar component are depicted, see Figure 6.40. The radiation pattern has also been cut by setting $\theta = 150°$ and rotating ϕ, see Figure 6.42. The co polar component is depicted in red and the cross polar component is depicted in blue. For the antenna operating at 60 GHz no limits were set to the gain at a specific elevation angle.

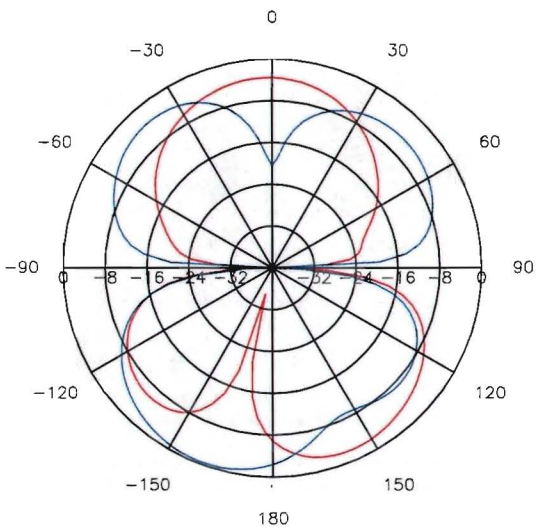

Figure 6.41: The polar plot of the bow-tie slot antenna at 60 GHz with $\phi = 300°$ and the θ angle swept over 360°.

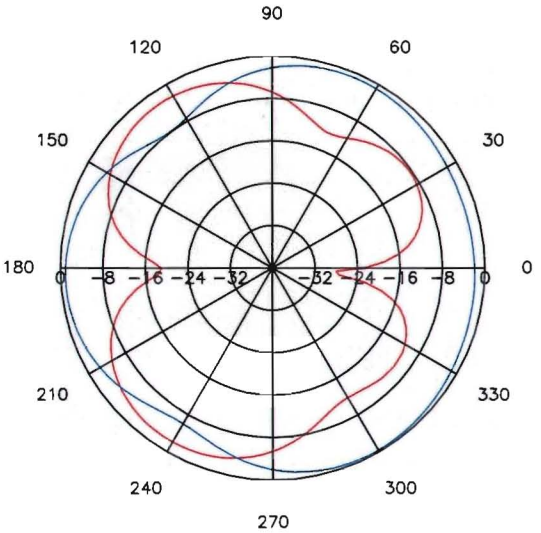

Figure 6.42: The polar plot of the bow-tie slot antenna at 60 GHz with $\theta = 150°$ and the ϕ angle swept over 360°.

The gain and directivity plots are given in figures 6.43 and 6.44. The plots are obtained by setting the θ to the angle of maximum radiation, 153° and rotating the ϕ angle over 360° and setting the ϕ angle to 293 ° and rotating the θ angle over 360° respectively.

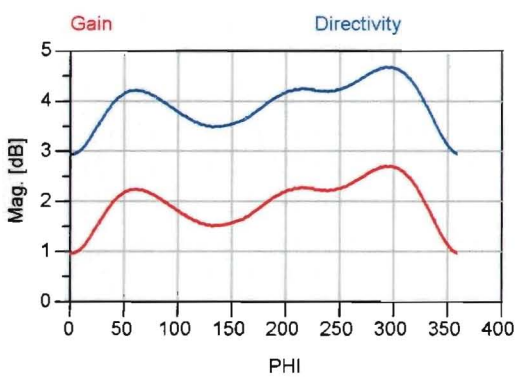

Figure 6.43: The gain and directivity plot of the bow-tie slot antenna at 60 GHz with the $\theta = 150°$.

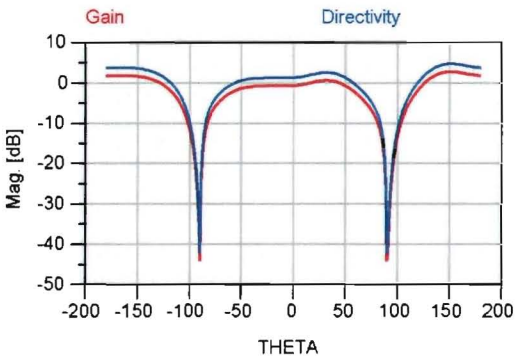

Figure 6.44: The gain and directivity plot of the bow-tie slot antenna at 60 GHz with the $\phi = 300°$.

The group delay is plotted in Figure 6.45. The average group delay was calculated by taking the average of the modulus of the group delay in the band 59 to 65 GHz. The maximum delay is determined in the same band.

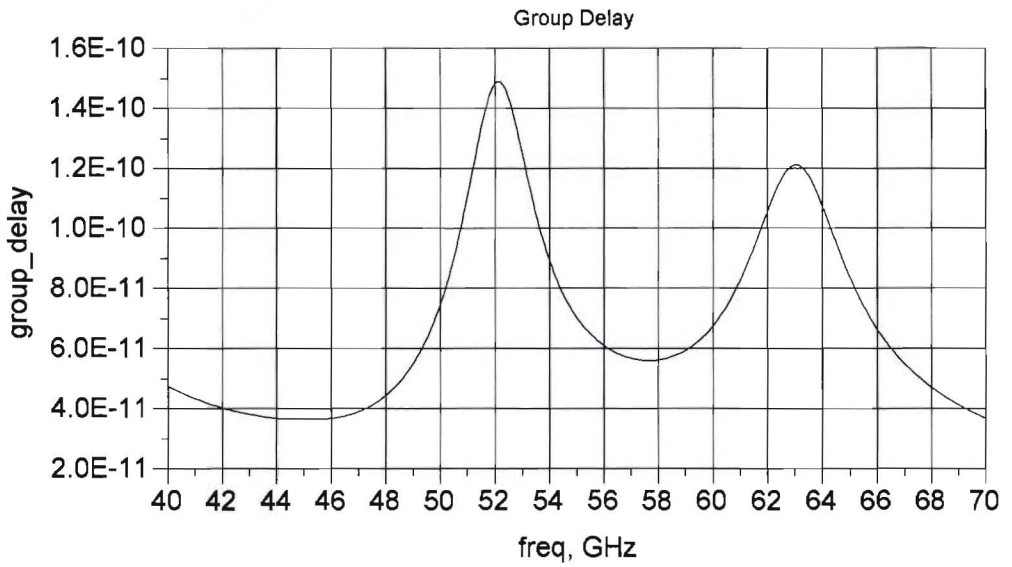

Figure 6.45: The group delay of the bow-tie slot antenna at 60 GHz

Parameters	value
Directivity	4.69 dBi
Gain	2.70 dBi
Angle of Maximum radiation (θ, ϕ)	153 °,293°
Efficiency	63.24%
Bandwidth	17.21 GHz
Lower frequency of the bandwidth	48.02 GHz
Upper frequency of the bandwidth	65.23 GHz
Average group delay	0.097 ns
Maximum group delay	0.12 ns

Table 6.5: Antenna parameters of the bow-tie slot antenna at 60 GHz with dimensions:$H_{antenna}$ = 4.125 mm, Wh_{slot} = 1.35 mm, Wl_{slot} = 0.52 mm, H_{slot} = 1.76 mm, Wh_{stub} = 0.88 mm, Wl_{stub} = 0.37 mm, H_{stub} = 1.75 mm, H_1 = 0.5 mm, H_2 = 0.65 mm and W = 0.09 mm.

Since a scaled version of the bow-tie slot antenna was used at 60 GHz the same radiation pattern was expected. However the radiation characteristics of the two bow-tie slot antennas are slightly different. The most noticeable difference was found in the radiation pattern at a fixed θ angle. In the design for 24 GHz there is only one strong component. In the design for 60 GHz there are two strong components. The strongest polarization has been determined in ADS. For the bow-tie slot antenna at 24 GHz this found to be the polarization along E_{co}, see Figure 6.30 and for the bow-tie slot antenna at 60 GHz this was found to be the polarization along E_{co} see Figure 6.40.

Chapter 7

Antenna results

The ultra wideband antennas that were presented in Chapter 6 were fabricated together with several other designs. These fabricated antennas were available for measurement. In the previous chapter results of the ultra wideband antennas were presented that were obtained with ADS Momentum from Agilent. In this chapter the results of the measurement of the fabricated antennas will be presented. Two sets of return loss bandwidth measurements were performed. In the first set the entire board, see Figure 7.14, was placed in a probe station.

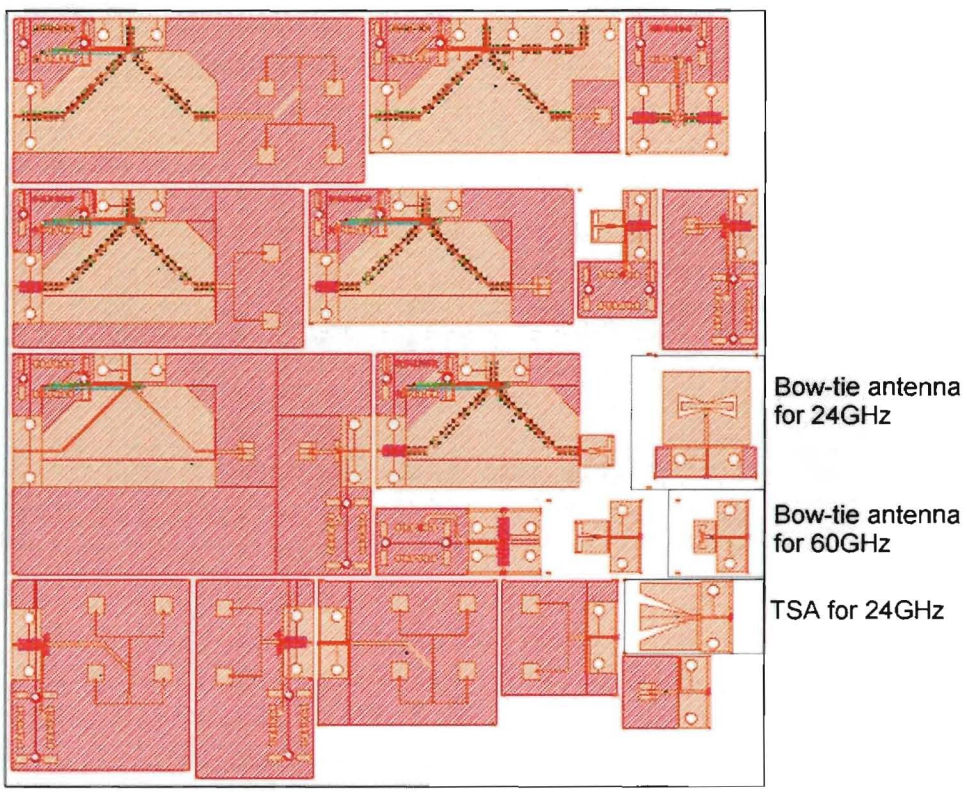

Figure 7.1: The total board with the designed antennas on the right side.

A probe was placed on a special pad that was placed on the side of the connector footprint, see Figure 4.16. The probe was connected to a vector network analyzer. In the second measurement the antennas were cut out of the board and the connector as described in Section 4.4 was connected to the antenna. The antenna was then connected to a vector network analyzer with coax cables.

In this chapter the results of the measurements will be presented starting with the probe station measurement in Section 7.1 followed by the measurement performed on the antenna with the connector in Section 7.2. Then the results from a radiation pattern measurement and an antenna gain measurement will be presented in Section 7.3. In the last Section 7.4, a summary of the measured antenna parameters is given. In addition to the results conclusions will be drawn on the performance of the antennas with regard to the requirements set in Chapter 3 and the simulations performed in ADS Momentum presented in Chapter 6.

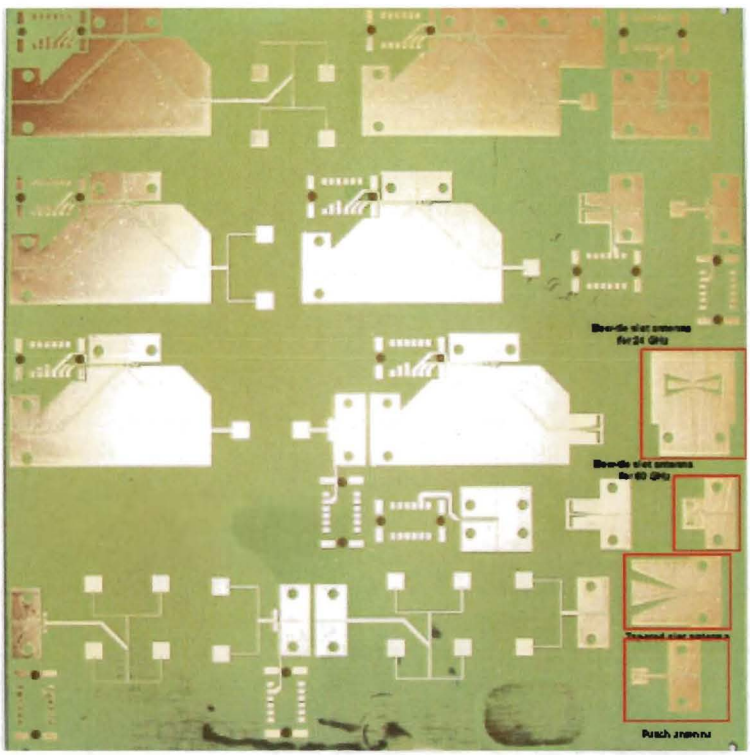

Figure 7.2: Photo of the total board with the designed antennas on the right side.

7.1 Probe station measurement

In this Section the results of the first set of measurements will be presented. In this set the board was placed inside a probe station and a probe was placed on a special pad connected to the antennas. Only one board was available for measuring. In figures 7.3 and 7.4 the S11 return loss plot and the Smith chart of the tapered slot antenna are depicted respectively. It is clear that return loss is different from the original simulation, also depicted in figures 7.3 and 7.4.

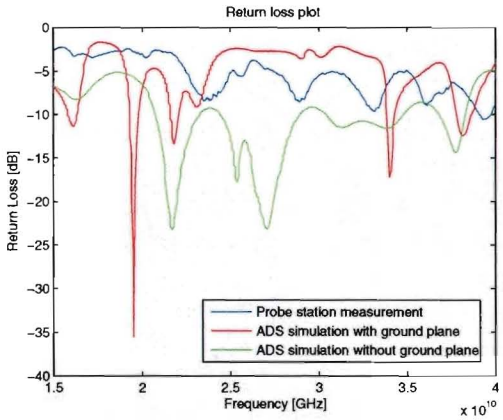

Figure 7.3: The S11 return loss plot of the tapered slot antenna measured in the probe station.

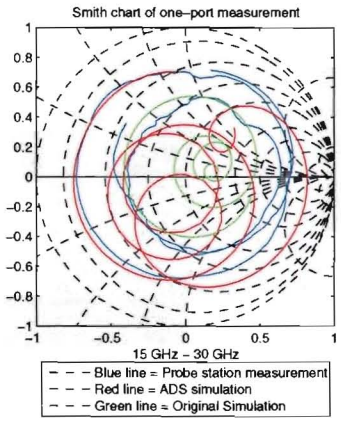

Figure 7.4: The Smith chart of the tapered slot antenna measured in the probe station. The frequency scale has been adjusted in order to depict the part with the best match.

There are several reasons for the difference in performance between the simulated and measured results. The first reason is the environment in which the measurement is performed. The board is placed on a metal plate connected to ground. In addition the board is placed in a space which is enclosed by metal. The ground plane and metal box were not simulated. To test the addition of a ground plane to the tapered slot antenna a simulation was performed in ADS. In this simulation the original design was copied and a ground plane was added to the design. The results of this simulation are also included in figures 7.3 and 7.4. In figures 7.3 and 7.4 can be seen that there is a difference between the simulation of the tapered slot antenna with the ground plane and the probe measurement of the tapered slot antenna. Therefore more factors most contribute to the difference. A possible factor could be the substrate on which the antenna is placed. In the simulation there are no other metallic structures surrounding the antenna in this case however there are several large metallic structures see Figure 7.14. The tapered slot antenna is an end-fire antenna, therefore the antenna radiates into the board surrounding the antenna. This changes the load impedance of the antenna. This effect has not been tested. It is clear that the tapered slot antenna does not meet the bandwidth requirement of 5 GHz in this situation.

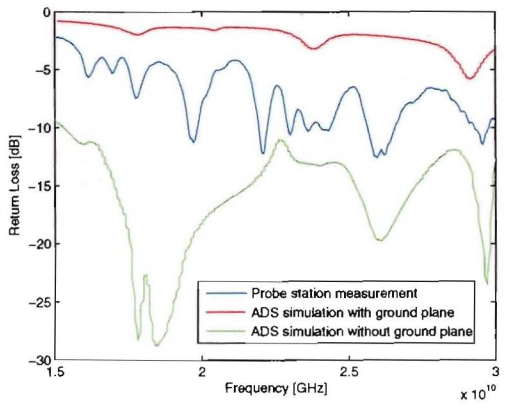

Figure 7.5: The S11 return loss plot of the bow-tie slot antenna at 24 GHz measured in the probe station.

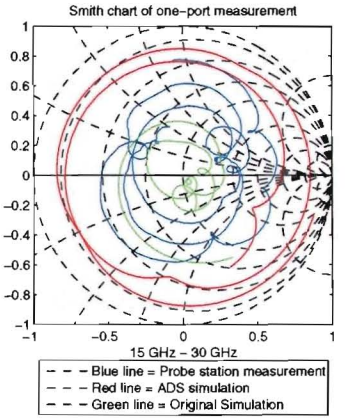

Figure 7.6: The Smith chart of the bow-tie slot antenna at 24 GHz measured in the probe station.

The second antenna that was measured is the bow-tie slot antenna designed for the 24 GHz band. The measurement procedure was similar to the measurement of the tapered slot antenna. The results are depicted in figures 7.5 and 7.6. The addition of the ground plane and the metallic structures on the substrate change the return loss bandwidth considerably. It is also clear that the bow-tie antenna at 24 GHz does not meet the bandwidth requirement of 5 GHz in this case.

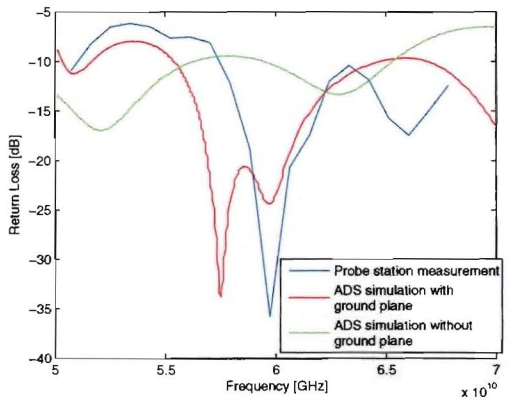

Figure 7.7: The S11 return loss plot of the bow-tie slot antenna at 60 GHz measured in the probe station.

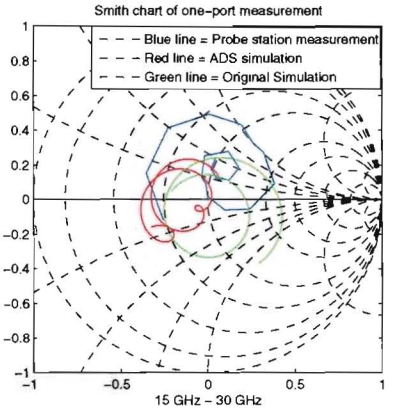

Figure 7.8: The Smith chart of the bow-tie slot antenna at 60 GHz measured in the probe station.

The last antenna that was measured is the bow-tie slot antenna designed for the 60 GHz band. The measurement procedure was similar to the measurement of the tapered slot antenna. The results are depicted in figures 7.7 and 7.8. In this case the effect of the ground plane can be clearly seen. The effects of the environment are smaller than in the other two measurements. The bandwidth requirement of 5 GHz is met in this case. The results of the bow-tie antenna at 24 GHz are dissimilar to the results of the bow-tie antenna at 60 GHz. In the former the effect of the ground plane was stronger.

7.2 Measurement results of the antenna with connector

The second set of measurements was performed on the antenna with the connector. The antennas were connected via a coax cable to a vector network analyzer. Two types of network analyzers were used, the first was able the measure signals up to 50 GHz and was used to measure the tapered slot and the bow-tie antenna at 24 GHz. The second network analyzer that was used was able to measure signals up to 67 GHz. The measurements were stored on a pc and loaded in to Matlab for further processing. The simulated results from ADS are also added to each figure for easy comparison. Three samples per antenna type were available for testing. However in some cases the connection between the connector and the coplanar waveguide of the antennas was not good. This happened in the case of the bow-tie antennas. See Section 4.4 for more information about the connector.
The first antenna that was measured was the tapered slot antenna. The S11 return loss plot and the S11 smith chart are depicted below. With this measurement there was no ground plane below the antenna. Therefore it is not necessary to depict the results of the ADS simulation with a ground plane added to the antenna designs.

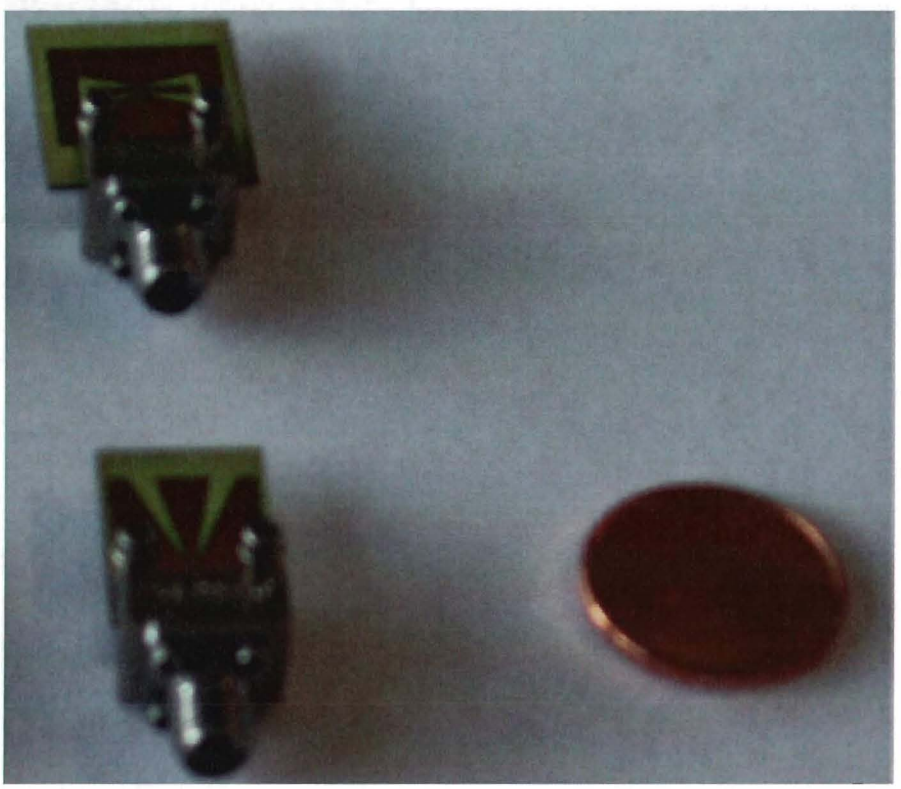

Figure 7.9: Photo of the bow-tie antenna for 24 GHz(upper) and the TSA (lower).

In Figure 7.10 can be seen that the tapered slot antenna meets the bandwidth requirement. However the lower frequency of the antenna is too high. Furthermore it is clear that there is some spread in the production process. The measured antennas outperform the simulated antennas on the width of the return loss bandwidth. In addition the measured antennas have a lower return loss.

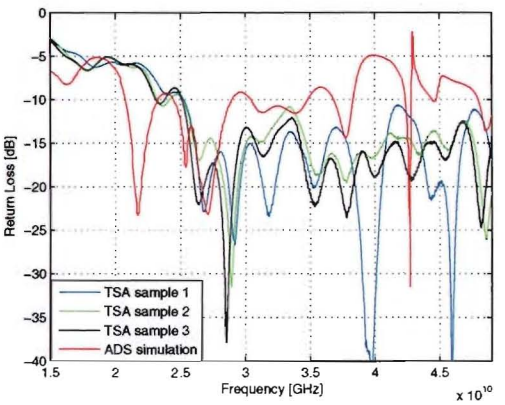

Figure 7.10: The S11 return loss plot of the tapered slot antenna at 24 GHz.

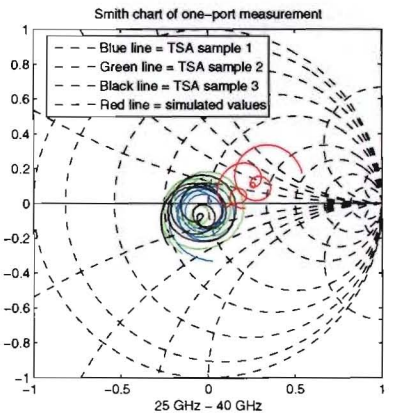

Figure 7.11: The Smith chart of the tapered slot antenna at 24 GHz.

In figures 7.12 and 7.13 the results of the bow-tie antenna at 24 GHz are depicted. The bandwidth requirement is met several times over and the return loss is lower than was predicted by the simulations in ADS.

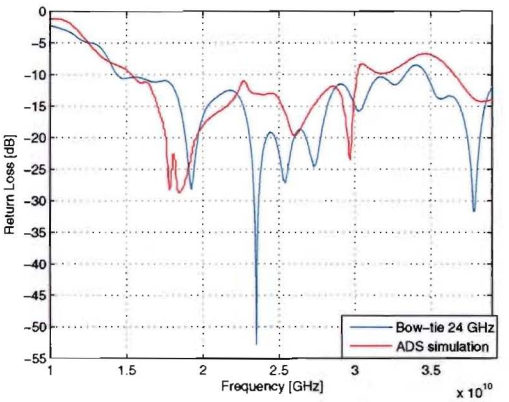

Figure 7.12: The S11 return loss plot of the bow-tie slot antenna at 24 GHz.

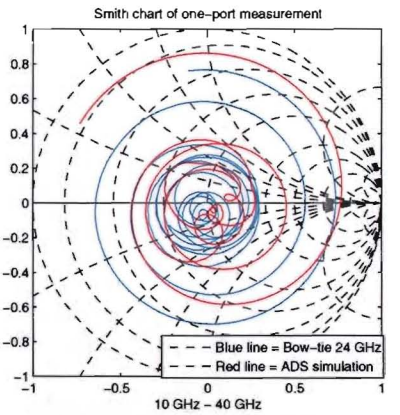

Figure 7.13: The Smith chart of the bow-tie slot antenna at 24 GHz.

In Figures 7.15 and 7.16 the results of the bow-tie antenna at 60 GHz are depicted. Also for this antenna there is only one working sample. The working example has a wide bandwidth of 20.5 GHz which is more than the simulated bandwidth. The measured return loss plot does not resemble the simulated return loss plot. In the probe station measurement the measured and simulated return loss plots showed better resemblance. The differences between the measured return loss plot depicted in Figure 7.15 and the simulated return loss plot could be explained by the resonances in the connector. The connector that was used has been certified up till 40 GHz. Another explanation could be the quality of the electronic calibration kit which has been used for the return loss measurement of the antenna with connector.

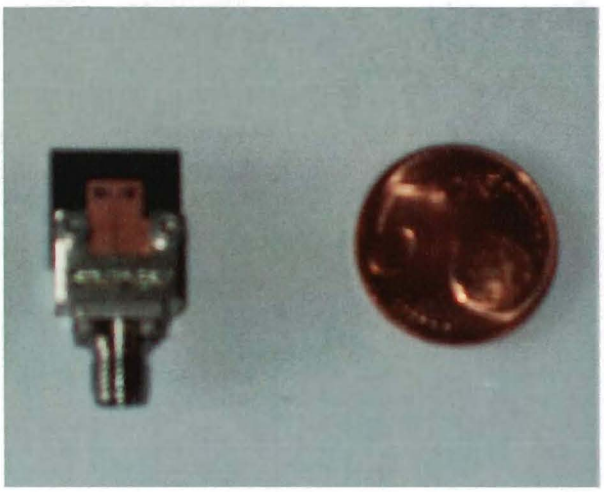

Figure 7.14: Photo of the bow-tie antenna for 60 GHz.

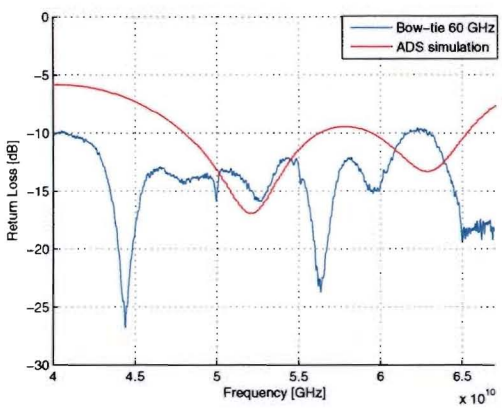

Figure 7.15: The S11 return loss plot of the bow-tie slot antenna at 60 GHz.

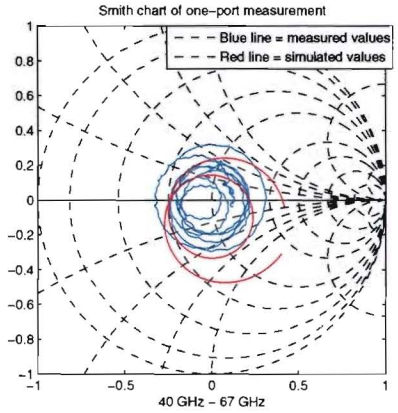

Figure 7.16: The Smith chart of the bow-tie slot antenna at 60 GHz.

Antenna type	Lower frequency	Upper frequency	Bandwidth
Tapered slot /1	25.2 GHz	>40 GHz	> 14.8 GHz
Tapered slot /2	25.1 GHz	>40 GHz	> 14.9 GHz
Tapered slot /3	25.1 GHz	>40 GHz	> 14.9 GHz
Bow-tie slot 24 /1	14.3 GHz	33.3 GHz	19 GHz
Bow-tie slot 60 /3	41.0 GHz	61.5 GHz	20.5 GHz

Table 7.1: The return loss characteristics of the measured tapered slot and bow-tie slot antennas.

In Table 7.1 the results of the return loss measurements are given. For every antenna type there was at least one working sample which met the bandwidth requirement of 5 GHz.

7.3 Antenna radiation pattern and gain measurement

Philips Research offered the possibility to use an EMC test facility to measure the radiation patterns of the antennas designed for 24 GHz. This test facility is certified only up till 18 GHz. The antennas were placed on a turntable $P_{antenna}$ in front of a horn antenna at position P_{probe}. The antennas could be placed in a vertical position or in a horizontal position see pictures D.2 and D.1 respectively. The horn antenna could be rotated 90° in order to measure the vertical $P_{vertical}$ and horizontal $P_{horizontal}$ polarization see Figure 7.17. The turntable was rotated over 360° corresponding to ϕ and for each ϕ the power delivered from the antenna under test to the horn antenna was registered. The angle resolution was 1°.

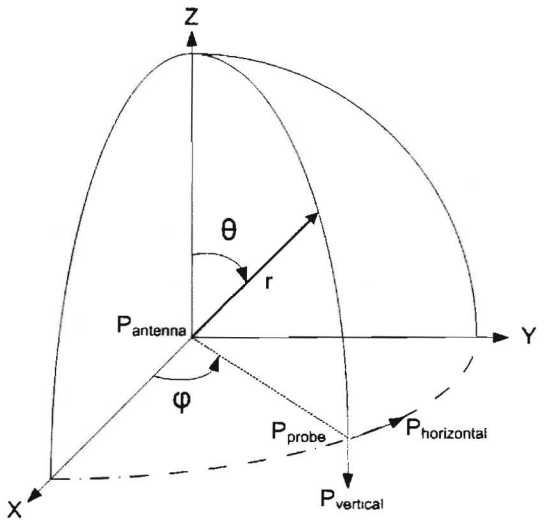

Figure 7.17: The coordination system used in the EMC measurement.

The radiation patterns of the tapered slot and bow-tie slot antenna at 24 GHz were measured. Based on the simulation that has been performed in ADS Momentum it was expected that the TSA would radiate most in the XY plane. Therefore the TSA was placed in the horizontal position, see picture D.1. Then the antenna was rotated over 360°, once to measure the polarization orientated along $P_{horizontal}$ and once to measure the polarization orientated along $P_{vertical}$.
The strongest radiation was found when the TSA was placed in the horizontal position and the polarization along $P_{horizontal}$ was measured. The cross polarization was determined by calculating the difference between the maximum received power of the co polar component to the maximum received power of the cross polar component. The cross polarization was 10 dB. The simulation results from ADS Momentum were obtained by cutting the radiation pattern at an angle of $\theta = 29°$. because in the simulations there is a null in the radiation pattern at $\theta = 90°$ see Figure 6.14. In Chapter 6 the TSA radiation pattern was cut at a different angle. The antenna was re-simulated for the measurements in this section, there was no moulding layer covering the antenna and the horizontal currents on thick metals were simulated. The strongest radiation was now found for one of the two beams above the XY plane. The radiation pattern in Figures 7.18 and 7.19 is rotated 90 degrees clockwise compared to the Figure 6.17.

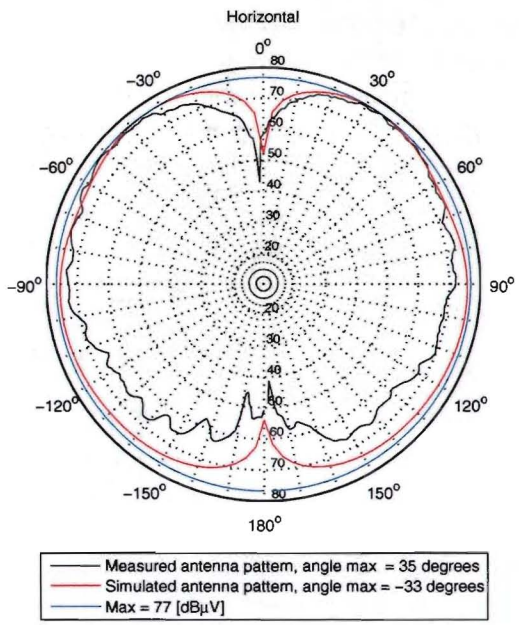

Figure 7.18: The radiation pattern of the TSA in the horizontal position, polarization along $P_{horizontal}$.

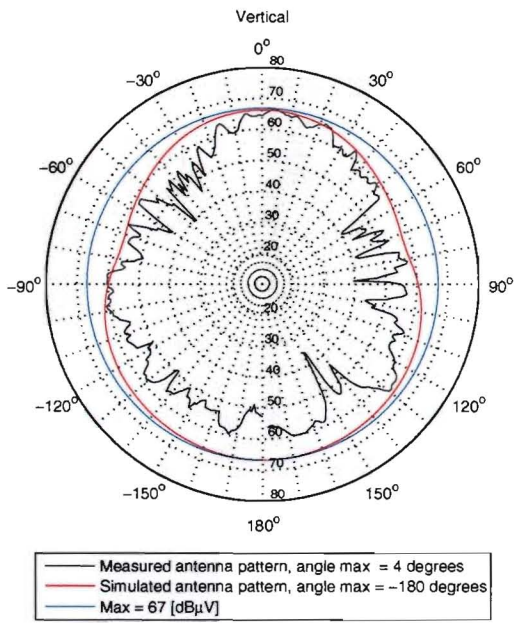

Figure 7.19: The radiation pattern of the TSA in the horizontal position, polarization along $P_{vertical}$.

Next the TSA was placed in the vertical position, in the YZ plane, see picture D.2. The antenna was rotated over 360° once to measure the polarization along $P_{horizontal}$ and once to measure the polarization along $P_{vertical}$. The strongest radiation was found for polarization along the $P_{vertical}$. This polarization angle was not measured in the horizontal plane. The cross polarization was found to be 8 dB.

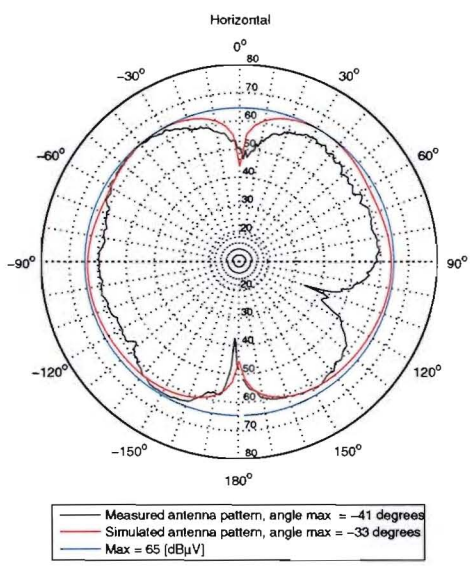

Figure 7.20: The radiation pattern of the TSA slot antenna in the vertical position, polarization along the $P_{horizontal}$.

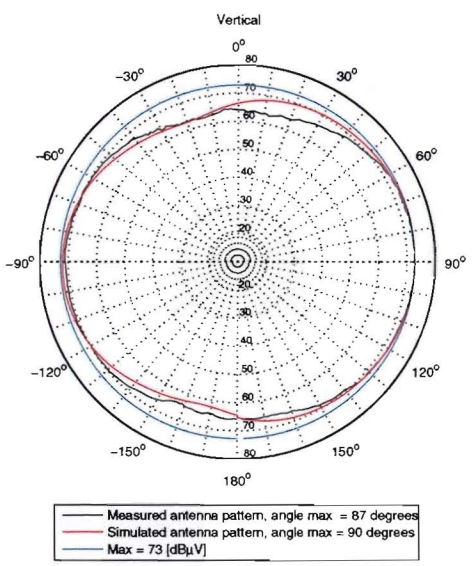

Figure 7.21: The radiation pattern of the TSA slot antenna in the vertical position, polarization along $P_{vertical}$

The second antenna that was measured was the bow-tie slot antenna designed for 24 GHz. In the simulations there is a null in the horizontal $\theta = 90°$ plane see Figure 6.29, to obtain the simulated results the θ angle was set to 60° corresponding to the maximum in the θ plane. The radiation pattern in Figures 7.22 and 7.23 is rotated 90 degrees clockwise compared to Figure 6.32.

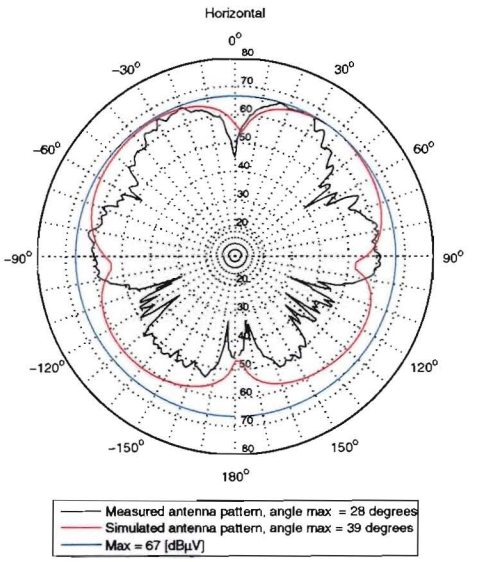

Figure 7.22: The radiation pattern of the bow-tie slot antenna in the horizontal position, polarization along $P_{horizontal}$.

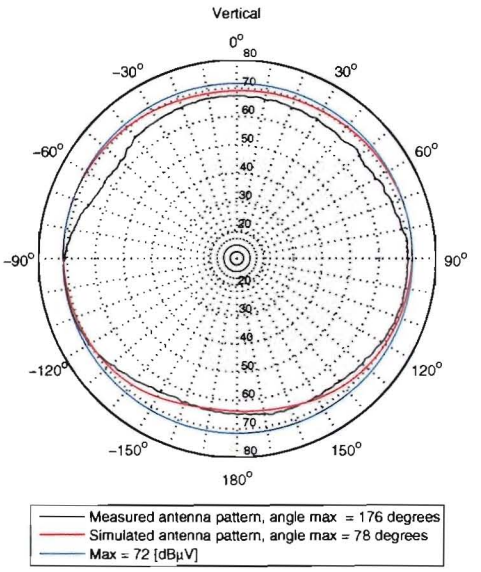

Figure 7.23: The radiation pattern of the bow-tie slot antenna in the horizontal position, polarization along $P_{vertical}$.

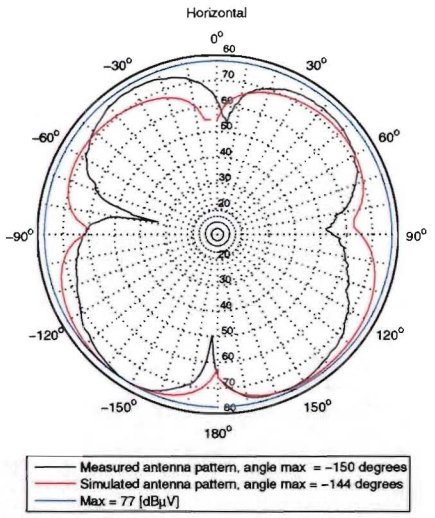

Figure 7.24: The radiation pattern of the bow-tie slot antenna in the vertical position, polarization along $P_{horizontal}$.

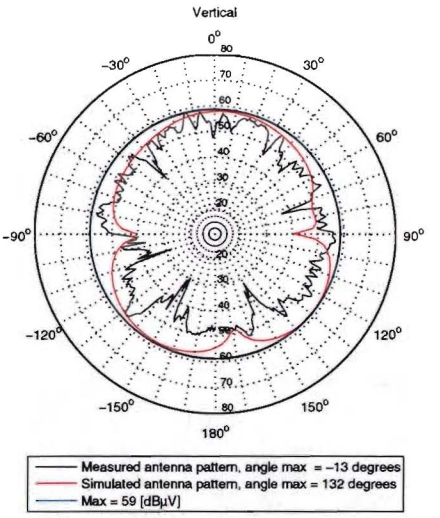

Figure 7.25: The radiation pattern of the bow-tie slot antenna in the upright position, polarization along $P_{vertical}$.

The cross polarization was found to be 5 dB. The radiation pattern has two main lobes and two weaker lobes where the weaker lobes were found on the connection side of the antenna. For the last measurement the bow-tie slot antenna was placed in the vertical position, in the YZ plane

and the polarization along $P_{horizontal}$ and the polarization along $P_{vertical}$ were measured. The strongest component was the polarization along $P_{horizontal}$. The radiation pattern in Figure 7.24 is rotated 90 degrees counter clockwise compared to Figure 6.31. The cross polarization was found to be 18 dB.
There was no measurement equipment available to perform measurements on the bow-tie antenna designed for 60 GHz.
There were no possibilities to measure the absolute gain of the antennas in the EMC room. However the relative gain of the antennas could be measured. Therefore a two port measurement was made with a vector network analyzer. A patch antenna comparable to the antenna described in Section 5.2 was used as a reference. The polarization was vertical and the gain of this antenna is 6.7 dBi see Table 5.1. First the S21 parameter of two reference antennas was determined. Then one of the reference antennas was replaced by the antenna under test and the S21 parameter was measured. Thereafter the S21 parameter of two antennas under test was measured. Based on these three measurements the relative gain could be determined. In all cases the antennas were positioned in such a way that the S21 parameter between the antennas reached a maximum. The results of the 24 GHz measurements are given in Table 7.2, in this case the power was averaged over the bandwidth 23.5 to 26.5 GHz. A better bandwidth would have been 22 to 29 GHz corresponding to the frequency band as presented in Section 3.1.1. However the patch antenna does not have a large bandwidth and measuring over the 22 to 29 GHz band would produce gains that are too high. This can be explained by the higher return loss of the patch antenna when measuring outside the radiation band. The upper frequency was fixed by the upper frequency of the network analyzer which is 26.5 GHz.

Antenna	Received power at 20 cm
TSA - TSA	-40.3 dB
Patch - TSA	-38.9 dB
Difference	-1.4 dB
Patch - Patch	-39.2 dB
Patch - TSA	-38.9 dB
Difference	0.3 dB
Bow-tie 24 - Bow-tie 24	-42.2 dB
Patch - Bow-tie 24	-41.4 dB
Difference	-0.8 dB
Patch - Patch	-39.2 dB
Patch - Bow-tie 24	-41.4 dB
Difference	-2.2 dB

Table 7.2: The receive power for different antenna combinations of the bow-tie slot antenna and the tapered slot antenna with the reference patch antenna in the frequency band 23.5 to 26.5 GHz.

In addition the measured maximum received power of the antennas under test were compared to the maximum received power of the patch antenna. The results of this measurement are given in Table 7.3. In this Table the gain based on the measurement in the EMC room is given.

Antenna	Received power
TSA -Horn	76.8 dBμv
Patch Horn	77.2 dBμv
Difference	-0.4 dB
Gain	6.3 dBi
Horn bow-tie 24	77.0 dBμv
Horn patch	77.2 dBμv
Difference	-0.2 dB
Gain	6.5 dBi

Table 7.3: The maximum received power measured in the EMC room at 24 GHz.

In Table 7.4 the differences in power have been translated in to the gain of the antenna. There is a spread of about 2 dB in the gain. This is inherent to the measurement.

Antenna	Gain
Tapered slot	5.3 - 7.0 dBi
Bow-tie for 24 GHz	4.5 - 6.5 dBi

Table 7.4: The measured antenna gains of the bow-tie slot antenna at 24 GHz and the tapered slot antenna.

The same measurement procedure has been repeated for the bow-tie slot antenna at 60 GHz. The reference antenna was the horn antenna that was used for the radio propagation experiments see Table 8.1. Only one reference antenna was available. However this measurement failed due to problems with finding the best alignment.

7.4 Summary antenna measurement

In Chapter 6 the simulated results of the antennas that were selected for fabrication were presented. In this chapter the results of the measurements of the fabricated antennas have been presented. In this Section the simulated and measured results will be compared. In addition the performance of the antennas is compared to the requirements set in Chapter 3.
In the case of the TSA sample three was selected. This selection was based on the lower return loss over the entire bandwidth. In Table 7.5 the requirements, simulated and measured results of the antennas designed for the automotive radar system are given. The most important requirement was the bandwidth requirement of 5 GHz. This requirement was met by the tapered slot antenna and the bow-tie slot antenna based on the simulated and the measured return loss bandwidth. The bandwidth of the bow-tie slot antenna is correctly placed in the allocated spectrum. In addition the bandwidth of the fabricated antenna is larger than the simulated bandwidth. The return loss bandwidth of the tapered slot and was not placed correctly in the allocated spectrum based on the measured data. The measured bandwidth of the tapered slot antenna is larger than the simulated bandwidth. An antenna gain of at least 6.5 dBi is required. This requirement is not met by the bow-tie slot antenna at 24 GHz. The measured and simulated gain are comparable. In setup a gain was measured with the TSA that meets the requirement. There is however a large spread in the gain measurements. The measured gain of the TSA is higher than the simulated value. However the requirement gain is not met by these antennas.

		Bow-tie 24 GHz		TSA	
Parameter	Requirement	Simulated	Measured	Simulated	Measured
f low	22 GHz	15.3 GHz	14.3 GHz	20.8 GHz	25.2 GHz
f high	29 GHz	30.1 GHz	33.3 GHz	28.9 GHz	>40 GHz
BW	5 GHz	14.8 GHz	19.0 GHz	8.1 GHz	>14.8 GHz
Gain	> 6.5 dBi	4.7 dBi	4.5 - 5.9 dBi	3.4 dBi	5.3 - 7.0 dBi
Directivity	N.A.	6.4 dBi	N.A.	6.0 dBi	N.A.
Efficiency	N.A.	67.8 %	N.A.	55%	N.A.
Mean Group delay	N.A.	0.16 ns	1.8 ns	0.13 ns	2.3 ns
Max Group delay	N.A.	0.32 ns	4.6 ns	-0.51 ns	4.3 ns
Polarization	N.A.	Vertical	Vertical	Horizontal	Horizontal
Cross polarization	N.A.	4.21 dB	18 dB	4.76 dB	10 dB

Table 7.5: Simulated and measured antenna parameters of the antennas designed for 24 GHz.

The radiation pattern of the tapered slot antenna has two beams radiating along the x-axis, see Figure 6.2. The two beams are polarized along the y-axis. This meets the expectations based on the simulated results. The radiation pattern in the XZ plane see Figure 6.2 was not measured. One measurement of the radiation pattern with $\theta = 0°$ was available. The measured radiation pattern was not below -35 dB of the radiation pattern measured in the ZX plane. Therefore this requirement is not met.
The radiation pattern of the bow-tie antenna is more complicated. The antenna is placed along the z-axis see Figure 6.21. The strongest radiation of the bow-tie antenna for 24 GHz is found in the YZ plane and is orientated along the x-axis. The radiation pattern consist of 4 beams. There is also a polarization component orientated along the z-axis which reaches its peak value at the y-axis. The radiation in the XZ-plane was considerably less strong however the requirement of -35 dB is not met.
A scaled version of the bow-tie slot antennas had been designed to operate at 60 GHz. The requirements in addition to the simulated and measured results are given in Table 7.6. The main

		Bow-tie 60 GHz	
Parameter	Requirement	Simulated	Measured
f low	59 GHz	48.0 GHz	42.0 GHz
f high	64 GHz	65.2 GHz	61.5 GHz
BW	5 GHz	17.2 GHz	20.5 GHz
Gain	N.A.	2.7 dBi	N.A.
Directivity	N.A.	4.7 dBi	N.A.
Efficiency	N.A.	63.2 %	N.A.
Mean group delay	N.A.	0.10 ns	1.3 ns
Max group delay	N.A.	0.12 ns	3.2 ns
Polarization	N.A.	Horizontal	Horizontal
Cross polarization	N.A.	2.6 dB	N.A.

Table 7.6: Simulated and measured antenna parameters of the antenna designed for 60 GHz.

requirement of a return loss bandwidth of at least 5 GHz was met by the simulated and fabricated design. The upper frequency of the measured bandwidth is placed too low. The simulated gain of

the bow-tie slot antenna for 60 GHz was 2.7 dBi. The measurement of the gain failed. Although no requirement was set to the gain it is believed that this gain is too low since the path loss at 60 GHz is very high.
There are no measurements of the radiation pattern of the bow-tie slot antenna for 60 GHz. It was expected that the radiation pattern is comparable to the radiation pattern of the bow-tie slot antenna for 24 GHz. This assumption is based on the fact that the bow-tie antenna for 60 GHz is a scaled version of the bow-tie antenna for 24 GHz. Simulations have shown that the radiation pattern is not the same as for the bow-tie slot antenna at 24 GHz. In addition while the polarization of the bow-tie for 24 GHz is vertical a horizontal polarization was found for the bow-tie for 60 GHz. A simple measurement with the reference fan beam antenna has proofed the simulated result. The difference can be explained by the dimensions of the stub and the slot. Although the antenna was first scaled the width of the top end of the stub was later decreased.

Chapter 8

Small-scale indoor radio channel measurements

In wireless systems the transmitting antenna emits an electromagnetic wave that follows a path through space and is received by the antenna of the receiver. The path of the electromagnetic wave can be a direct line of sight (LOS) or can be an indirect non line of sight path (NLOS). The radio coverage can be estimated with the large-scale propagation models. Large-scale models predict the average received signal strength over large distances when compared with the wavelength. The strength of the received signal over small distances, in the order of tens of wavelengths, is predicted by the small-scale or fading models. This chapter focuses on the small-scale models. In this project two frequencies are investigated, namely 24 GHz for the car radar system and 60 GHz for the wireless LAN system. The 24 GHz band is used in an outdoor environment. This complicates the measurement procedure of small-scale measurements. In addition the envisioned application does not need small-scale measurements. The 60 GHz band will be used for an indoor wireless LAN system. Up till now there has not been much research in the field of 60 GHz small-scale measurements. In this chapter the theory of small-scale measurements and the results of measurements that were performed at the Eindhoven University of Technology will be presented.

In the past large-scale measurements as well as ray tracing simulations have been performed at the Eindhoven University of Technology. The room that was used for these measurements has however changed since the last measurement. These simulations can nonetheless give an idea of the expected values for the small-scale measurements for more information about these measurements see reference [21].

In the first Section 8.1 the properties of an indoor radio channel will be treated. In the second section the measurement setup will presented 8.2. In the next two sections 8.3 and 8.4 the time dispersion parameters and the fading statistics will be treated respectively. The results of the measurements are presented in the next Section. In the last Section a summary of the measurement results will be presented.

8.1 Indoor radio channels

The measurements performed in this project focus on an indoor environment in which the transmitting and receiving antenna are placed in the same room. In this environment the radio waves travelling between the receiving and transmitting antenna are reflected, scattered or diffracted.

Due to this specific nature of this environment a large number of paths exist between the receiving and transmitting antenna. This fenomenon is commonly referred to as multipath propagation. Indoor radio channel measurements are performed over two different ranges. In the first range the separation between the antennas is varied with distances larger than the wavelength of the transmitted signal. In the second range the separation between the antennas is varied with distances smaller than the wavelength of the transmitted signal. The first range is referred to as large-scale measurements, the second range is referred to as small-scale measurements. This project focuses on the small-scale effects of radio channels at 60 GHz. The large-scale effects of outdoor environments are not considered.

In indoor radio channels rapid fluctuations in the amplitude, phase, or multipath delays of a radio channel over a short period of time or travel distance exist, see reference [22]. These rapid fluctuations are caused by the interference of one or more versions of the transmitted signal which arrive at the receiver at slightly different times. This interference produces three effects.

1. Rapid changes in signal strength over a small distance or time interval.

2. Random frequency modulation due to varying Doppler shifts on different multipath signals.

3. Time dispersion caused by multipath delays.

Four different factors can be distinguished that influence small-scale fading.

1. **Multipath propagation:** Objects might be placed along the transmission path. The emitted radio signal is reflected or scattered by these objects. This results in the arrival of multiple versions of the emitted radio signal that differ in magnitude, phase, angle of arrival and time of arrival. These versions are added vectorially which results in fluctuations in signal strength. This is illustrated by figures 8.2 and 8.3. In these figures the power of the received signal in the XY plane at one frequency component is depicted. The large nulls and peaks in the signal, which are typical in narrowband fading, are clearly visible. More information about the measurement of figures 8.2, 8.3, 8.4 and 8.5 can be found in Table 8.3 under measurement M7.

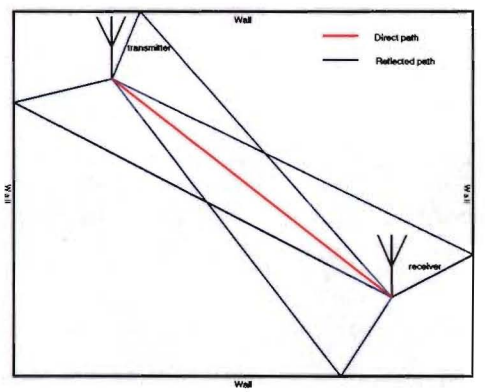

Figure 8.1: Multipath propagation in an indoor environment.

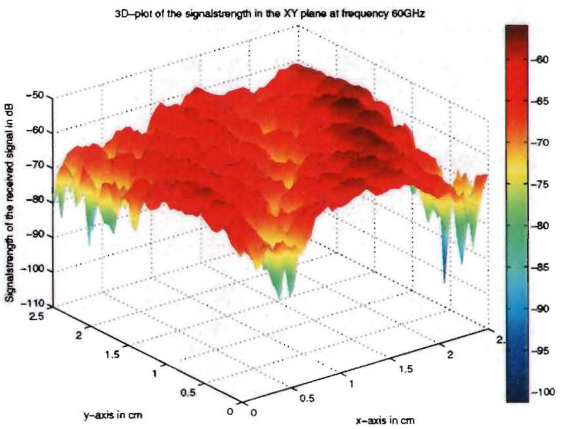

Figure 8.2: The power of the received signal in the XY plane of one frequency component, 60 GHz depicted in a three dimensional plot.

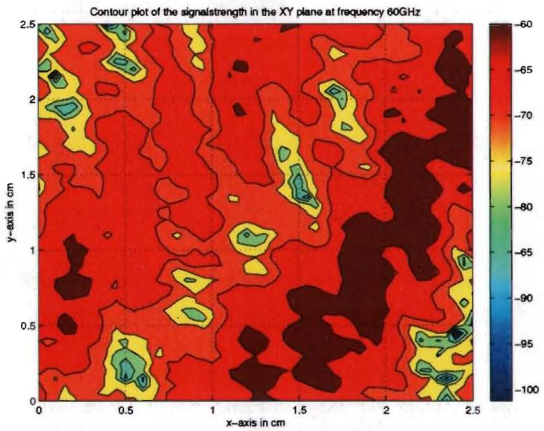

Figure 8.3: The power of the received signal in the XY plane of one frequency component, 60 GHz depicted in a contour plot.

2. **Bandwidth of the transmitted signal:** A bandwidth can be defined for the radio channel in which two frequency components have a strong amplitude correlation. If the bandwidth of the transmitted signal is larger than the bandwidth of the radio channel, then the received signal will be distorted. However the signal strength will not fade much over a small area. This situation is referred to as frequency selective fading.
In the other case, the bandwidth of the signal is smaller than the bandwidth of the radio channel, the amplitude of the received signal will vary rapidly over a small area. This situation is referred to as flat fading. The signal will however not be distorted.

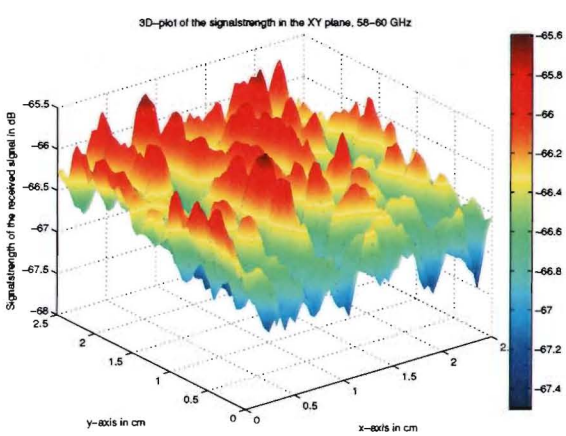

Figure 8.4: Three dimensional plot of the power of the received signal in the frequency range 58-60 GHz in the XY plane.

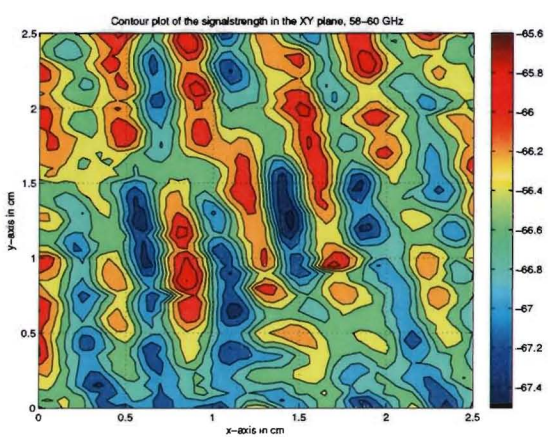

Figure 8.5: Contour plot of the power of the received signal in the frequency range 58-60 GHz in the XY plane.

The difference between the total energy over a frequency range and the power of one frequency component in the XY plane can be clearly seen by comparing figures 8.2 and 8.3 with figures 8.4 and 8.5. The figures 8.2 and 8.3 will vary for different frequencies, by

taking the total power over the bandwidth under consideration the fading effects will be averaged out. By increasing the bandwidth the fading will become less however the signal distortion will increase.

3. **Speed of the receiver:** The relative speed between the transmitter and the receiver results in a random frequency modulation due to Doppler shifts on each of the multipath components.

4. **Speed of objects in the transmission path:** the motion of objects along the transmission path induces a time varying Doppler shift on the multipath components.

The measurements performed in this project where performed during hours when there were no employees at work. The speed of the receiving antenna, the transmitting antenna as well as the objects in the environment during the measurements was zero. Therefore the factors indicated with number 3 and 4 as described above can be neglected. As a consequence the radio channel can be considered as wide sense stationairy. Moreover it is assumed that the waves arriving at the receiver and following different paths are uncorrelated in attenuation, phase shift and time delay. This is referred to as uncorrelated scattering. This type of radio channels is referred to as wide sense stationary uncorrelated scattering (WSSUS) channels.

In reference [22] a general model for the radio channel is given. Here the radio channel is modelled as a linear filter with a time varying impulse response. The time variation is caused by the movement of the receiver or objects along the transmission path. The filtering nature of the channel is caused by the summation of the amplitudes of multipath components and the delays of the multipath components. The received signal, $y(d,t)$, is given by the convolution of the transmitted signal, $x(t)$, with the impulse response of the radio channel, $h(d,t)$.

$$y(d,t) = x(t) \star h(d,t) = \int_{-\infty}^{t} x(t)h(d,t-\tau)d\tau \tag{8.1}$$

where d represents the location of the receiver and τ represents the delay in seconds due to the multipath propagation. In this case the excess delay is taken, that is the amount of time after the arrival of the first multipath component. This excess time delay can be divided into N bins. The resolution in the time domain is dependent on the bandwidth of the measurement B.

$$\begin{aligned} \Delta f &= \frac{B}{N} \\ (\Delta f \cdot 2\pi) \cdot \Delta\tau &= \frac{2\pi}{N} \\ \Delta\tau &= \frac{1}{N\Delta f} \end{aligned}$$

The width of a bin is given by $\Delta\tau$ and represents the time resolution.
The baseband impulse response of the radio channel can be given by:

$$h(t,\tau) = \sum_{i=0}^{N-1} a_i(t,\tau)e^{j\phi_i(t,\tau)}\delta(\tau-\tau_i) \tag{8.2}$$

where $a_i(t,\tau)$ represents the real amplitude of the i^{th} multipath component, $\tau_i(t)$ is the excess delay of the i^{th} bin and $\phi_i(t,\tau)$ represents the additional phase shifts that were encountered in

the channel at time t. In this project the radio channel was assumed to be wide sense stationary, therefore the time dependence t can be removed. The simplified version is given by:

$$h(\tau) = \sum_{i=0}^{N-1} a_i(\tau) e^{\theta_i(\tau)} \delta(\tau - \tau_i) \tag{8.3}$$

In the next the used measurement setup will be treated.

8.2 Measurement setup

In this Section the used measurement setup is described. An important parameter of the radio channel is the distribution of the amplitude of the received signal. To obtain the distribution a large number of measurements have to be performed in a small area. In this project a XY table was used to precisely move the receiving antenna over fractions of the wavelength. The receiving antenna can be moved on the Table with steps which can be as small as a fraction of the wavelength corresponding to the upper frequency of the measurement that is performed. The area over which the transmit antenna can be moved is 1.02 m by 0.82 m. On each point on the XY table the frequency transfer function is measured by a vector analyzer (HP 8510C). Each measured frequency transfer is transferred to a PC where it is stored for further processing. The measurement setup is depicted in Figure 8.6. This network analyzer can not measure signals up to 60 GHz. Therefore two mixers are used which up convert the signal to 60 GHz.

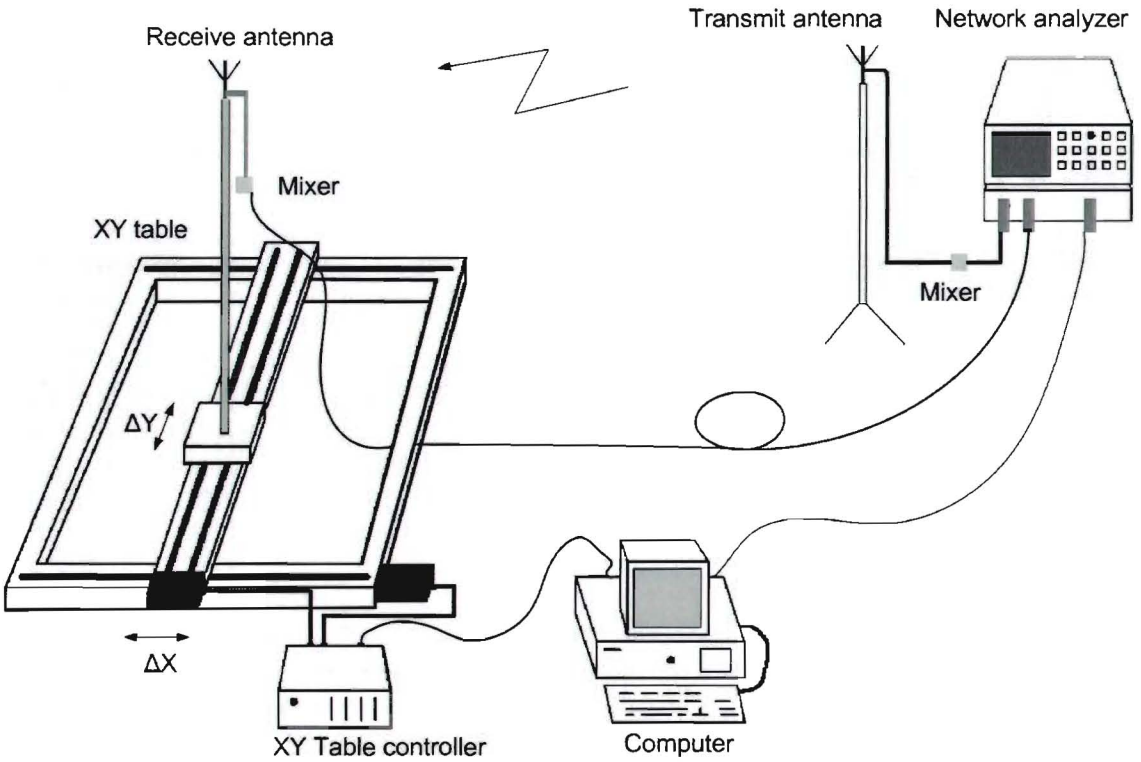

Figure 8.6: Measurement setup.

The transmit antenna is connected to the network analyzer by waveguides. The receive antenna is connected by semi rigid cables to enable displacement of the antenna. Three different antennas have been used. In Table 8.1 the parameters of the used antennas are included. The omni directional and fan beam antennas were the same antennas as used in reference [21]. The fan

	Half power beam width		
Type of antenna	Vertical-plane	Horizontal-plane	Gain
Omni directional	9.0°	omni directional	6.5 dBi
Fan beam	12.0°	70.0°	16.5 dBi
Bow tie	N.A.	N.A.	2.7 dBi (simulated)

Table 8.1: The parameters of the antennas used in the measurements.

beam antenna was pointed at the transmit antenna in the LOS situation or was pointed along the shortest path in the NLOS situation. The bow-tie antenna was placed in the XZ plane see Figure 6.21 where the y-axis is aligned with the shortest path for the LOS and NLOS situations.
Two types of measurements have been performed. In the first type a direct line of sight path existed, in the second type there was no direct line of sight path. In addition of the six measurements (two types times three antennas) two measurements have been performed with a higher resolution in the frequency domain and more data points in the spatial domain. In total eight measurements have been performed.

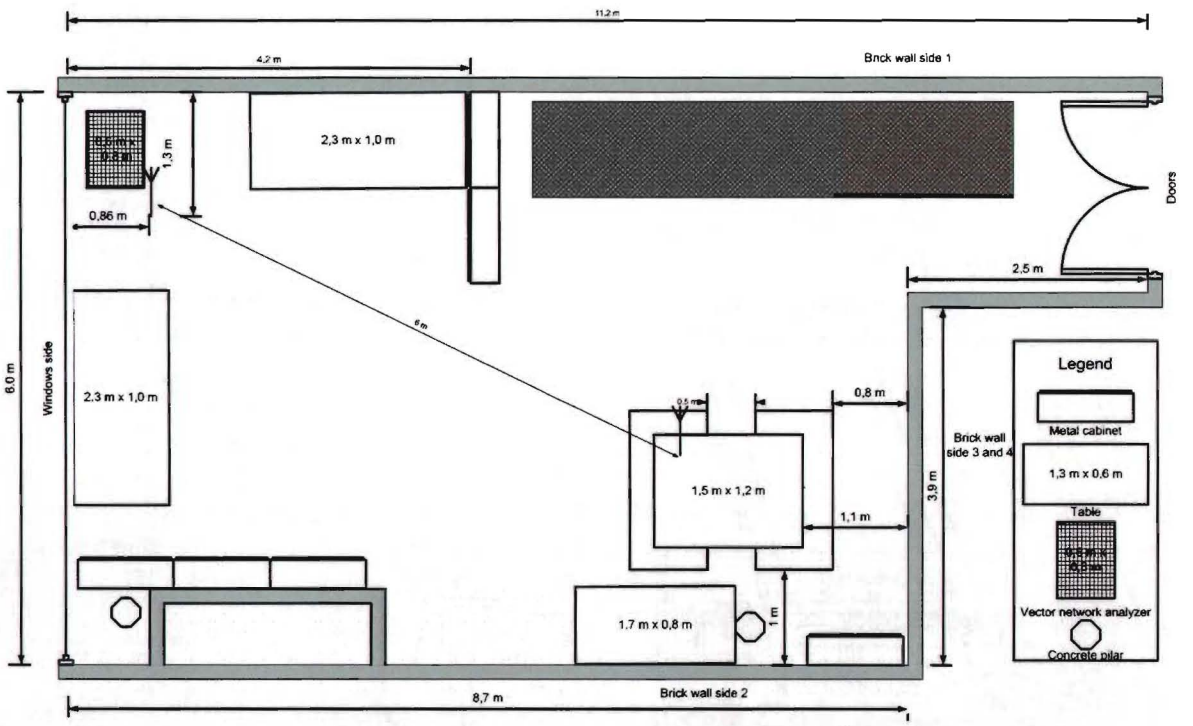

Figure 8.7: Topography of the measurement room at the Technical University of Eindhoven for the line of sight measurement.

The dimensions of the room are $11.2 \times 6.0 \times 3.2m^3$. The long sides are made off brick walls. The window side consists of window glasses with a metallic frame ranging from one meter above the

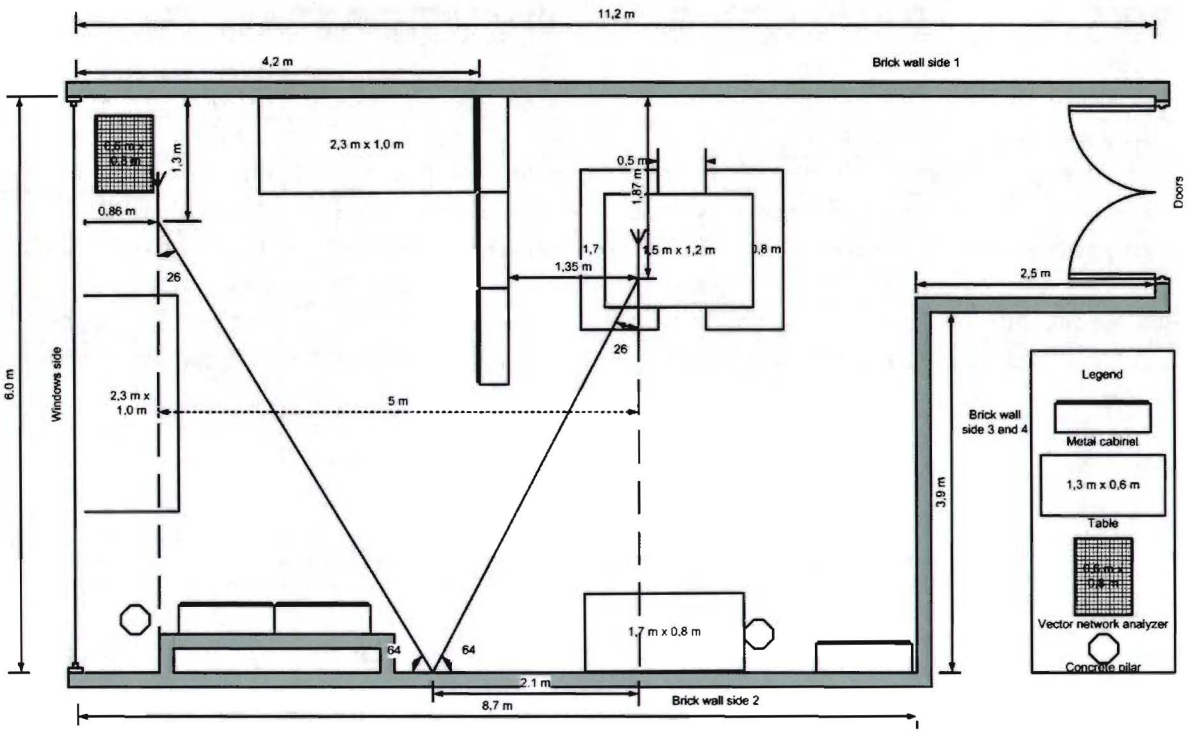

Figure 8.8: Topography of the measurement room at the Technical University of Eindhoven for the non line of sight measurement.

floor up to the ceiling and a metal heating radiator below the windows. Outside the building, the windows are covered with a thin cool shade curtain made of copper, not depicted in the figure. The floor is made of concrete covered with linoleum and the ceiling is also made of concrete but covered with aluminium plates and light holders. Two aligned cabinets are located in the middle of the room. To create a true NLOS area, a cabinet is moved to elongate the cabinet wall and the spaces between the cabinets and the ceiling are blocked by aluminium foil. The antennas were placed at a height of 2 meters above the ground. The topography of the measurement room is depicted in Figure 8.7 for the LOS setup and in Figure 8.8 for the NLOS setup.

The network analyzer measures the S21 parameter in the frequency domain. The maximum number of points in the frequency domain was 801. The network analyzer was calibrated before each measurement. Therefore the antennas were removed from the setup and the waveguides were connected at the end points, thus the reference plane was placed at the connection point of the antennas. The network analyzer was calibrated with a thru calibration. [1] Next the S21 parameter is measured and recorded at each point in the measurement area. The database with recorded S21 parameters is then loaded into Matlab for further processing. The recorded S21 parameters are multiplied by a Gaussian window with $a = 0.886B$ where B represents the bandwidth. This results in a sidelobe level of -42 dB, see reference [23]. This filter is not causal, therefore a delay is added. Thereafter the discrete Fourier is applied to the filtered S21 parameter.

In Table 8.2 the configuration of measurement M1 up till M6 is presented where O stands for omni directional, F for Fan beam and BT for bow-tie. In each measurement only one parameter

[1] The bow-tie antenna is fitted with a coax connector. Therefore an adapter is used to connect this antenna to the waveguide. The calibration of this setup is performed without the adapter.

Parameter	M1	M2	M3	M4	M5	M6
Antenna type	O-O	O-BT	O-F	O-O	O-BT	O-F
Environment	LOS	LOS	LOS	NLOS	NLOS	NLOS
Antenna height	2 m	2 m	2 m	2 m	2 m	2 m
Shortest path length	6 m	6 m	6 m	10 m	10 m	10 m
Lower frequency	58 GHz	58 GHz	58 GHz	58 GHz	58 GHz	58 GHz
Upper frequency	60 GHz	60 GHz	60 GHz	60 GHz	60 GHz	60 GHz
N	201	201	201	201	201	201
Time resolution	0.5 ns	0.5 ns	0.5 ns	0.5 ns	0.5 ns	0.5 ns
Total measurement time	100 ns	100 ns	100 ns	100 ns	100 ns	100 ns
Number of wavelengths x direction	4	4	4	4	4	4
Number of wavelengths y direction	4	4	4	4	4	4
Points per wavelength	10	10	10	10	10	10
Runtime	9.5 h	9.5 h	9.5 h	9.5 h	9.5 h	9.5 h

Table 8.2: The parameters of the measurement where O stands for omni directional, F for fan beam and BT for bow-tie.

is changed which makes it easier to compare the results. In M4 up till M6 the space above the cabinets has been shielded with aluminium foil to construct a true NLOS situation. All the measurements presented in this Table have been performed during the night. Because of the absence of movement in and around the measurement room the radio channel can be considered stationary. However even during the day it is likely that the channel is stationary since signals at 60 GHz will not penetrate the walls. The choice of the number of points in the frequency domain and the number of data points is a compromise. To perform a statistical analysis it is important to have a large number of data points. This would however result in a very long runtime. This could be solved by measuring over less points in the frequency domain. Measuring over less points in the frequency domain would decrease the accuracy of the measurement. Taking into account both considerations a comprise has been made. In addition to the six measurements two other measurements were made. The settings of these two measurements are given in Table 8.3. The aim of these measurements was to obtain data at a higher resolution. This data has been used to calculate the coherence bandwidth. However no accurate value for the coherence bandwidth could be obtained with these settings. The reason is that the used vector network analyzer can only measure over 801 points and the measurement bandwidth is 2 GHz. Measurements M7 and M8 have also been used to plot the three dimensional plots of the strength of the received signal.
In the next two sections the parameters that are commonly used to describe the indoor small scale radio channel will be treated.

Parameter	M7	M8
Antenna type	O-O	O-O
Environment	LOS	NLOS
Antenna height	2 m	2 m
Shortest path length	6 m	10 m
Lower frequency	58 GHz	58 GHz
Upper frequency	60 GHz	60 GHz
N	801	801
Time resolution	0.5 ns	0.5 ns
Total measurement time	400 ns	400 ns
Number of wavelengths x direction	5	5
Number of wavelengths y direction	5	5
Points per wavelength	10	10
Runtime	65 h	65 h

Table 8.3: The parameters of the measurement where O stands for omni directional

8.3 Time dispersion parameters

The power delay profile (PDP) is an important tool for the evaluation of a radio channel. The PDP is given by the ensemble average of the squared absolute value of the transfer function $P_{PDD}(\tau) = E_d(|h(d)|^2)$ over an area in the order of several wavelengths. It represents the power output of the radio channel as a function of the excess delay τ with respect to a fixed time delay reference. The PDP at one position $P_{PDD}(\tau, d) = |h(\tau, d)|^2$ is commonly called the local PDP. The radio channel can be characterized by parameters derived from the PDP and the Fourier transform of the PDP. The power delay profile from a LOS measurement using two omni directional antennas is depicted in Figure 8.9. More information about this measurement can be found in Table 8.2 under measurement M1.
The local mean excess delay time is defined as:

$$\tau(d) = \frac{\sum_k a_k^2 \tau_k}{\sum_k a_k^2} \tag{8.4}$$

This is the first moment of the power delay profile. In Equation 8.4 it is assumed that the transmitted pulses can be described by Dirac pulses. However in most practical situations the pulses can not be described by Dirac pulses. Therefore a second method is used to calculate the local mean delay of the signal:

$$\tau(d) = \frac{\int_0^\infty t P_{PDD}(\tau, d) d\tau}{\int_0^\infty P_{PDD}(\tau, d) d\tau} \tag{8.5}$$

The second moment of the PDP is called the root mean square (RMS) delay spread and is defined as:

$$\sigma_\tau(d) = \sqrt{\bar{\tau^2}(d) - \tau^2(d)}$$

where

$$\bar{\tau^2}(d) = \frac{\sum_k a_k^2 \tau_k^2}{\sum_k a_k^2} \tag{8.6}$$

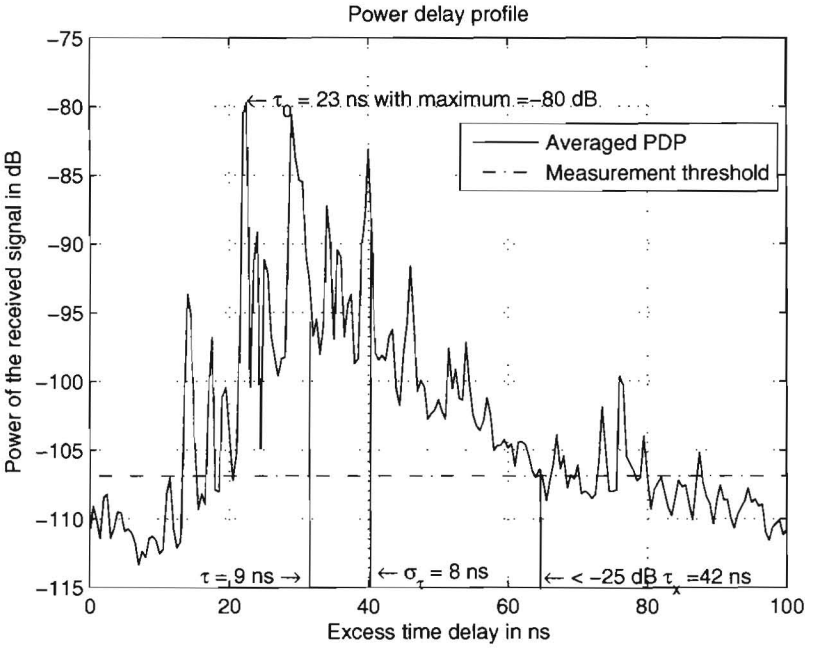

Figure 8.9: Power delay profile averaged over all measured points in the XY-plane, LOS measurement using two omni directional antennas, see Table 8.2 measurement M1 for more details.

The RMS delay spread can also be calculated by using integrals, the equation for the local RMS delay spread is then given by:

$$\sigma_\tau(d) = \sqrt{\frac{\int_0^\infty \left[\tau - \frac{\int_0^\infty tP_{PDD}(\tau,d)d\tau}{\int_0^\infty P_{PDD}(\tau,d)d\tau}\right]^2 P_{PDD}(\tau)d\tau}{\int_0^\infty P_{PDD}(\tau,d)d\tau}} \tag{8.7}$$

The RMS delay spread and the mean delay spread are measured from the time that the maximum signal arrives τ_0. The last time dispersion parameter from the PDP is the maximum excess delay τ_x. This time is defined as the excess delay for which the received signal energy falls to x dB below the maximum received energy of one of the multipath components. In this report the x dB was calculated as the time that the first peak of the PDP falls below x dB off the maximum received signal. The time dispersion parameters have so far been defined at a certain place d in the XY-plane. They are referred to as local time dispersion parameters. A more practical value for these parameters is obtained by taking the ensemble average of the parameters on all the points in the xy-plane. The ensemble average parameters are referred to as averaged time dispersion parameters and will be denoted by placing a bar over the parameter.

$$\begin{aligned} \bar{\tau} &= E_d(\tau) \\ \bar{\sigma_\tau} &= E_d(\sigma_\tau) \end{aligned}$$

In Figure 8.10 and 8.11 a three dimensional plot and a contour plot of the RMS delay spread parameter for all the data points in the xy-plane are given respectively.

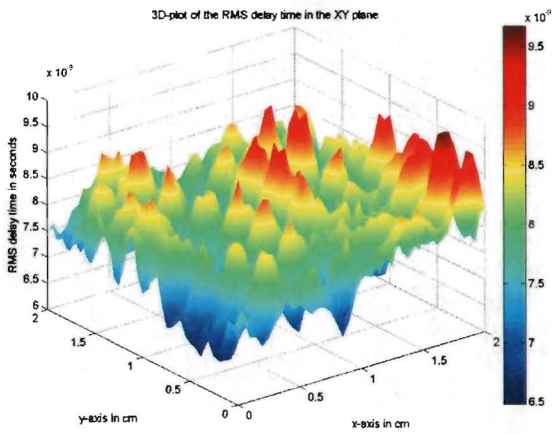

Figure 8.10: 3D plot of the RMS delay spread in the XY-plane for a LOS measurement, see Table 8.2 measurement M1 for more details.

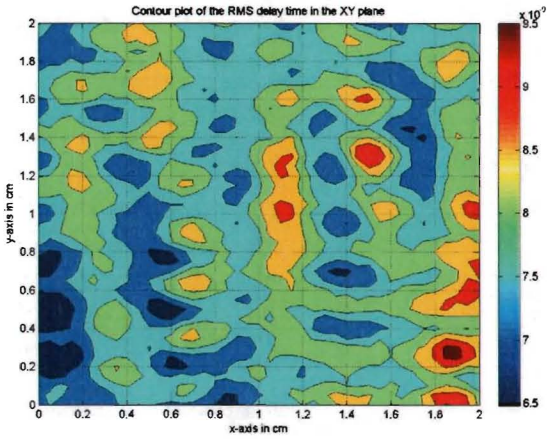

Figure 8.11: Contour plot of the RMS delay spread in the XY-plane for a LOS measurement, see Table 8.2 measurement M1 for more details.

In Figure 8.11 can be clearly seen that the RMS delay spread is clustered. There exist a relation between the amplitude of the signal and the RMS delay spread. This is shown is in Figure 8.12. In this case the RMS delay spread decreases with increasing received power. In other measurements the opposite effect has been found as well. In equations 8.5 and 8.7 the PDP is integrated between $0 \leq t \leq \infty$. However in practice the first signal does not arrive at $t = 0$ and the measurement time is finite. Therefore the integrating time is limited to $\tau_0 \leq \tau \leq t_{end}$ where τ_0 is the time that the strongest multipath component arrives. In Figure 8.9 can be seen that the received signals drown into the noise before the time $\tau = \tau_{end}$ is reached. Moreover in Equation 8.7 can be seen that the RMS delay time is dependent on τ^2. Therefore the noise will increase the RMS delay time for large values of τ. To prevent the influence of the noise on the time dispersion parameters the measurement time shortened $\tau_{end} \ll 1/B$. In this report the measurement time for the time dispersion parameters is $\tau_0 \leq \tau \leq \tau_x$.
Another parameter used to describe the radio channel is the coherence bandwidth. The coherence bandwidth is defined as the range of frequencies over which two frequency components have a strong potential for amplitude correlation, see reference [22]. In the coherence bandwidth all spectral components will be passed with approximately equal gain and phase. The coherence bandwidth B_c is determined by the range of frequencies for which the correlation function exceeds a fixed value i.e. 0.5 or 0.9. The correlation function is given as:

$$C(\Omega)(d) = \frac{\int_{\omega_1}^{\omega_2} H(\omega)H^*(\omega+\Omega)d\omega}{\int_{\omega_1}^{\omega_2} H(\omega)H^*(\omega)d\omega} \tag{8.8}$$

where $\omega = 2\pi f$, $C(\Omega)$ is the local correlation function evaluated in the band $\omega_1 < \omega < \omega_2$ and Ω is the frequency difference. $H(\omega)$ is the frequency domain representation of the impulse response and * indicates the complex conjugate. The ensemble average of $C(\Omega)$ over all data points in the XY plane is denoted by $E_d(C(\Omega)) = \overline{C(\Omega)}$. The correlation function of a NLOS measurement using two omni directional antennas is depicted in Figure 8.13. In this figure the average coherence bandwidth of all data points in the XY plane is depicted. In practical situations the equation given in 8.8 might not be applicable. To obtain an accurate value of the coherence bandwidth a high resolution in the frequency domain is necessary. The effect of a low resolution

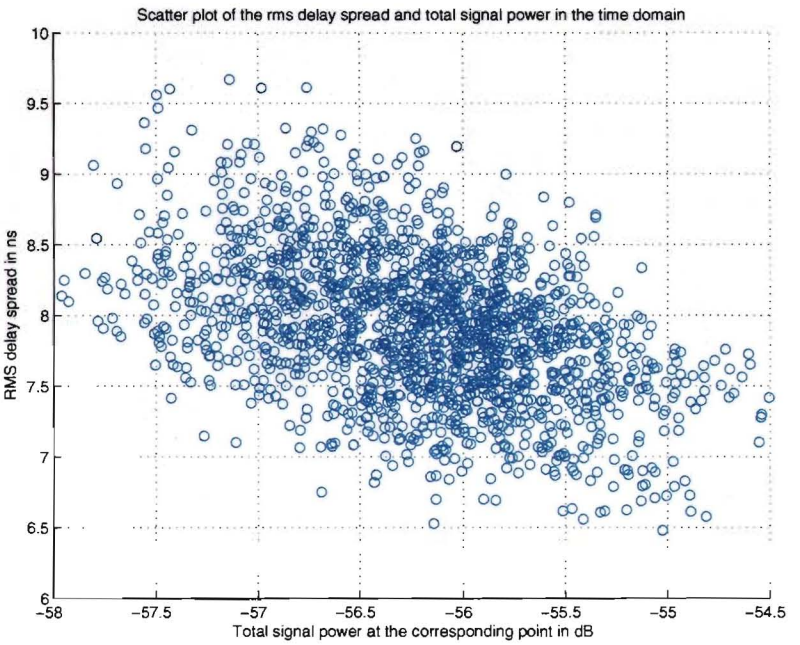

Figure 8.12: Scatter plot of the RMS delay spread and the total power in the time domain of the received signal for all data points in the xy-plane.

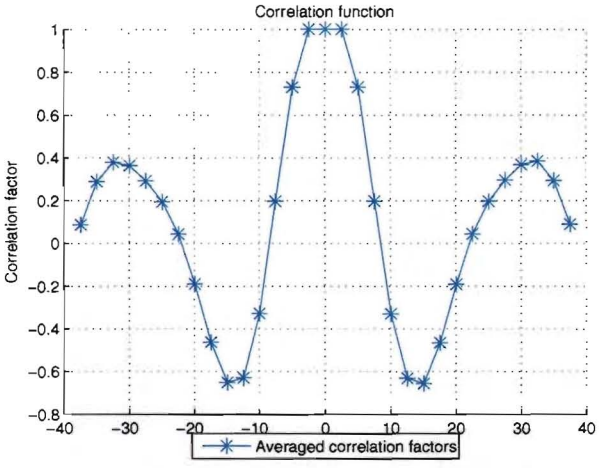

Figure 8.13: Correlation function $\overline{C(\Omega)}$ of a measurement in a LOS situation using two omni directional antennas plotted against Δf. The measurement bandwidth was 2 GHz and the number of points was 800 therefore the frequency resolution was 2.5 MHz see Table 8.3 measurement M8 for more details about this measurement.

is visible in Figure 8.13. The coherence bandwidth was found to be 5 MHz for a correlation factor of 0.9 and 10 MHz for a correlation factor of 0.5.

However when performing a wide bandwidth measurement the number of points per frequency sweep N is limited. Or in the case of small-scale measurements the measurement time per point in the XY plane can be limited. For example when performing a measurement during

the night the time is limited to about 12 hours. If the IF bandwidth and sweep time of the vector network analyzer are not changed increasing N will increase the measurement time. Therefore there is a tradeoff between the number of points in the XY plane and the number of points per frequency sweep N. A possible solution could be to decrease B. In this case B_c will only be valid for this smaller bandwidth. Considering this drawbacks two approximations are often used to obtain the coherence bandwidth see reference [22]:

$$B_c \approx \frac{1}{50\bar{\sigma}_\tau} \tag{8.9}$$

$$B_c \approx \frac{1}{5\bar{\sigma}_\tau} \tag{8.10}$$

Equation 8.9 is used if the correlation function is at least 0.9, Equation 8.10 is used if the correlation function is at least 0.5. When using the approximations the coherence bandwidths were found to be 1.96 MHz and 19.62 MHz for the correlation factors of 0.9 and 0.5 respectively.

8.4 Small-scale fading

Multiple versions of the transmitted signal arrive at the receiving antenna, these versions differ in amplitude, phase and delay. The phase of the received signal changes 180° when the receiving antenna is displaced 2.5 mm at 60 GHz. Generally the attenuation and time delay do not change considerably over such a distance. At the receiving antenna the versions are added vectorially. The difference in phase of the received signals causes peaks in the received power when the versions are added constructively or causes nulls when the versions are added destructively. This behavior is called small-scale fading and is superimposed on the large-scale path loss.

In the past many narrowband measurements were performed on radio channels at other frequencies. Based on these measurements the Rayleigh fading distribution was chosen to describe the statistical spatial varying nature of the received envelope of the signal. If the radio channel is measured over a bandwidth of B Hz then the time resolution Δt is given by $1/B$ s . When Δt is large a large number of multipath components M, will be received in one interval. The M multipath components will be vectorially added. The central limit theorem can now be used to find the distribution of the summed multipath components. Let $X_1, X_2, ...X_M$, be a set of M independent random variants and each X_i has an arbitrary probability distribution $P(x_1, x_2, ...x_M)$ with mean μ_i and variance σ_i then the variant has a limiting cumulative distribution function which approaches a normal (Gaussian) distribution. The normal distribution is given by:

$$P_{Normal}(r) = \frac{1}{\sqrt{2\pi}\sigma} e^{\frac{-r^2}{2\sigma^2}} \tag{8.11}$$

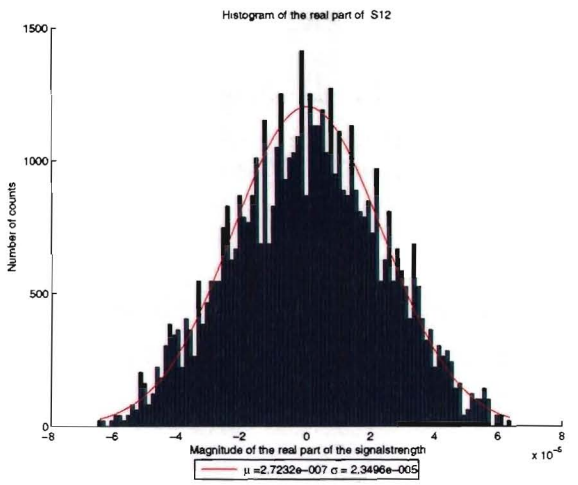

Figure 8.14: Histogram of the real part of the received signal of all the data points in the XY-plane. In red the fitted normal distribution is depicted.

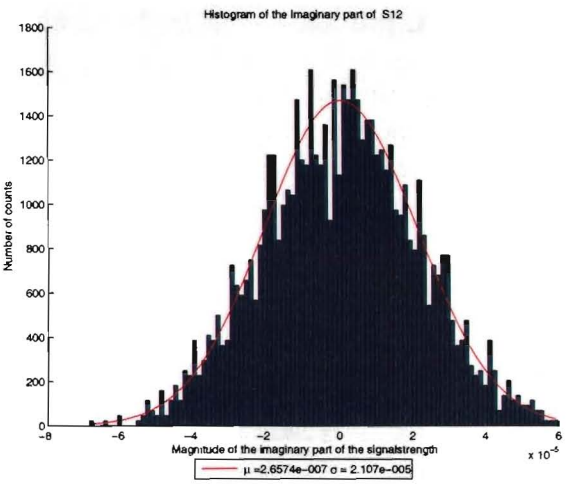

Figure 8.15: Histogram of the imaginary part of the received signal of all the data points in the XY-plane. In red the fitted normal distribution is depicted.

The amplitude of the received signal contains an in-phase x and a quadrature component y. The histogram of the in-phase (real) component is depicted in Figure 8.17, the histogram of the quadrature (imaginary) component is depicted in Figure 8.15. The obtain these results the settings from M7 given in Table 8.3 have been used. In addition all distribution have been analyzed in a time period with half the length of the measurement time. The amplitudes of both components will have a normal distribution if M is large, with means μ_1 and μ_2 and equal variance σ. If the in-phase and quadrature components have a Gaussian distribution with zero mean $\mu_1 = \mu_2 = 0$ then the amplitude of the received signal will follow a Rayleigh distribution:

$$f_R(r) = \begin{cases} \frac{r}{\sigma^2} e^{-\frac{r^2}{2\sigma^2}} & r > 0 \\ 0 & q \leq 0 \end{cases} \tag{8.12}$$

When the mean of the in phase and quadrature component is not zero $\mu_1 = \mu_2 \neq 0$, an additional component is present in the signal. This occurs for example when there is a LOS connection between the transmitting and receiving antenna. The amplitude of the received signal then has a Ricean distribution given by:

$$f_R(r) = \begin{cases} \frac{r}{\sigma^2} e^{-\frac{r^2+s^2}{2\sigma^2}} I_0(\frac{sr}{\sigma^2}) & r > 0 \\ 0 & r \leq 0 \end{cases} \tag{8.13}$$

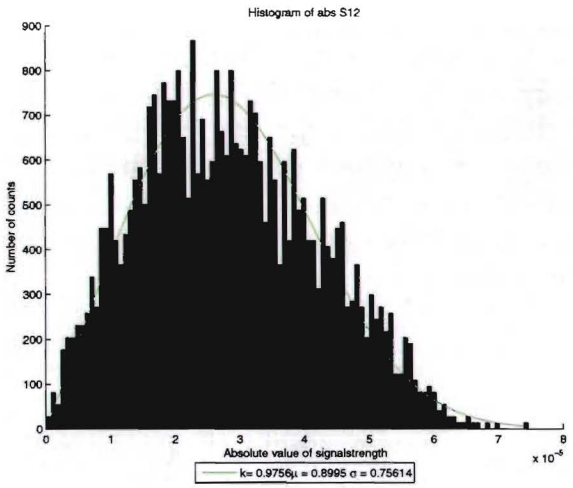

Figure 8.16: Histogram of the absolute value of the received signal of all the data points in the XY-plane. In green the fitted Ricean distribution is depicted.

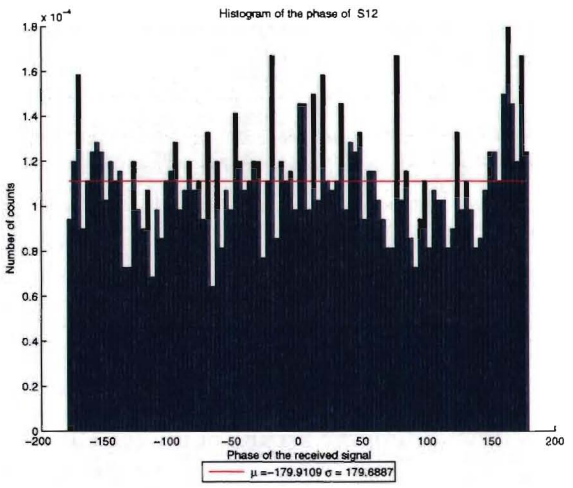

Figure 8.17: Histogram of the phase of the received signal of all the data points in the XY-plane. In red the fitted uniform distribution is depicted.

where s^2 and $2\sigma^2$ are the power of the dominant path and scattered paths respectively, I_0 is the o^{th} order modified Bessel function of the first kind.
The Ricean distribution can be described using the so-called k-factor. The k-factor is defined as the ratio between the power of the dominant path to the power of the other paths:

$$k(d) = \frac{P_{dominant}(d)}{P_{scattered}(d)} \tag{8.14}$$

where the τ_{max} is the moment in time when the dominant signal is received, $P_{scattered}(d)$ is measured over the entire measured time. In this project the following formula from [24] is used to calculate the k-factor:

$$K = \frac{\sqrt{1-\sigma_R^2}}{1-\sqrt{1-\sigma_R^2}} \tag{8.15}$$

where the variance of the Ricean distribution σ_R^2 is given by:

$$\sigma_R^2 = \frac{Var(R^2)}{(E(R^2))^2} \tag{8.16}$$

where R is a vector with elements $R_d = |\sum_{i=0}^{N-1} h_d(\tau_i)|$. With the k-factor and a scaling factor $\Omega_p = E(R^2)$ the PDF of the Ricean distribution can be written as:

$$f_R(r) = \frac{2(K+1)r}{\Omega_p} exp\left\{-K - \frac{(K+1)r^2}{\Omega_p}\right\} I_0\left\{2r\sqrt{\frac{K(K+1)}{\Omega_p}}\right\} \tag{8.17}$$

with $r \geq 0, K \geq 0, \Omega_p \geq 0$. The mean value μ_R of the Ricean distribution is given by:

$$\mu_R = \frac{E(R)}{\sqrt{E(R^2)}} = \sqrt{\frac{\pi}{4(K+1)}} exp\left(\frac{-K}{2}\right)\left[(K+1)I_0\left(\frac{K}{2}\right) + KI_1\left(\frac{K}{2}\right)\right] \tag{8.18}$$

A low K-factor $K \rightarrow 0$ indicates that there is no strong dominant path present, the amplitude distribution of the absolute value of the received signal will transform into a Rayleigh distribution. A high K-factor $K \gg 1$ indicates that a strong dominant path is present, the amplitude distribution will be approach a Gauss distribution. Regarding the phase of the received signal. It was found the phase distribution is not necessarily uniform. In some cases peaks were found around 180°. This occurred with the distributions of the phase for which a high k-factor was found in the amplitude distribution as well as in cases where a low k-factor was found in the amplitude distribution. More research is needed to clarify this behavior.

8.5 Measurement results

In this Section the results of the measurements are presented. The six measurements that were performed with a lower number of data points and resolution in the frequency domain will be presented. The figures for this Section are included in Appendix E

Parameter	LOS M1	LOS M2	LOS M3	NLOS M4	NLOS M5	NLOS M6
Mean P (60 GHz)	-70.0 dB	-70.3 dB	-60.3 dB	-77.7 dB	-72.7 dB	-62.7 dB
Var. P (60 GHz)	-150.8 dB	-153.5 dB	-136.2 dB	-163.5 dB	-163.1 dB	-145.6 dB
Max. P (60 GHz)	-61.8 dB	-61.4 dB	-53.3 dB	-66.7 dB	-65.8 dB	-57.0 dB
Min. P (60 GHz)	-100.8 dB	-105.6 dB	-94.7 dB	-107.9 dB	-95.8 dB	-91.6 dB
Mean BW Power	-67.3 dB	-70.8 dB	-61.0 dB	-73.0 dB	-72.3 dB	-65.8 dB
Var. BW Power	-191.4 dB	-205.7 dB	-182.5 dB	-200.8 dB	-214.9 dB	-190.3 dB
Max. BW Power	-66.4 dB	-70.2 dB	-60.3 dB	-72.1 dB	-71.8 dB	-65.1 dB
Min. BW Power	-68.2 dB	-71.5 dB	-61.7 dB	-74.0 dB	-72.8 dB	-66.7 dB

Table 8.4: The power of the received signal at 60 GHz and the total power in the frequency band between 58 GHz and 60 GHz.

In Table 8.4 the received power is given. In wide bandwidth measurements a clear difference can be seen between the power measured at one frequency component and the power measured over the entire bandwidth. In addition the received power is dependent on the used receive antenna, in all cases an omni directional antenna was used as transmitter. The lowest received power was observed when the bow-tie antenna was used. The highest received power was observed when a omni directional antenna was used as a transmitter and a fan beam antenna was used as a receive antenna. This can be explained by the higher gain and directivity of the fan beam antenna over the omni directional antenna and the bow-tie. A clear difference can be observed between the power measured at one frequency (60 GHz) for the LOS and NLOS case. The received power in the NLOS situation is 2.4 to 7.7 dB lower than in the LOS situation. When measuring the total power in the frequency band 58 - 60 GHz the received power in the NLOS situation is only 1.5 to 5.7 dB lower than the LOS situation. The distance between the transmit and receive antenna for the NLOS situation is larger and therefore the free space path loss is higher. In addition to the increase in free space loss there is also energy lost when the signal is reflected from the wall. In this case of the bow-tie antenna the received power is only 1.5 dB lower. The next parameters that were investigated are the time dispersion parameters. These parameters are given in Table 8.5. The length of the shortest path between the receive and transmit antenna was 6 m for the LOS situation and 10 m for the NLOS situation. The expected travel time will therefore be 20 ns and 33 ns for the LOS and NLOS situation respectively. However a time delay was added to the

τ_0	23 ns	5 ns	23 ns	36 ns	5 ns	36 ns
$\bar{\tau}$	9.09 ns	16.50 ns	6.60 ns	7.83 ns	12.17 ns	13.66 ns
max τ	11.21 ns	18.73 ns	8.31 ns	10.88 ns	16.86 ns	16.30 ns
min τ	6.71 ns	12.98 ns	5.19 ns	5.52 ns	11.72 ns	10.94 ns
$\bar{\sigma_\tau}$	7.92 ns	12.10 ns	7.15 ns	10.12 ns	12.98 ns	10.93 ns
max σ_τ	9.67 ns	14.05 ns	7.99 ns	11.55 ns	14.78 ns	11.73 ns
min σ_τ	6.48 ns	10.52 ns	6.21 ns	8.75 ns	11.18 ns	9.84 ns
-25 dB time	42 ns	54.50 ns[2]	26 ns	37 ns	54.5 ns[2]	36 ns
$\overline{B_{c=0.9}}$	20 MHz	20 MHz	20 MHz	20 MHz	20 MHz	20 MHz
$\overline{B_{c=0.5}}$	20 MHz	40 MHz	40 MHz	20 MHz	40 MHz	40 MHz
Apx. $B_{c=0.9}$	2.5 MHz	1.7 MHz	2.8 MHz	2.0 MHz	1.5 MHz	1.8 MHz
Apx. $B_{c=0.5}$	25.3 MHz	16.5 MHz	28.0 MHz	19.8 MHz	15.4 MHz	18.3 MHz

Table 8.5: The time dispersion parameters of the indoor radio channel. [2] x = -22 dB because the signal dropped below the noise level of -106 dB.

Gaussian filter to achieve a causal filter. This delay was approximately 2 ns. In the case that the bow-tie antenna was used a strange effect is observed. In this case the strongest signal arrives before the direct path component arrives. This effect has to be investigated further.

The RMS delay spread is comparable for the omni directional and fan beam receive antenna. The bow-tie receive antenna has the highest RMS delay spread of the six measurements for both LOS and NLOS situations.

The signal received by the bow-tie antenna has longest x dB time followed by the omni directional receive antenna and the fan beam receive antenna. The small -25 dB time of the fan beam antenna for the LOS situations can be explained by the fact that the antenna was pointed towards the transmit antenna and will therefore not see reflections coming from the walls behind the antenna.

In Section 8.3 the problem of the limited number of points in the frequency domain with respect to the coherence bandwidth was mentioned. In Table 8.5 this problem is clearly visible. The difference between the coherence bandwidth using Equation 8.8 and equations 8.9 and 8.10 is large. Therefore the latter equations are preferred.

In the figures E.4 till E.9 the impulse responses averaged over all the data points in the XY-plane for the measurements M1 to M6 are depicted. De scatter plots of the signal strength (in the time domain) against the RMS delay spread are given in figures E.10 to E.15. In most LOS situations the RMS delay spread decreases when the received signal strength increases. Except when the receiving antenna is a bow-tie antenna. In the NLOS situation the RMS delay spread increases when the signal strength increases.

In Section 8.4 the Ricean distribution has been treated. This distribution has been fitted to the measured absolute value of the summed received signal. In Table 8.6 the k-factors of these fitted curves are given. In the situation that the fan beam antenna is used as receive antenna the difference between the LOS and NLOS situation can be explained by the fact that the strongest component will be weaker for the NLOS situation. Another effect occurs for the bow-tie and omni directional antennas. Here the k-factor for NLOS situation is larger than for the LOS situation. The increase of the k-factor for the NLOS situation is an unexpected effect. Due to the absence of the direct path a k-factor which is lower than the k-factor in the LOS situation is expected. This

was the case when the fan beam antenna was used as a receiver. However, the opposite effect was measured when using the omni directional antenna and the bow-tie slot antenna. A possible explanation for the high k-factor of the omni directional antenna could be that there were more reflectors surrounding the antenna in the LOS situation then in the NLOS situation. Therefore, the power of scattered waves in the LOS was higher than in the NLOS situation. The explanation also applies to the bow-tie slot antenna. The fan-beam antenna will however not have received waves coming from these reflectors due to the narrow beam which was pointed at the transmit antenna.

Parameter	LOS M1	LOS M2	LOS M3	NLOS M4	NLOS M5	NLOS M6
k-factor	0.89	0.88	2.19	2.20	1.30	1.80

Table 8.6: The k-factor of the Ricean distribution.

In addition to the distribution of the amplitude the distributions of the phase are also given, see figures E.22 till E.27. In red the uniform distribution is given. This distribution fits the measured data well if two omni directional antennas were used. In the case that the bow-tie or the fan beam antennas were used the uniform distribution is no longer applicable. For both antenna types and for both situations there is a peak around 180°.

8.6 Conclusions

The indoor radio channel at 60 GHz was measured using a setup in which the receiving antenna could be displaced with steps of one tenth of the wavelength in order to obtain the small-scale characteristics. A total of eight small-scale radio channel measurements has been performed. Three different types of antennas have been used, an omni directional antenna, a fan beam antenna and an antenna developed in this project. In all cases an omni directional antenna was used as a transmitter. In addition the measurements were performed in two different scenario's one with a direct path and one without a direct path. The measured bandwidth was 2 GHz ranging from 58 till 60 GHz and the measurement time was 100 ns.
The received power at 60 GHz was 2.4 to 7.7 dB lower in the case of the NLOS situation than the power received at the same frequency in the LOS situation. The mean power in the frequency band 58 - 60 GHz in the NLOS situation was 1.5 to 5.7 dB lower than the power received in the same band in the LOS situation. The fan beam antenna had the highest received power followed by the omni directional and bow-tie slot antenna. The omni directional antenna had the highest increase in path loss when there was no direct path, followed by the fan beam antenna and the bow-tie slot antenna.
The mean delay spread and RMS delay spread have been measured. The results of these measurements are given in Table 8.5. The lowest RMS delay spread was found when using the fan beam antenna as receive antenna. The highest RMS delay spread was found for the bow-tie slot antenna. For all antenna types the RMS delay spread was higher in the NLOS situation than in the LOS situation.
The coherence bandwidth was calculated using two different approaches. The first approach directly determines the correlation factor in the frequency domain. The second approach is an approximation based on the RMS delay spread in the time domain. The second approach was preferred because the resolution in the frequency domain was too low to calculate an accurate value. The coherence bandwidth has the inverse behavior of the RMS delay spread.

The small-scale measurement data was used to find the statistical distribution of the absolute value and phase of the received signal. A Ricean distribution was fitted to the measured absolute value of the received signal. The Ricean k-factor of measurements M1 to M6 was determined. The k-factor of the fan beam antenna was lower in the NLOS situation than in the LOS situation. When using the bow-tie slot and omni directional antennas the k-factor was higher in the NLOS situation than for the LOS situation.

The 60 GHz measurements have been performed only in one room. This limits the usability of the obtained results. For a full understanding of the small-scale behavior of the 60 GHz indoor radio channel it is necessary to perform more measurements at different locations. Although three different antenna types have been used no investigation was done on the parameters of the channel when the antennas were not placed at equal heights or when there is a misalignment between the antennas.

This project has focused mainly on the time of arrival parameters and statistical distribution functions. In Chapter 6 it was shown that the bow-tie slot antenna has a simulated gain of 2.6 dBi. It is assumed that this gain is too low. A possible solution could be the use of an array of bow-tie antennas. In order to design a good antenna array the direction of arrival of the electromagnetic waves has to be known. This was not investigated in this project. However the small-scale measurements could be used as a virtual array. In this virtual array the data points in the XY plane are treated as individual antennas. This can be done because the channel was stationary during the measurement.

Chapter 9

Conclusions and recommendations

The advancement of silicon IC processes opens up new opportunities to develop new consumer microwave applications at frequencies which were considered to high in the past. In this project a research in to the properties of transmission lines and antennas at high frequencies 24 GHz and 60 GHz has been performed. In addition the small-scale properties of an indoor radio channel at 60 GHz have been investigated. In this chapter the conclusions of this project are presented.

9.1 Conclusions concerning the antennas

Two new microwave applications have been investigated. The first application is an automotive radar system operating at 24 GHz which provides safety features and a parking aid. A bandwidth of at least 5 GHz is needed to achieve a range resolution of 6 cm needed for the parking aid. A required antenna gain of at least 6.5 dBi was found in a link budget investigation. The second application is a high speed wireless PAN system operating at 60 GHz. The main requirement placed on the antenna for this system is a bandwidth of at least 5 GHz. The dimensions of the antennas were restricted for both applications since it should be possible to integrate the antenna with the circuits in a small module.
Transmission lines play a key role in the design of antennas. Moreover the design of transmission lines becomes more important at high frequencies. The propagation constant, attenuation factor and characteristic impedance of the microstrip line and the coplanar waveguide have been determined. Frequency dependent models were implemented in Matlab and simulations in ADS Momentum were performed. The models and simulations showed that the transmission line parameters have a strong frequency dependence. A microstrip line with W = 700 μm was found to have a characteristic impedance of 51 Ω, an attenuation of 52 dB/m and an effective permittivity of 3.2. The coplanar waveguide with dimensions W = 500 μm and G = 75 μm has a a characteristic impedance of 50 Ω, an attenuation of 44 dB/m and an effective permittivity of 2.1. These results are calculated using the models implemented in Matlab. The outcome of a comparison between the microstrip line and the coplanar waveguide was a higher degree of freedom in design and the possibility of a lower attenuation factor for the coplanar waveguide. A transition element for coplanar waveguides was designed. Simulations based on a cascaded transmission line model and simulations in ADS momentum showed that the transition element was well matched to the coplanar waveguides.

Prior to the antenna design a pre-selection was performed in a literature search in to wide bandwidth antenna designs. Four of the pre-selected designs were based on the microstrip patch

antenna design. These designs were chosen as a starting point based on the ease with which these antennas can be designed. During simulations with these antennas no wide bandwidth could be achieved. The main reason is the relatively high permittivity and small thickness of the used substrate. Typically antennas based on the microstrip patch antenna achieved bandwidths of 1.2 GHz for a single patch to 2.16 GHz for a double stacked patch. One design was found which had a bandwidth of 5.2 GHz. However a suitable feeding structure was not found.
Designs with a slot in a metal ground plane were investigated next. Two types have been investigated a bow-tie shaped slot antenna with a metal stub called the bow-tie slot antenna and a tapered slot antenna which is a planar variant of a horn antenna. These antennas were selected for fabrication based on the simulated bandwidth which met the requirement.
An experimental model for the tapered slot antenna was tested. The tsa was modelled as a cascade of coplanar waveguide sections and terminated with the resistance of free space. The transmission line parameters were then determined for each section and all the selections were recombined. However the termination with the resistance of free space was incorrect and the model was inaccurate.
A simulated bandwidth of 8.1 GHz and a measured bandwidth of 14.8 GHz were found for the tsa. The bow-tie slot antenna had a simulated bandwidth of 14.8 GHz and a measured bandwidth of 19.0 GHz. A simulated bandwidth of 17.2 GHz was found for the bow-tie slot antenna at 60 GHz, the measured bandwidth was 20.5 GHz. An attenuation of 35 dB at an elevation angle of 30° above the horizon was required for the antennas operating at 24 GHz. This requirement was not met by the bow-tie slot antenna at 24 GHz and the tapered slot antenna.
The bow-tie slot antenna for 24 GHz had a gain of 4.5 - 5.9 dBi which is comparable to the simulated gain of 4.7 dBi. The measured gain of the TSA is 5.3 - 7.0 dBi which is higher than the simulated gain of 3.4 dBi. The bow-tie slot antenna at 24 GHz does not meet the gain requirement. In the case of the tsa the gain requirement was met in only one measurement in other measurements the gain was too low. The measurement of the gain of the bow-tie slot antenna for 60 GHz failed. The simulated gain of this antenna is 2.7 dBi.
An important conclusion of the investigation of the antennas is that the bandwidth requirements can not be met by designs based on a microstrip patch but can be met by designs based on a slot in a metal ground plane.

9.2 Conclusions concerning indoor radio channels

The indoor radio channel at 60 GHz was measured using a setup in which the receiving antenna could be displaced with steps of one tenth of a wavelength in order to obtain the small-scale characteristics. A total of eight small-scale radio channel measurements has been performed. Three different types of antennas have been used, an omni directional antenna, a fan beam antenna and the bow-tie slot antenna for 60 GHz developed in this project. In all cases an omni directional antenna was used as a transmitter. In addition the measurements were performed in two different scenario's one with a direct path and one in which the direct path was blocked. The measured bandwidth was 2 GHz ranging from 58 till 60 GHz.
The received power at 60 GHz was 2.4 to 7.7 dB lower in the case of the NLOS situation than the power received at the same frequency in the LOS situation. The mean power in the frequency band 58 - 60 GHz in the NLOS situation was 1.5 to 5.7 dB lower than the power received in the same band in the LOS situation. The fan beam antenna had the highest received power followed by the omni directional antenna and bow-tie slot antenna. The omni directional antenna had the

highest decrease in received power path loss when there was no direct path, followed by the fan beam antenna and the bow-tie slot antenna.
The mean delay spread and RMS delay spread have been measured. The lowest RMS delay spread was found when using the fan beam antenna as receive antenna and was 7 ns in the LOS situation and 11 ns in the NLOS situation. The highest RMS delay spread was found for the bow-tie slot antenna and was 12 ns in the LOS and 13 ns in the NLOS situation. The RMS delay spread of the omni directional antenna was 8 ns for the LOS and 10 ns for the NLOS situation. For all antenna types the RMS delay spread was higher in the NLOS situation than in the LOS situation.
The coherence bandwidth was calculated using two different approaches. The first approach directly determines the correlation factor in the frequency domain. The second approach is an approximation based on the RMS delay spread in the time domain. The second approach was preferred because the resolution in the frequency domain was too low to calculate an accurate value.
The small-scale measurement data was used to find the statistical distribution of the absolute value and phase of the received signal. A Ricean distribution was fitted to the measured absolute value of the received signal. The Ricean k-factor of the fan beam antenna was lower in the NLOS situation 1.8, than in the LOS situation 2.2. When using the bow-tie slot and omni directional antennas the k-factor was higher in the NLOS situation 1.3 and 1.8 respectively, than for the LOS situation 0.88 and 0.89 respectively. The uniform distribution could only be fitted to the phase of the received signal in the NLOS situation when the omni directional antenna was used as receive antenna. In all other measurement a strong peak around 180° was present.

9.3 Recommendations

The results presented in this report show that the bandwidth requirement of 5 GHz can be met. However the requirements placed on the gain and the gain at a specified elevation angle were not met. The gain of the tapered slot antenna could be increased by increasing the length of the slots. However due to the limited space available this might not be possible. Another option is the use of an antenna array. In this case the radiation pattern of the individual antennas is multiplied by an array factor. The possibility exists that by configuring the array in a specific way the gain at the 30° elevation angle can be suppressed. In addition the overall gain of an array is larger than the gain of the individual antenna elements.
The accuracy of the results presented in this report was limited by ADS. At several points in this project problems arose whenever a slot in a metal plane with finite thickness had to be simulated. For example with the coplanar waveguide and the slot antennas. During this project an upgrade of ADS became available which models the finite thickness of metal layers more accurately by calculating the horizontal currents on the sides of a thick conductor. However the modelling of thick metal layers remains a problem in ADS due to the large amount of memory that this method requires. If in a future project simulations of slot antennas in an array will be performed the amount of memory that is currently available will not be sufficient. Considering this observation a full three dimensional or another two dimensional simulator which has more memory at its disposal might out-perform ADS when investigating the performance of slot antenna arrays.
The 60 GHz measurements have been performed only in one room. This limits the usability of the obtained results. For a full understanding of the 60 GHz indoor radio channel it is necessary to perform more measurements at different locations. Although three different antenna types have been used no investigation was done on the parameters of the channel when the antennas

were misaligned .
This project has focused mainly on the time of arrival parameters and statistical distribution functions. In order to design a good antenna array the direction of arrival of the electromagnetic waves has to be known. This was not investigated in this project. However the small-scale measurements could be used as a virtual array. In this virtual array the data points in the XY plane are treated as individual antennas. This can be done because the channel was stationary during the measurement. The data obtained with the virtual array could then be further processed to obtain the angle of arrival.

Acknowledgment

I would like to thank Philips Research Eindhoven for giving me the opportunity to perform my graduation project at Philips Research Eindhoven. Furthermore I would like to thank Dr. ir. G. Dolmans, Dr. ir. P.F.M. Smulders and Dr. ir. M.H.A.J. Herben for their supervision and help during my graduation project.

I also would like to thank all members and colleagues within the Integrated Transceivers Group, my family and my friends for their continuous support and interest in my project.

Feike Jansen, June 2006

References

[1] R. Schneider J. Wenger K.l M. Strohm, H-L Bloecher. Development of Future Short Range Radar Technology. In *Second European Radar Conference, Paris*, pages 165–168, October 2005.

[2] I. Gresham and C. Eswarappa N. Kinayman N. Jain R. Anderson F. Kolak R. Wohlert S. P. Bawell J. Bennett J-P Lanter A. Jenkins, R. Egri. Ultra-Wideband Radar Sensors for Short-Range Vehicular Applications. *IEEE Transactions on Microwave Theory and Techniques*, 52(9):2105 – 2122, September 2004.

[3] O. A. M. Omar and A. S. Omar. New Implementation of the Correlation Function of the PN Code for Application in Automotive Radars. In *In proceedings of the International IEEE Antennas and Propagation Society Symposium, 2003.*, volume 3, pages 272 – 275, 22-27 June 2003.

[4] M.N.O. Sadiku. *Elements of electromagnetics.* Oxford University Press, Oxford, third edition, 2001.

[5] K.C. Gupta R. Garg I. Bahl P. Bhartia. *Microstrip Lines and Slotlines.* Artech House Boston, second edition, 1996.

[6] G. Kumar K.P. Ray. *Broadband Microstrip Antennas.* Artech House, Boston, 2003.

[7] L. I. Basilio M. A. Khayat J. T. Williams S. A. Long. The Dependence of the Input Impedance on Feed Position of Probe and Microstrip Line-Fed Patch Antennas. *IEEE Transactions on Antennas and Propagation*, 49(1):45–47, January 2001.

[8] R.B. Waterhouse. Desing of Probe-Fed Stacked Patches. *IEEE Transactions on Antennas and Propagation*, 47(12):1780–1784, December 1999.

[9] T. Huynh K. F. Lee. Single-Layer Single-Patch Wideband Microstrip Antenna. *IEEE Transactions on Antennas and Propagation*, 31(3):1310–1312, August 1995.

[10] P. J. Gibson. The Vivaldi Aerial. In *Proceedings of the 9th European Microwave conference*, September 1979.

[11] S. Mahapatra. A novel MIC slot-line antenna. In *Proceeding of the 9th European Microwave conference*, pages 120–123, September 1979.

[12] K. S. Yngvesson T. L. Korzeniowski Y. S. Kim E. L. Kollberg J. F. Johansson. The Tapered Slot Antenna-A New Integrated Element for Millimeter-Wave Applications. *IEEE Transactions on Microwave Theory and Techniques*, 37(2):365–374, 1989.

[13] R. N. Simons N. I. Dib R.Q. Lee L. P. B. Katehi. Integrated Uniplanar Transistion for Linearly Tapered Slot Antenna. *IEEE Transactions on Antennas and Propagation*, 43(9):998–1002, September 1995.

[14] R. Janaswamy D. H. Schaubert. Analysis of the Tapered Slot Antenna. *IEEE Transactions on Antennas and Propagation*, 35(9):1058–1064, 1987.

[15] H Y Wang S. D. Mirshekar-Syakhal I. J. Dilworth. A Rigorous Analysis of Tapered Slot Antennas on Dielectric Substrates. In *Proceedings of the 10th International Conference on Antennas and Propagation*, April 1997.

[16] H Y Wang D. Mirshekar-Syakhal I. J. Dilworth. Numerical Modeling of V-Shaped Linearly Tapered Slot Antennas. In *Proceedings of the Antennas and Propagation Society International Symposium*, volume 2, pages 1118–1121, July 1997.

[17] H. Oraizi S. Jam. Optimum Design of the Tapered Slot Antenna Profile. *IEEE Transactions on Antennas and Propagation*, 51(8):19871995, August 2003.

[18] K. S. Yngvesson D. H. Schaubert T. L. Korzeniowski E. L. Kollberg T. Thungren J. F. Johansson. Endfire Tapered Slot Antennas on Dielectric Substrates. *IEEE Transactions on Antennas and Propagation*, 33(12):1392–1400, December 1985.

[19] B.L. Ooi M. Miao and P.S. Kooi. Broadband CPW-fed wide slot antenna. *Microwave and Optical Technology Letters*, 25(3):583–588, May 2000.

[20] A. A. Eldek A. Z. Elsherbeni C. E. Smith. Wideband Bow-tie Slot Antenna With Tuning Stub. In *Proceeding of the IEEE, Radar Conference 2004*, 26-29 April 2004.

[21] H. Yang and M.H.A.J. Herben P.F.M. Smulders. Channel Characteristics and Transmission Performance for Various Channel Configurations at 60 GHz. *to be published in: special issue of EURASIP on millimeter-wave wireless communication systems: theory and application*, 2007.

[22] T. S. Rappaport. *Wireless communications: principles and practice*, volume two. Upper Saddle River, Prentice Hall PTR, 2002.

[23] L. Leijten. *Design of Antenna-Diversity Transceivers*. Koninklijke Philips Electronics N.V., 2001.

[24] J. Schonthier. WP3-Study The 60 GHz Channel and its Modelling. Technical report, BroadWay, May 2005.

[25] F. Di Paolo. *Networks and Devices Using Planar Transmission Lines*. CRC Press, Boca Raton, 2000.

[26] M. M. Ney. Method of Moments as Applied to Electromagnetic Problems. *IEEE Transactions on Microwave Theory and Techniques*, 33(10):972–980, October 1985.

[27] Y. Eo and W.R. Eisenstadt. High-Speed VLSI Interconnect Modeling Based on S-Parameter Measurements. *IEEE Transactions On Components, Hybrids and Manufacturing Technology*, 16(5), 1993.

[28] K. Narita T.Kushta. An Accurate Experimental Method for Characterizing Transmission Lines Embedded in Mulitlayer Printed Circuit Boards. *IEEE Transactions on Advanced Packaging*, 29(1):114–120, February 2006.

Appendix A

Transmission line equations

In this appendix the general equations that describe transmission lines will be treated. They serve as a basis for the models treated in Chapter 4. It is assumed that all the transmission lines, used in this project, attenuate the signal. Such lines are called lossy transmission lines. Three parameters: the characteristic impedance Z_0, the phase constant β, and the attenuation factor α, are used to describe the lossy transmission lines. A lossy transmission line can be represented by the L-type lumped circuit depicted in Figure A.1. The components are given per unit length. By

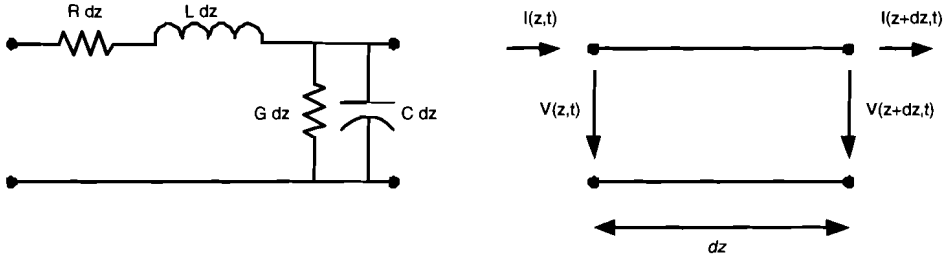

Figure A.1: L-type equivalent lumped circuit of a lossy transmission line for a differential length Δz.

applying Kirchhoff's voltage and current laws to the lumped circuit, with a length $\Delta z \rightarrow 0$ and taking the derivative of the voltage and current, a set of equations for the voltage, $V(z)$ and the current, $I(z)$, in the transmission line is obtained, see reference [4].

$$V(z,t) = R\Delta z I(z,t) + L\Delta z \frac{\delta I(z,t)}{\delta t} + V(z+\Delta z,t) \quad \text{(A.1)}$$

$$I(z,t) = I(z+\Delta z,t) + G\Delta z V(z+\Delta z,t) + C\Delta z \frac{\delta V(z+\Delta z,t)}{\delta t} \quad \text{(A.2)}$$

$$\frac{V(z,t)-V(z+\Delta z,t)}{\Delta z} = RI(z,t) + L\frac{\delta I(z,t)}{\delta t} \quad \text{(A.3)}$$

$$\frac{I(z,t)-I(z+\Delta z,t)}{\Delta z} = GV(z+\Delta z,t) + C\frac{\delta V(z+\Delta z,t)}{\delta t} \quad \text{(A.4)}$$

By assuming harmonic time dependence with $\omega = 2\pi f$:

$$V(z,t) = Re[V_s(z)e^{j\omega t}] \quad \text{(A.5)}$$

$$I(z,t) = Re[I_s(z)e^{j\omega t}] \quad \text{(A.6)}$$

Taking another derivative of A.4 and A.3 and filling in the term for $I(z,t)$ obtained in Equation A.4 into the derivative of Equation A.3 and filling in the term for $V(z,t)$ obtained in Equation A.3 into the derivative of Equation A.4 the following differential equations are obtained:

$$\frac{d^2V_s(z)}{dz^2} - \gamma^2 V_s(z) = 0 \tag{A.7}$$

$$\frac{d^2I_s(z)}{dz^2} - \gamma^2 I_s(z) = 0 \tag{A.8}$$

The solution for the voltage V_s is given by:

$$V_s(z) = V_0^+ e^{-\gamma z} + V_0^- e^{\gamma z} \tag{A.9}$$

The solution for the current I_s is given by:

$$I_s(z) = I_0^+ e^{-\gamma z} + I_0^- e^{\gamma z} \tag{A.10}$$

where V_0^+, V_0^-, I_0^+ and I_0^- are wave amplitudes, the + and - signs, respectively denote the wave travelling along the $+z$ and $-z$ directions. If an infinitely long transmission line is assumed the waves travelling along the $-z$ direction can be assumed zero. The voltage and current can now be given by:

$$V_s(z) = V_0^+ e^{-\gamma z} \tag{A.11}$$

$$I_s(z) = I_0^+ e^{-\gamma z} \tag{A.12}$$

The derivatives of equations A.3 and A.4 can now be written as:

$$-\gamma V_0^+ = RI_0^+ + j\omega L I_0^+ \tag{A.13}$$

$$-\gamma I_0^+ = GV_0^+ + j\omega C V_0^+ \tag{A.14}$$

where γ can be obtained by substituting the result of Equation A.14 in to Equation A.13:

$$\begin{aligned} -\gamma V_0^+ &= (R + j\omega L) I_0^+ \\ -\gamma V_0^+ &= (R + j\omega L)(GV_0^+ + j\omega C V_0^+)/-\gamma \\ \gamma^2 &= (R + j\omega L)(G + j\omega C) \\ \gamma &= \sqrt{(R + j\omega L)(G + j\omega C)} = \alpha + j\beta \end{aligned} \tag{A.15}$$

In transmission line theory, γ is called the propagation constant, α is the attenuation factor (dBm^{-1}) and β is the phase constant ($radm^{-1}$). β can be seen as the spatial equivalent of the frequency. β and α can be represented by the following equations taken from reference [25]:

$$\alpha = \sqrt{RG - \omega^2 LC + \sqrt{(RG - \omega^2 LC)^2 + \omega^2 (RC + LG)^2}}/\sqrt{2} \tag{A.16}$$

$$\beta = \sqrt{\omega^2 LC - RG + \sqrt{(RG - \omega^2 LC)^2 + \omega^2 (RC + LG)^2}}/\sqrt{2} \tag{A.17}$$

By dividing the positively travelling voltage wave, from Equation A.13, by the current given in Equation A.14, at any point on the line the characteristic impedance of the transmission line is obtained as:

$$Z_0 = \frac{V_0^+}{I_0^+} = \frac{V_0^-}{I_0^-} \tag{A.18}$$

$$Z_0 = \sqrt{\frac{R + j\omega L}{G + j\omega C}} = R_0 + jX_0 \tag{A.19}$$

Appendix B

Electromagnetic modelling

Antenna designs are structures for which the full wave analysis can be difficult. The analytical analysis of the antennas treated in this report is beyond the scope of the project. To be able to evaluate and design the antennas extensive use has been made of computer aided design programs. This has proved to be very helpful in designing antennas since the performance of the antenna could be evaluated without knowledge of the, sometimes complicated, principles of operation. There are several methods to solve the three dimensional full wave problems of antenna design. These methods are based on the electric current distribution on the metal surfaces in conjunction with full wave numerical analysis. The following numerical methods are frequently used: the finite-element method, the finite-difference time domain method and the method of moments.
In this project Advanced Design System from Agilent has been used. This program contains the Momentum engine which is able to solve the currents in multi-layered two dimensional structures using the method of moments. Because extensive use has been made of this program the method of moments as used in Momentum will be treated in detail in this appendix. This method can be seen as a 2,5 dimensional method, it uses the surface currents in a planar metal structure in conjunction with the polarization currents in the dielectric substrates between the metal layers to model the electromagnetic fields. An integral equation for the unknown currents on the metal surfaces is formulated. This integral equation is discretizised in order to solve the resulting problem numerically. The electromagnetic fields are then derived from the obtained currents on the metal surfaces and the polarization currents in the dielectric substrate. With the method of moments equations of the following type of equation can be solved:

$$\int_S \int G(\mathbf{r},\mathbf{r}') * J(\mathbf{r}) dS = E(\mathbf{r}) \tag{B.1}$$

where $J(\mathbf{r})$ represents the unknown surface currents, on the corresponding surface S and $E(\mathbf{r})$ represents the known excitation. $G(\mathbf{r},\mathbf{r}')$ is the integral kernel and is a suitable Green function which will be treated further on and $*$ represents the inner product. The surface current is meshed in a two dimensional plane, see Figure B.1 and expanded in sub sectional basis functions.

$$J(\mathbf{r}) = \sum_{j=1}^{N} I_j B_j(\mathbf{r}) \tag{B.2}$$

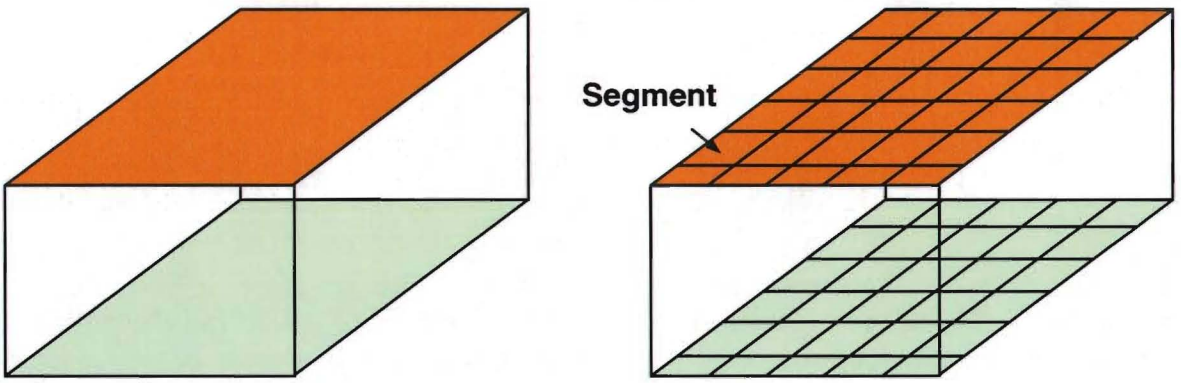

Figure B.1: A simple structure with two conductors separated by a dielectric substrate [left], the structure with the mesh applied [right]

where I_j are constants. Each basis function, $B_j(\mathbf{r})$, represents a constant density current flowing through one edge of the two dimensional cell, see Figure B.2. The mesh can be either rectangular, triangular or polygonal, depending on the geometry of the structure. The basis functions, used in Momentum, are the so-called rooftop functions. In these functions each rooftop represents a current with constant density flowing through that edge. After expanding the surface current into basis functions the equation given in Equation B.1 can now be written as:

$$\sum_{j=1}^{N} I_j \int_S \int G(\mathbf{r},\mathbf{r}') * B_j(\mathbf{r}) dS = E(\mathbf{r}) \tag{B.3}$$

There are N unknown constants I_j and only one equation. Consequently the unknown constants cannot be determined directly. Therefore a set of trial weighting functions $w_j(\mathbf{r}) = w_1(\mathbf{r}), w_2(\mathbf{r}), ..., w_N(\mathbf{r})$ is introduced see reference [26]. The error between the result of the trial function and the true result can be obtained by taking the inner product, between the trial and the true solution. The error function is given by:

$$\sum_{j=1}^{N} I_j \int_S \int w_j dS * \int_S \int G(\mathbf{r},\mathbf{r}') * B_j(\mathbf{r}) dS = \int_S \int w_j * E(\mathbf{r}) dS \tag{B.4}$$

The true solution can be obtained by applying the testing procedure to the boundary conditions where the fields are known. The weights can now be found be iteratively searching for the weights that obey the boundary conditions. In Momentum the Galerkin testing procedure is applied. This means that the weighting functions $w_j(\mathbf{r})$ are equal to the basis functions $B_j(\mathbf{r})$. The equation described in Equation B.4 is transformed into:

$$\text{for } i = 1, ...N$$
$$\sum_{j=1}^{N} Z_{i,j} I_j = V_i \qquad \text{or} \qquad [Z] * [I] = [V] \tag{B.5}$$

with

$$Z_{i,j} = \int_S \int B_i(\mathbf{r})dS * \int_S \int G(\mathbf{r},\mathbf{r}') * B_j(\mathbf{r})dS \tag{B.6}$$

$$V_i = \int_S \int B_i(\mathbf{r}) * E(\mathbf{r})dS \tag{B.7}$$

The matrix $[Z]$ is the interaction matrix since it describes the electromagnetic interaction between each of the rooftop basis functions. Therefore the dimension of $[Z]$ is N. The elements $[Z_{i,j}]$ represent the interaction between the i^{th} and j^{th} cell. The vector $[V]$ represents the voltage source which forms the excitation of the structure.
The surface currents excite an electromagnetic field in the circuit. These currents are described using dyadic Green's functions of the dielectric substrate. These are obtained via the impulse response between each pair of layers, dielectric substrate and conductors and thus form a spatial impulse response. In ADS the Green's functions are pre-computed for a specific substrate stack. In this way the Green's functions are known for each circuit that uses this specific substrate stack. ADS uses the mixed potential integral equation. This formulation expresses the electric and magnetic currents as a vector and a scalar potential. The Green function $G(\mathbf{r},\mathbf{r}')$, is given by:

$$G(\mathbf{r},\mathbf{r}') = j\omega G^A(\mathbf{r},\mathbf{r}')I - \frac{1}{j\omega}\nabla[G^V(\mathbf{r},\mathbf{r}')\nabla'] \tag{B.8}$$

where $G^A(\mathrm{r},\mathbf{r}')$ represents the vector potential at $\mathbf{r}$ due to a electric dipole of unit strength located at $\mathbf{r}'$ and $G^V(\mathbf{r},\mathbf{r}')$ represents the scalar potential at $\mathbf{r}$, due to a unit point charge associated with an electric dipole at $\mathbf{r}'$. The expression for $G(\mathbf{r},\mathbf{r}')$ obtained in Equation B.8, is substituted in Equation B.6.

$$Z_{i,j} = j\omega L_{i,j} + \frac{1}{j\omega C_{i,j}} \tag{B.9}$$

with

$$L_{i,j} = \int_S \int B_i(\mathbf{r})dS * \int_S \int G^A(\mathbf{r},\mathbf{r}')B_j(\mathbf{r})dS \tag{B.10}$$

$$\frac{1}{C_{i,j}} = \int_S \int \nabla \cdot B_i(\mathbf{r})dS * \int_S \int G^V(\mathbf{r},\mathbf{r}')\nabla * B_j(\mathbf{r})dS \tag{B.11}$$

Now the meshed structure can be converted into a structure which consists of nodes. Where each node represents a segment of the meshed structure and the connections between the nodes are formed by the inductors, $L_{i,j}$ given in Equation B.11. All the nodes are connected to ground via a capacitor, $C_{i,j}$ given in Equation B.11, see Figure B.2. The ground in this case corresponds to the potential of an infinite metal layer or to a sphere at infinity.

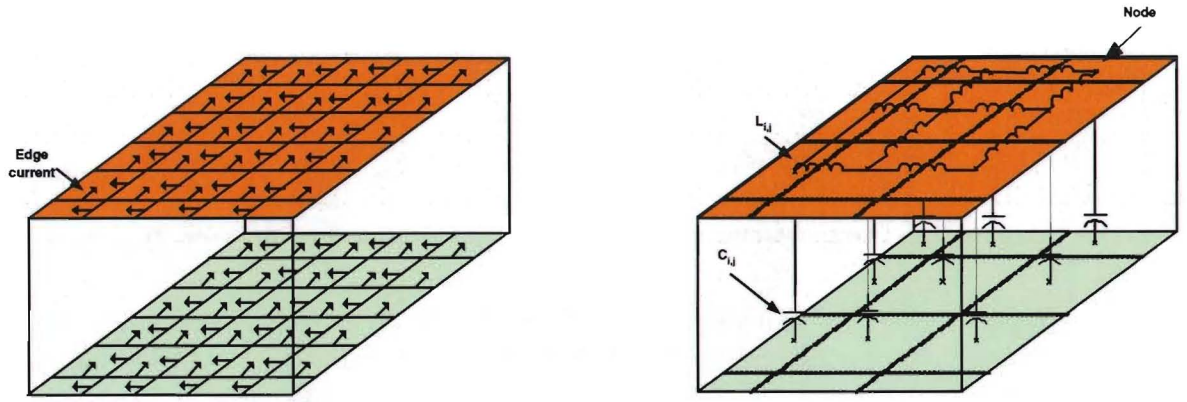

Figure B.2: The currents in the structure [left], equivalent circuit [right], for clarity the number of segments in the mesh has been reduced.

To excite the circuits ports are connected to metal layers. Different types of ports are available depending on the problem. The single port is calibrated and is connected to the edge of a conductor. Polarity can be assigned to a single port. The coplanar port is a variant of the single ports. It is a pair of ports with opposite polarity which are defined on slots. The internal port is not calibrated and is connected on the conductors. When using this type of port the circuit is excited with a lumped source. The last port that is used is the ground reference. This port is used to connect conductors to ground when there is no ground plane present in the structure.
Although ADS is only capable of simulating planar structures, the finite thickness of metal layers can still be taken into account. The mask of a conductor is expanded with finite thickness in the direction orthogonal to the conducting layer. Therefore an extra dielectric layer is included with the characteristics of the material above or below the conducting layer. The thickness of the dielectric substrate between two conducting layers is however not changed. In case this option in ADS is not used all metal layers are modelled as metal sheets with zero thickness and a resistivity. This resistivity is calculated from the assigned metal thickness and the real part of sigma, σ. When the metal conductors are modelled as sheets the metal surfaces orthogonal to the metal layer are removed. This can effect the simulated results. When simulations are performed on structures containing a slot in a ground plane and the metals are modelled as sheets the capacitance is underestimated.
Up to now only currents on metal surfaces have been considered. The antenna designs that have been discussed use a slot in a metal surface. This case is treated differently by Momentum. The equivalence theorem is applied. The electric field in the slot is modelled as an equivalent magnetic current. This prevents the calculation of the electric currents in the large ground plane surrounding the slot.
Now that the excitation is known the currents on the surfaces can be found by applying the Kirchhoff's voltage laws to the equivalent network. The obtained currents in the structure are then used to calculate the electromagnetic field. In ADS only the far field components are considered. These components vary with $1/r$ where r is the distance between the antenna and the point of observation. The following antenna characteristics were used to analyse the antennas: gain, directivity, efficiency and polarization. In addition to these parameters the radiation patterns were also analyzed. These patterns were obtained by cutting the radiation pattern along the θ or ϕ axis, see Figure B.3. The directivity is obtained by dividing the radiation intensity in one direction by

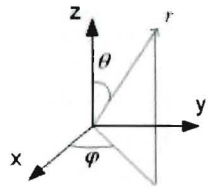

Figure B.3: The coordinate system used for the antenna radiation pattern.

the total radiated power. In ADS the maximum directivity is given in addition the angle at which the directivity reaches it's maximum is also given. The antenna gain is obtained by dividing the maximum radiation intensity by the total injected power. By dividing the gain by the directivity an efficiency parameter of the antenna can be obtained. The efficiency is a ratio of the amount of the power that is injected into the circuit, to the power that is radiated away from the circuit. The power that is not radiated is lost in surface waves and in losses in the conductors and dielectric substrate.

Appendix C

Extracting transmission line parameters from s-parameter data

The transmission lines treated in Chapter 4 are usually described by the characteristic impedance and propagation constant. These parameters provide an insight in the behavior of the transmission line. Models based on empirical data can be used to compute these parameters. In addition commercial CAD programs are often used to obtain the transmission line parameters. The results of the CAD programs and the implemented models were compared to the results obtained with ADS Momentum. At first the obtained results of ADS were not in the line of expectance. A large influence of the used configuration, i.e. thick or thin conductors, single or internal port, was found. Further research was performed to obtain the best configuration in ADS. The results of this research are presented in this appendix.

Two different ports have been connected to the transmission lines in ADS, the single port and the internal port. The single port is a calibrated port and calculates the propagation constant. The internal port is a non-calibrated port and does not calculate the propagation constant. Therefore the use of single ports when simulating transmission lines in ADS is an obvious choice. However ADS is not able to calibrate transmission lines with a finite thickness due to the model used to model transmission lines. To solve this problem internal ports were connected to the transmission lines and the propagation constant and characteristic impedance were derived from the obtained s-parameters. Two formulas can be used to extract these parameters from the s-parameters, see reference [27].

$$e^{-\gamma l} = \left[\frac{1 - S_{11}^2 + S_{21}^2}{2S_{21}} \pm K\right]^{-1} \tag{C.1}$$

$$K = \left[\frac{(S_{11}^2 - S_{21}^2 + 1)^2 - (2S_{11})^2}{(2S_{21})^2}\right]^{1/2} \tag{C.2}$$

where l is the length of the transmission line in meters. The characteristic impedance Z_0 can be obtained with:

$$Z_0^2 = Z_{ref}^2 \frac{Z_{de}}{Z_{num}} = Z_{ref}^2 \frac{(1 + S_{11})^2 - S_{21}^2}{(1 - S_{11})^2 - S_{21}^2} \tag{C.3}$$

Z_{ref} in this case is 50 Ω. However this approach is sensitive to numerical problems see for example Figure C.1. In this figure the impedance, obtained from the s-parameter data from ADS,

is depicted in red and the blue line is the squared value of Z_{de} in Equation C.3, multiplied by a constant and the green line is the squared value of Z_{num}, multiplied by a constant. In contrast to the empirical models the length of the line plays an important role. At frequencies where the line length is near a multiple of half-wave-length the squared value of Z_{de} and of Z_{num} approach zero and numerical uncertainties can become a problem. A good example of this problem can be

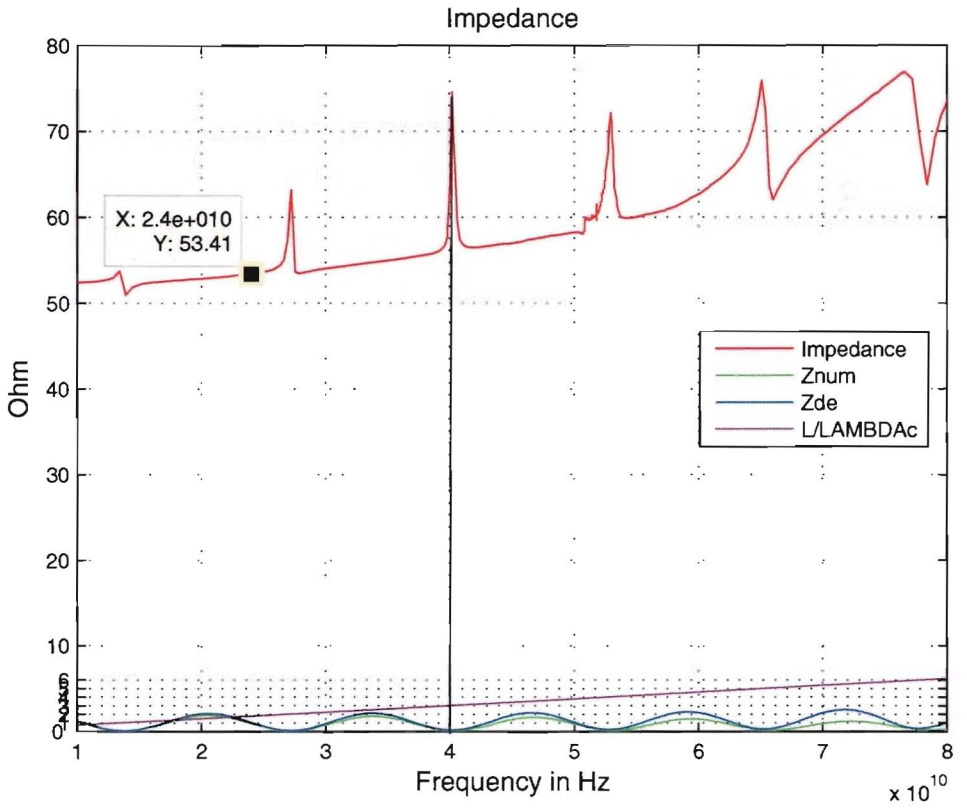

Figure C.1: The impedance of a microstrip line with $W = 700\mu m$, $h = 330\mu m$, $L = 6.2$ mm and $t = 28\mu m$ calculated using the formula described in C.3

seen at 40 GHz. At this frequency the half wave length multiplied by three is equal to the length of the microstrip. At 24 GHz the length of the microstrip line is not near a multiple of the half wave length. However if the length of the microstrip line would have been equal to a multiple of the half wave length at 24 GHz the data could not have been extracted in this way. The results of this approach are depicted in row 1a of Table C.1.

In row 1b of this Table the results of the build-in model of a microstrip line in ADS are depicted. In this case the thickness of the metal was set to zero (sheet conductor), and the line was excited with a single port. The difference in values can be explained by the difference in metal thickness. The values in row 1a compare well to the values given in Table 4.2, except for the attenuation factor which was lower.

The next two measurements were performed on a coplanar waveguide modelled as two slots in an infinite perfect conducting ground plane. The values were extracted directly from ADS by using calibrated ports. As can be seen there is no difference between a thin ground plane, row 2, or a thick ground plane, row 3. ADS underestimates the capacity by not modelling the thickness

of the conductors, this leads to a higher characteristic impedance. Because the ground plane is modelled as a perfect conductor no losses in the conductor have been taking into account which leads to a low value of the attenuation per meter.
To obtain an accurate estimation of the capacitance of the coplanar waveguide the metal thickness has to be taken into account. This is done by modelling the metal layers as three strips with a finite thickness and finite width. Three different approaches using this configuration were investigated. In the first method the configuration is excited by calibrated single ports and the transmission line parameters are computed by ADS. In the second method the s-parameters were extracted from ADS and converted to the transmission line parameters by equations: C.3 and C.1. In the third method two transmission lines of different length are used to remove the uncertainties that occur at frequencies where the length of the transmission line is a multiple of the half wave length.
The first method did not produce good results as can be seen in the Table C.1, row 4. The single port used in ADS is calibrated. The calibrating process uses a cross-section solver. However this solver is not capable of calculating transmission lines with thick conductors.
The second method was applied to a CPW with the strip configuration excited by internal, non calibrated, ports. The same numerical problems at frequencies where the length of the transmission line is a multiple of the half wave length arise. The problems were more severe than was the case with the microstrip line. No usable results were obtained with this method. An example of this problem is given in row 5.
The last method that was applied is a method presented in reference [28]. This method is based on a mathematical error removing scheme using two transmission lines of different length. By using two different length transmission lines the errors that occur when converting the s-parameters to transmission line parameters can be removed. This method was applied to the s-parameter data of the strip configuration excited by non calibrated ports. The lengths were chosen to be 6.2 mm and 6.3 mm. Two configurations were tested. The first configuration consists of three thick metal, conductors, row 6. The second configuration consists of three infinitely thin metal conductors, row 7.
In this appendix three methods were treated to obtain the transmission line parameters from ADS. In the case of a microstrip line these parameters can be obtained by converting the s-parameter data directly to the transmission line parameters. At the frequency of interest the length of the microstrip line may not be a integer multiple of the half wave length at that frequency.
The best method to obtain the transmission line parameters of the coplanar waveguide is to use a model which consists of three thick metal conductors. The configuration is best excited with an internal, non calibrated, port. The method described in [28] can then be applied. The results from this method are given in row 6 of Table C.1.

N	Type	Metal thick-ness	Port	Z_0	ϵ_r	β	α	description
1a	Micro strip line	thick	single	53.41 Ω	3.15	891.6 rad/m	41.48 dB/m	$W = 700\mu m$, $L = 6.2mm$, $h = 330\mu m$, $t = 25\mu m$
1b	Micro strip line	sheet	single	49.90 Ω	3.21	917.5 rad/m	53.99 dB/m	$W = 700\mu m$, $L = 6.2mm$, $h = 330\mu m$, $t = 0\mu m$
2	CPW slot	sheet	single	57.16 Ω	2.36	771.7 rad/m	30.84 dB/m	two slots, $W = 500\mu m$, $G = 75\mu m$, $L = 6.2mm$, $h = 330\mu m$, $t = 0\mu m$
3	CPW slot	thick	single	57.16 Ω	2.36	771.7 rad/m	30.84 dB/m	two slots, $W = 500\mu m$, $G = 75\mu m$, $L = 6.2mm$, $h = 330\mu m$, $t = 25\mu m$
4	CPW strip	sheet	single	132.43 Ω	1.53	622.64 rad/m	20.16 dB/m	Three strips, $W = 500\mu m$, $G = 75\mu m$, $L = 6.2mm$, $h = 330\mu m$, $t = 0\mu m$
5	CPW strip	thick	single	N.A. Ω	N.A.	N.A. rad/m	N.A. dB/m	Three strips, $W = 500\mu m$, $G = 75\mu m$, $L = 6.2mm$, $h = 330\mu m$, $t = 25\mu m$
6	CPW strip	thick	internal	52.21 Ω	2.00	710.0 rad/m	22.89 dB/m	Three strips, $W = 500\mu m$, $G = 75\mu m$, $L = 6.2mm$, $h = 330\mu m$, $t = 25\mu m$
7	CPW strip	sheet	internal	61.151 Ω	2.48	791.0 rad/m	41.42 dB/m	Three strips, $W = 500\mu m$, $G = 75\mu m$, $L = 6.2mm$, $h = 330\mu m$, $t = 0\mu m$

Table C.1: Summary of the transmission line parameters obtained using three different methods

Appendix D

Photo's

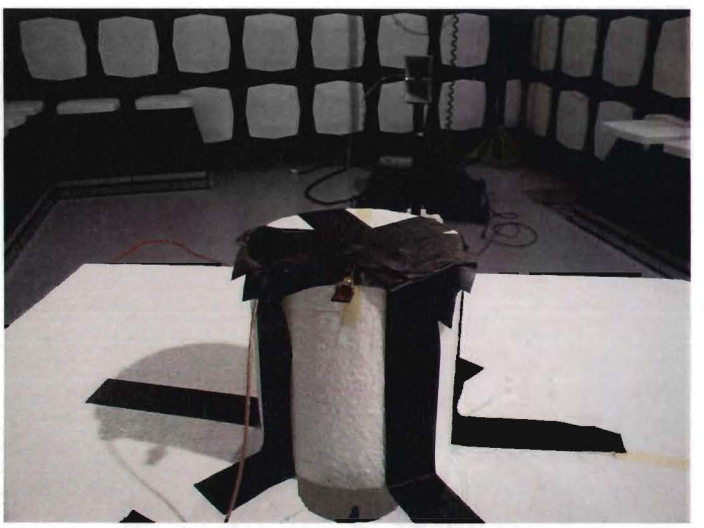

Figure D.1: Radiation pattern measurement with the antenna placed in the horizontal position.

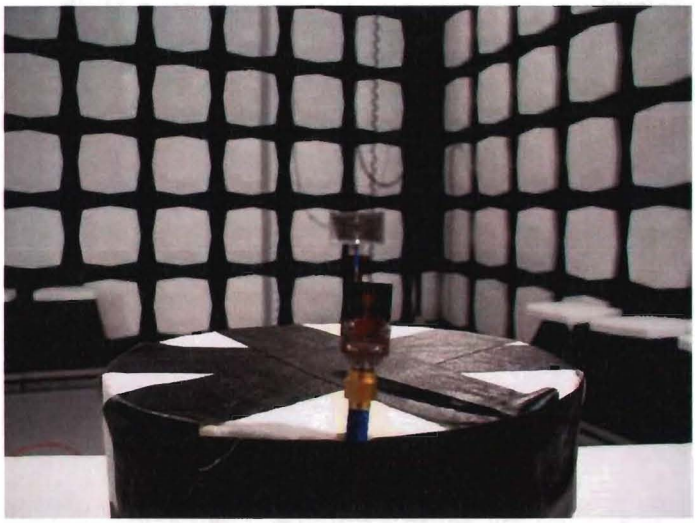

Figure D.2: Radiation pattern measurement with the antenna placed in the vertical position.

Appendix E

Small-scale indoor radio channels

Below some pictures of the measurement setup are included. In addition this appendix contains the results of the indoor small scale measurement that was performed at the Technical University of Eindhoven.

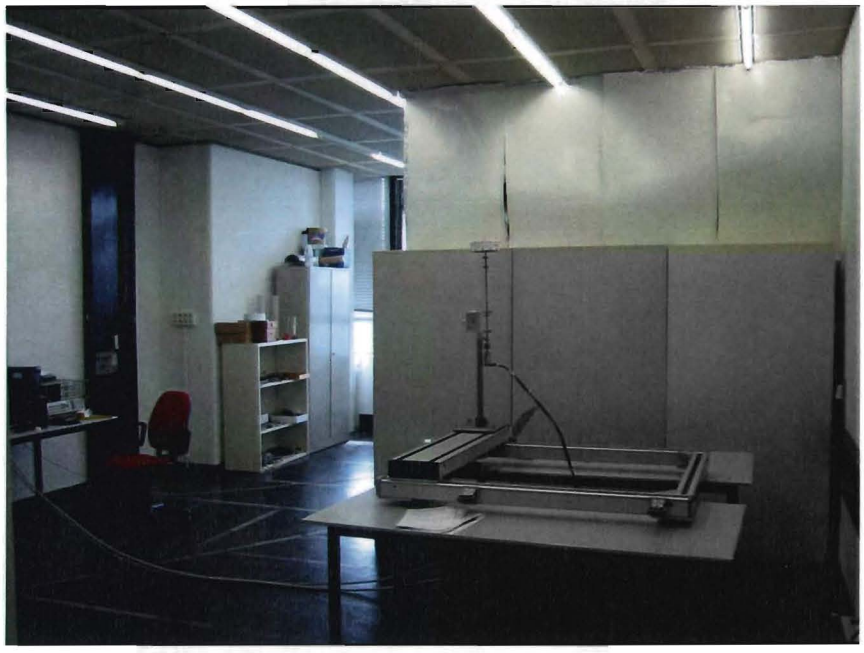

Figure E.1: The metal shield that was constructed to obtain a true non line of sight situation.

Figure E.2: The XY Table for the NLOS situation.

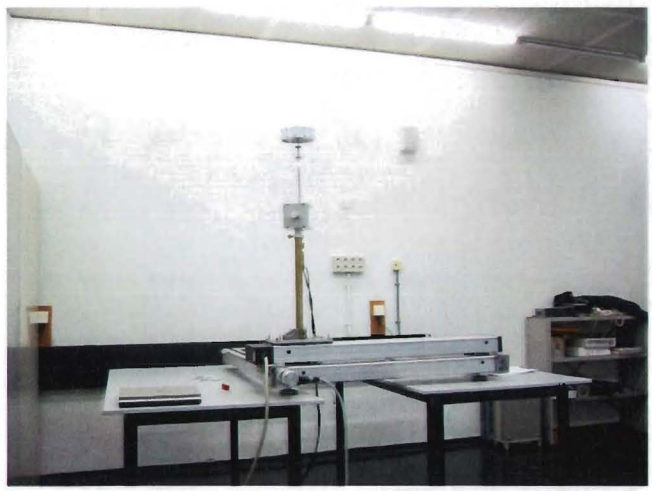

Figure E.3: Close up picture for the XY Table.

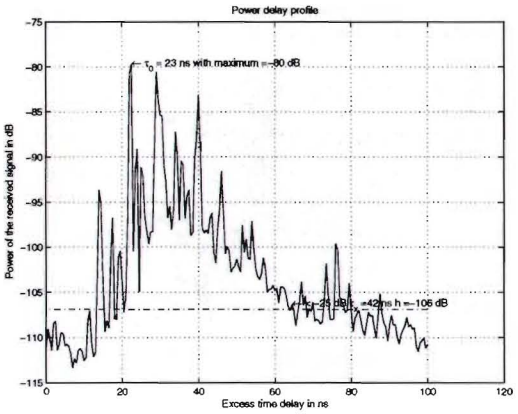

Figure E.4: Measurement M1: LOS path, Tx: Omni directional, Rx: Omni directional.

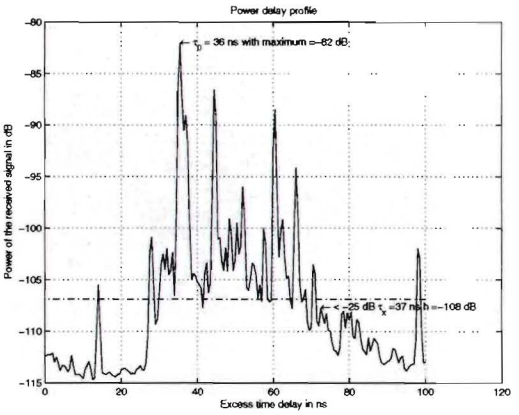

Figure E.5: Measurement M4: NLOS path, Tx: Omni directional, Rx: Omni directional.

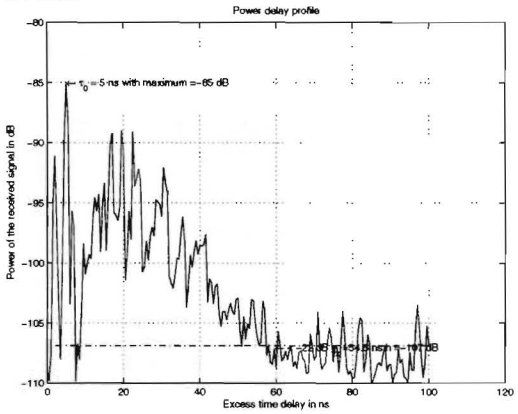

Figure E.6: Measurement M2: LOS path, Tx: Omni directional, Rx: Bow-Tie.

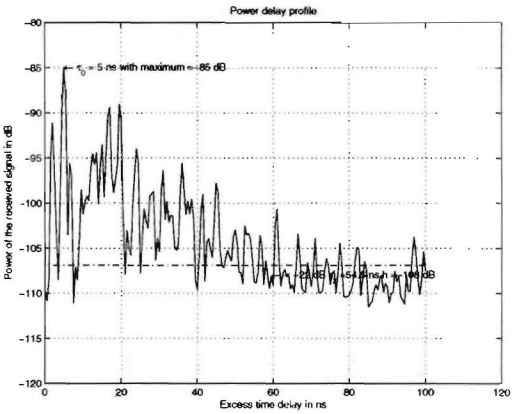

Figure E.7: Measurement M5: NLOS path, Tx: Omni directional, Rx: Bow-Tie.

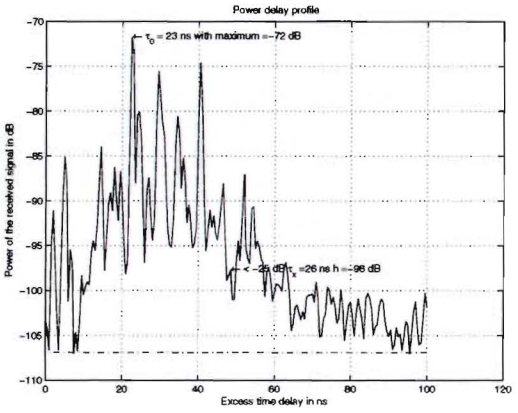

Figure E.8: Measurement M3: LOS path, Tx: Omni directional, Rx: Horn.

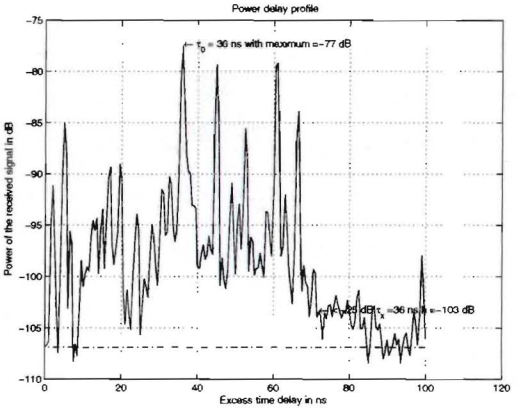

Figure E.9: Measurement M6: NLOS path, Tx: Omni directional, Rx: Horn.

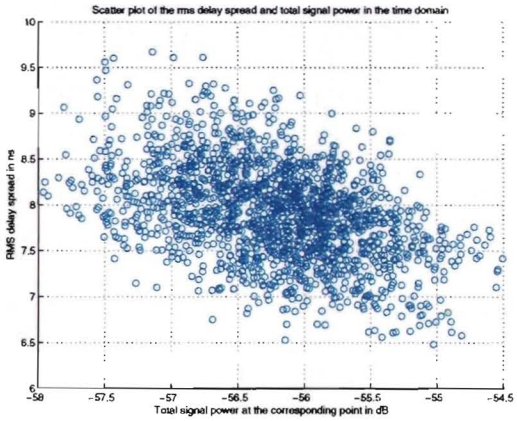

Figure E.10: Measurement M1: LOS path, Tx: Omni directional, Rx: Omni directional.

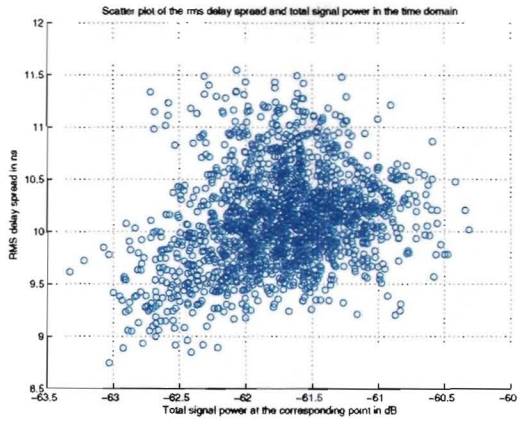

Figure E.11: Measurement M4: NLOS path, Tx: Omni directional, Rx: Omni directional.

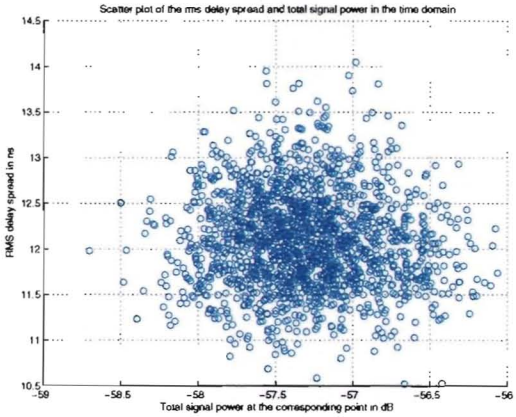

Figure E.12: Measurement M2: LOS path, Tx: Omni directional, Rx: Bow-Tie.

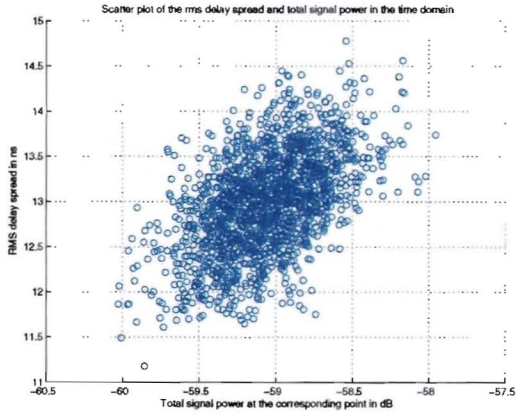

Figure E.13: Measurement M5: NLOS path, Tx: Omni directional, Rx: Bow-Tie.

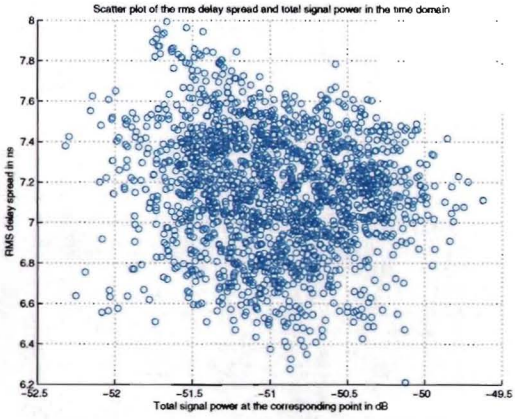

Figure E.14: Measurement M3: LOS path, Tx: Omni directional, Rx: Horn.

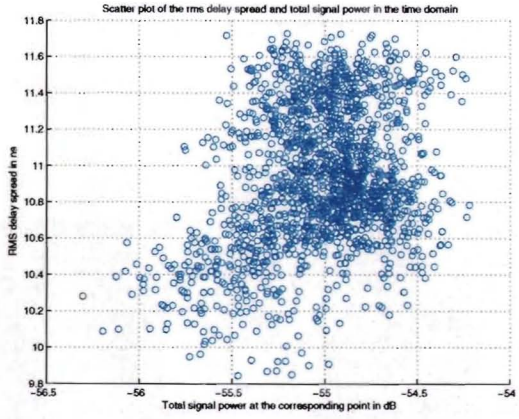

Figure E.15: Measurement M6: NLOS path, Tx: Omni directional, Rx: Horn.

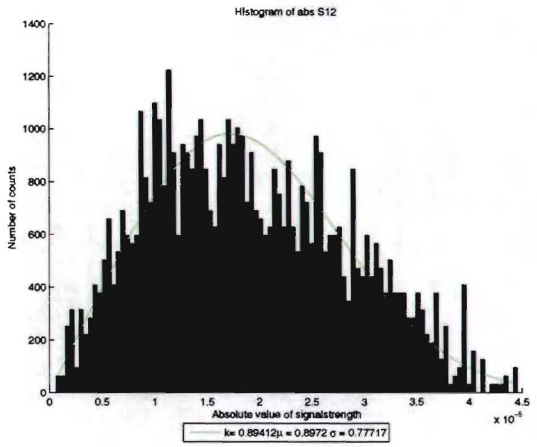

Figure E.16: Measurement M1: LOS path, Tx: Omni directional, Rx: Omni directional.

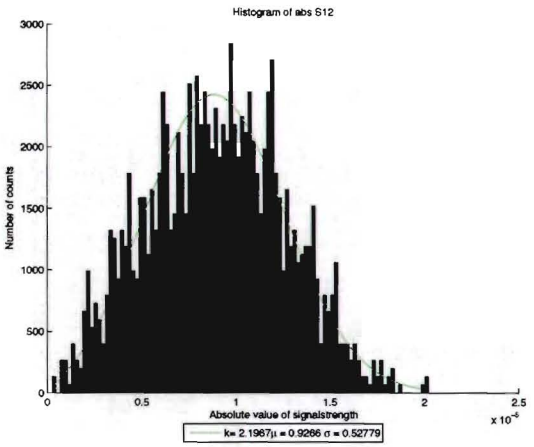

Figure E.17: Measurement M4: NLOS path, Tx: Omni directional, Rx: Omni directional.

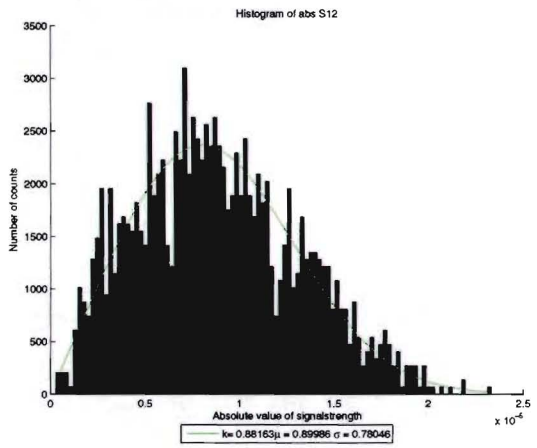

Figure E.18: Measurement M2: LOS path, Tx: Omni directional, Rx: Bow-Tie.

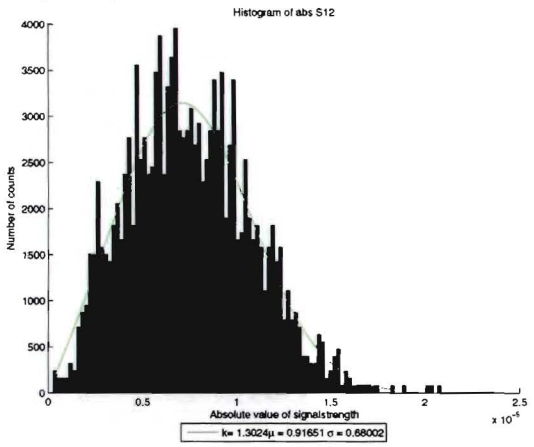

Figure E.19: Measurement M5: NLOS path, Tx: Omni directional, Rx: Bow-Tie.

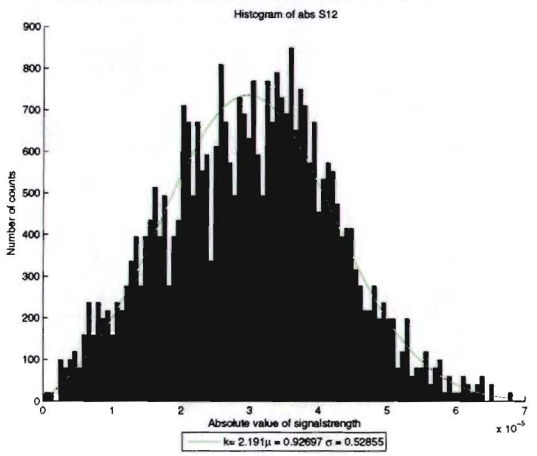

Figure E.20: Measurement M3: LOS path, Tx: Omni directional, Rx: Horn.

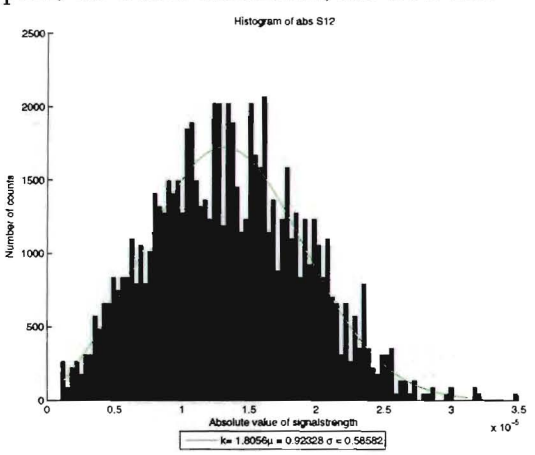

Figure E.21: Measurement M6: NLOS path, Tx: Omni directional, Rx: Horn.

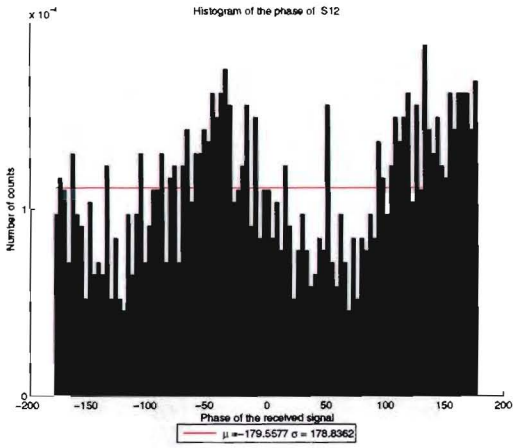

Figure E.22: Measurement M1: LOS path, Tx: Omni directional, Rx: Omni directional.

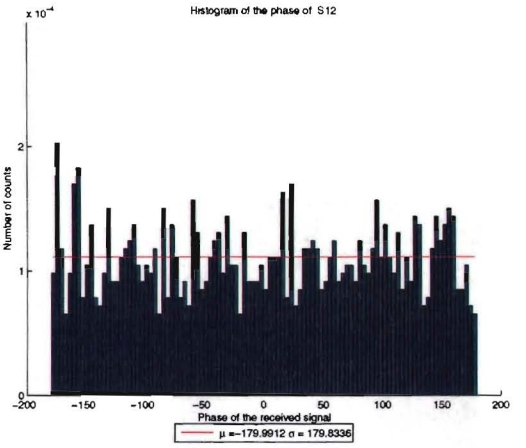

Figure E.23: Measurement M4: NLOS path, Tx: Omni directional, Rx: Omni directional.

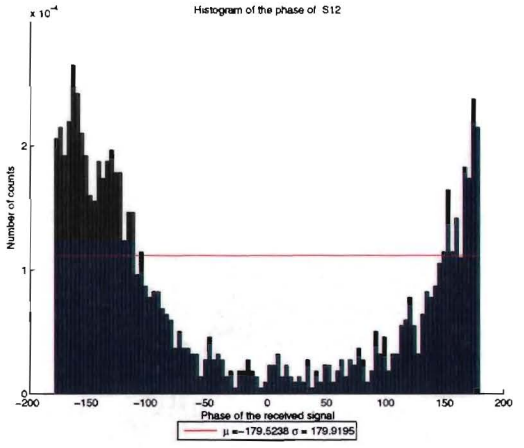

Figure E.24: Measurement M2: LOS path, Tx: Omni directional, Rx: Bow-Tie.

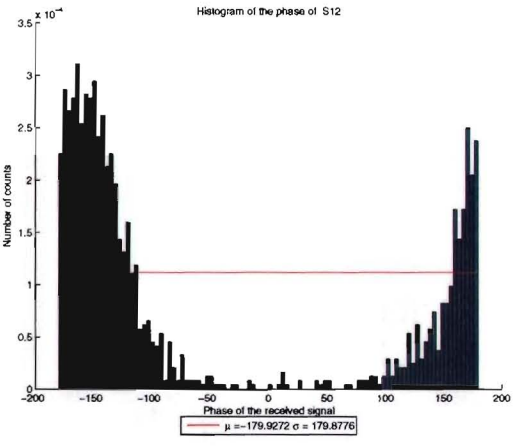

Figure E.25: Measurement M5: NLOS path, Tx: Omni directional, Rx: Bow-Tie.

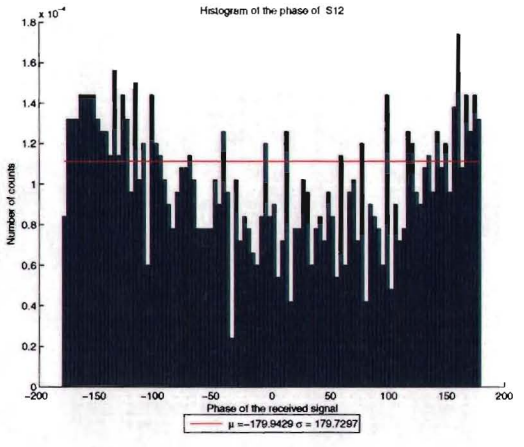

Figure E.26: Measurement M3: LOS path, Tx: Omni directional, Rx: Horn.

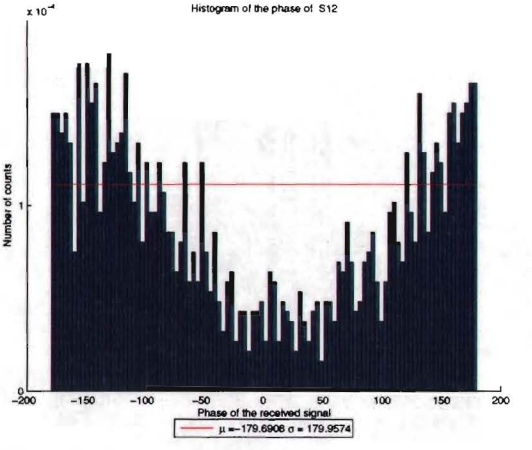

Figure E.27: Measurement M6: NLOS path, Tx: Omni directional, Rx: Horn.